Nanofluidics: a theoretical and numerical investigation of fluid transport in nanochannels

Simon Gravelle

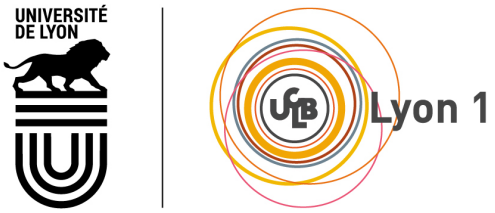

THESE DE DOCTORAT DE L'UNIVERSITE DE LYON

opérée au sein de

l'Université Claude Bernard Lyon 1

Ecole Doctorale N° 52
de Physique et d'Astrophysique (PHAST)

Soutenue publiquement le 17 Novembre 2015 par

Simon Gravelle

Nanofluidics: a theoretical and numerical investigation of fluid transport in nanochannels

---

Devant le jury composé de:

M. Thierry Biben	ILM Lyon	Président
M. Lydéric Bocquet	LPS-ENS Paris	Directeur de thèse
M. Laurent Joly	ILM Lyon	Invité
M. Jérome Mathé	LAMBE	Rapporteur
M. Roland Netz	FU Berlin	Examinateur
M. John Palmeri	LCC Montpellier	Examinateur
M. Benjamin Rotenberg	Lab. PHENIX	Rapporteur
M. Christophe Ybert	ILM Lyon	Directeur de thèse

Acknowledgements

Ce travail a été réalisé au sein du Laboratoire de Physique de la Matière Condensée et Nanostructures (LPMCN) devenu l'Institut Lumière Matière (ILM) de l'Université Claude Bernard Lyon 1. Je remercie Alfonso San Miguel et Marie-France Joubert de m'y avoir accueilli.

J'exprime mes sincères remerciements à l'ensemble des examinateurs, Thierry Biben, Jérôme Mathé, Roland Netz, John Palmery et Benjamin Rotenberg, en particulier à Thierry Biben pour avoir présidé le jury, ainsi qu'à Jérôme Mathé et Benjamin Rotenberg pour avoir accepté de rapporter ce travail.

Je voudrais remercier M. Klopfenstein, à l'époque professeur de mathématique au Lycée E. Belin de Vesoul, puisqu'il m'a poussé vers la physique en me transmettant son goût pour les sciences.

Ce fut un vrai plaisir de travailler sous la direction de Lydéric et Christophe et je leur suis reconnaissant pour tout ce qu'il m'ont apporté durant ces trois années. En particulier, je suis heureux de la confiance qu'ils m'ont accordé en me laissant travailler en toute liberté sur un large panel de sujets. Le binôme complémentaire qu'ils ont formé m'a permis de progresser efficacement. Je remercie Lydéric pour avoir financé ma thèse, et pour m'avoir invité plusieurs fois à Boston où j'ai pu découvrir le MIT. J'ai toujours été impressionné par son efficacité et sa vision globale de la science, le tout combiné à une nature humaine vraiment plaisante. En parallèle, j'ai eu la chance de pouvoir travailler avec Christophe dont la pertinence, la large culture scientifique et la personnalité joyeuse ont rendu nos échanges très fructueux et toujours agréables. Je suis heureux d'avoir pu apprendre autant à leurs cotés.

Ensuite, je suis très reconnaissant envers Laurent, mon encadrant officieux, sans qui le contenu de ce manuscrit aurait été considérablement plus pauvre. Sa gentillesse combinée à sa rigueur scientifique m'ont rendu la tache facile tout au long de ces trois années. Je lui suis également reconnaissant de m'avoir invité à Londres pour découvrir le monde des simulations ab initio.

Je voudrais remercier les chercheurs que j'ai côtoyé, et auprès desquels j'ai beaucoup appris. Choongyeop avec qui j'ai pris plaisir à maniper sur les nanocanaux, Rémy avec qui j'ai découvert la micro-fabrication en salle blanche, François dont j'ai partagé le bureau pendant un an et qui m'a transmis sa méthode de travail, et bien sûr tous les autres: Alessandro, Anne-Laure, Agnès, Bruno, Catherine B., Cécile, Charlotte, Christophe P., Gilles, Hélène, Jean, Jean-Paul, Kirsten, Loïc, Luc, Marie, Osvanny et Orianne. Ils participent largement à l'excellente ambiance de travail qui règne au sein de l'équipe liquide et interface.

Merci à Fabio et Ruben pour leur efficacité et leur sympathie. Merci à Delphine et Christelle pour leur efficacité, mais surtout pour leur flexibilité. Merci à Gilles pour la réalisation de pièces mécaniques.

Merci à tous les étudiants et post-doc pour toutes les discussions, les sorties et la vie en général: Ludivine, Nicolas W., Nicolas D., Xixi, Joseph, Baudoin, Isaac, Henry, Richard, Pauline, Loren, Angelique, Alexandra, Félix, Florence, Ronan, Renaud, Quentin, Sébastien, Rodney, Calina, Manon, Aude, Baptiste, Andrea, Julien L., Julien B., Nora, Antoine, Daniel, Mélodie, Pascal, Flore, Nahameh, Alessandro G., Tess, Teresa, Christophe, Ronan, Quentin, Florence, Alexis, Baptiste, Elisa, Catherine et Menka.

Merci à Osvanny de nous avoir accueilli chez lui, mais surtout pour sa grande générosité de façon générale. J'ai beaucoup appris de sa vision tranchée et objective du monde de la recherche.

Je suis en particulier très heureux d'avoir fait partie des ker-thésards, aux cotés de ker-Alexis, de ker-Catherine, de ker-Florence, de ker-Joseph et de ker-Menka, et ce malgré la ker-réticence de ker-Ronan. La ker-rédaction à ker-l-Ile d'Yeu, les ker-barbecues et les ker-balades aux ker-lacs resteront comme des points forts de cette thèse.

Catherine S., avec qui j'ai partagé plus que le sujet de cette thèse, occupe une place toute particulière dans ces remerciements. Les interactions que j'ai eues avec elle m'ont beaucoup apporté, et je reste imprégné pas son irréprochable honnêteté scientifique.

Je suis très heureux d'avoir partagé quelques temps mon bureau avec Élisa, qui est une vrai amie et quelqu'un pour qui j'ai énormément d'estime.

FIGURE 1: From left to right: meeting, wedding, driving.

Merci à ma famille ainsi qu'à ma nouvelle belle famille pour tout ce qu'ils m'ont apporté. Merci à Marija avec qui j'ai eu le plaisir de cohabiter ainsi que pour les nombreuses tasses made-in-Yougoslavie. Merci à Lola pour son soutien avant la thèse puis au début.

Et je termine ces remerciements par une personne d'exception dont la rencontre restera le point le fort de cette thèse. Je qui suis sincèrement heureux de poursuivre l'aventure avec Menka, qui a été successivement une amie, puis une compagne et maintenant ma femme. En tant que ma première interlocutrice scientifique, elle est toujours de bon conseil et de plus une remarquable relectrice.

Chapter 1

General introduction

Contents

You can find a shorter version of this introduction here: [1].

1.1 Generalities

1.1.1 What is nanofluidics?

Nanofluidics is the study of fluids confined in structures of nanometric dimensions (typically $1 - 100\,\text{nm}$) [2, 3]. Fluids confined in these structures

exhibit behaviours that are not observed in larger structures, due to a high surface to bulk ratio. Strictly speaking, nanofluidics is not a new research field and has been implicit in many disciplines [4–8], but has received a name of its own only recently. This evolution results from recent technological progress which made it possible to control what occurs at these scales. Moreover, advances have been made in observation/measurement techniques, allowing for measurement of the *small* physical quantities inherent to nano-sized systems.

Even though nanofluidics is born in the footstep of microfluidics, it would be incorrect to consider it an extension of microfluidics. Indeed, while in microfluidics the only scale which matters is the size of the system, nanofluidics has to deal with a large spectrum of characteristic lengths which induce coupled phenomena and give rise to complex fluid behaviours [9]. Moreover, since nanofluidics is at the intersection between physics, chemistry and biology, it concerns a wide range of domains such as physiology, membrane science, thermodynamics or colloidal science. Consequently, a multidisciplinary approach is often needed for nanofluidics' research.

Some striking phenomena taking place at the nanoscale have been highlighted during the past few years. For example, super-fast flow in carbon nanotubes [10–12], nonlinear eletrokinetic transport [13, 14] or slippage over smooth surfaces [15] have been measured. Those effects are indicators of the richness of nanofluidics. Accordingly, this field creates great hopes, and the discovery of a large variety of new interesting effects in the next decades is a reasonable expectation. Moreover, one can notice that most of the biological processes involving fluids operate at the nano-scale, which is certainly not by chance [9]. For example, the protein that regulates water flow in human body, called aquaporin, has got sub-nanometric dimensions [16, 17]. Aquaporins are known to combine high water permeability and good salt rejection, participating for example to the high efficiency of human kidney. Biological processes involving fluid and taking place at the nanoscale attest of the potential applications of nanofluidics, and constitute a source of inspiration for future technological developments.

Hereafter, an overview of the current state of nanofluidics is presented. First, a brief state-of-the-art, mainly focused on nano-fabrication and measurement

techniques is given. Then some current applications linked to nanofluidics are described.

1.1.2 State-of-the-art

Nanofluidics has emerged from the recent progresses of nanoscience and nanotechnology, such as progresses made in developing nano-fabrication technologies. Fabricating well-controlled channels is a major challenge for nanofluidics, and is a necessary condition for a systematic exploration of nanofluidic phenomena. This requires a good control of device dimensions and surface properties (charge, roughness, etc). For example, the improvement of lithography techniques (electron, x-beam, ion-beam, soft...) allows the fabrication of slit nanochannels [18]. Focus Ion Beam (FIB) allows to drill nanopores in solid membranes [19, 20]. There are also coatings and deposition/etching techniques that can be used to tune the surface properties [21, 22]. Siria et al. were able to manipulate a single boron nitride (BN) nanotube in order to insert it in a membrane separating electrolyte reservoirs and perform electric measurements [23]. Great developments of Scanning Tunneling Microscope (STM) or Atomic Force Microscopy (AFM) allow to characterize the fabricated devices.

In parallel, the efforts invested in nanofabrication have been combined to an improvement of measurement techniques. Most of them are based on the measurement of electric currents, and have been developed since the early days of physiology. But for a full understanding of nanofluidic properties, other quantities have to be made accessible. For example, local values of a velocity field can be obtained using nano-Particle Image Velocimetry (nano-PIV). Surface Force Apparatus (SFA) have been used to explore the hydrodynamic boundary condition and measure forces that play an important role in nanofluidics, such as van der Waals or electric forces.

In addition, a current challenge concerns water flow measurements. The main difficulty is due to the magnitude of typical flows through nanochannels: $\sim 10^{-18}\,\mathrm{m}^3/\mathrm{s}$ (it would take several years to grow a drop of 1 nl with such a flow). In order to detect a water flow through a nanochannel, some potential candidates have emerged during the last decade. One can cite, for example, Fluorescence Recovery After Photobleaching (FRAP), confocal

measurements or coulter counting measurements that have been reported to detect respectively $7 \cdot 10^{-18}\,\mathrm{m}^3/\mathrm{s}$ [24], $10^{-18}\,\mathrm{m}^3/\mathrm{s}$ [25] and $10^{-18}\,\mathrm{m}^3/\mathrm{s}$ [26]. However, the inconvenient of most of the existing measurement techniques is that they are indirect and require the use of dyes or probes.

Meanwhile, numerical progresses combined with calculation capacity improvement allow for the theoretical exploration of a large variety of nanofluidic properties. For example, the friction of water on solid surfaces can be investigated using ab initio methods [27], while molecular dynamics simulations are good candidates for fluid transport investigations [28, 29].

1.1.3 Applications

Some important applications of nanofluidics are listed hereafter.

Biology – First of all, most of the biological processes that involve fluids take place at the nanoscale [16, 30–32]. For example, the transport of water through biological membranes in cells is ensured by aquaporins, a protein with subnanometric dimensions. Aquaporins appear to have an extremely high water permeability, while ensuring an excellent salt rejection [1]. Another example of proteins with nanometric dimensions are ion pumps and ion channels, that ensure the flow of ions across cell membranes [33, 34]. Combined, those proteins allow the (human) kidney, which is an example of natural desalination and separation tool, to purify water with an energy cost far below current artificial desalination plants [9].

Desalination – At the same time, some of the most used (man-made) desalination techniques, consisting in the separation of salt and water in order to produce fresh water, are using nanofluidic properties [35, 36]. This is the case of membrane-based techniques, such as Reverse Osmosis (RO) [37], Forward Osmosis (FO) [38] or ElectroDialysis (ED) [39]. The improvement of the membrane technology has made it possible to desalinate with an energy consumption close to the minimum energy set by thermodynamics.

Extraction of mixing energy – Another interesting application of nanofluidics concerns the extraction of the energy of mixing from natural water

[1] Note that the shape of aquaporins is the basis of the chapter 2.

resources. This so-called blue energy is the energy available from the difference in salt concentration between, for example, seawater and river water. Pressure-Retarded Osmosis (PRO) converts the huge pressure difference originating in the difference in salt concentration ($\sim$ bars) between reservoirs separated by a semipermeable membrane into a mechanical force by the use of a semipermeable membrane with nanosized pores [40]. Siria et al. proposed another way to convert blue energy based on the generation of an osmotic electric current using a membrane pierced with charged nanotubes [23].

Nanofluidic circuitry – The recent emergence of nanofluidic components benefiting of the surface effects of nanofluidics leads naturally to an analogy with micro-electronics. Indeed, some nanofluidic components imitate the behaviour of over-used micro-electronic components such as the diode or the transistor [13] [2]. Even if a complete analogy between both fields fails due to the physical differences between ions and electrons, controlling/manipulating nano-flows the same way we control electric currents would allow for regulating, sensing, concentrating and separating ions and molecules in electrolyte solutions [41] with many potential applications in medicine, such as drug delivery or lab-on-a-chip analyses.

An overview of the full complexity of nanofluidics is highlighted in the following by the description of some theoretical bases. The first part provides the definitions of the characteristic lengths that separate the different transport regimes and lead to a large variety of behaviours. The second part describes the numerous forces that play a role in nanofluidics and that are at the origin of the various phenomena. Finally, the third part focuses on transport response of a membrane pierced with a slit nanochannel and submitted to external forcing.

[2] Note that nanofluidic diodes are discussed in chapter 4.

1.2 Definitions

1.2.1 Characteristic lengths

The richness of nanofluidics comes from the existence of a large number of characteristic lengths related to the finite size of the fluid's molecules, to electrostatics or to the fluid dynamics. Indeed, when one or more dimensions of a nanofluidic system compares with those characteristic lengths, new phenomena may appear. An overview of length scales at play in nanofluidics can be seen in figure 1.1. In what follows, a description of each length is given.

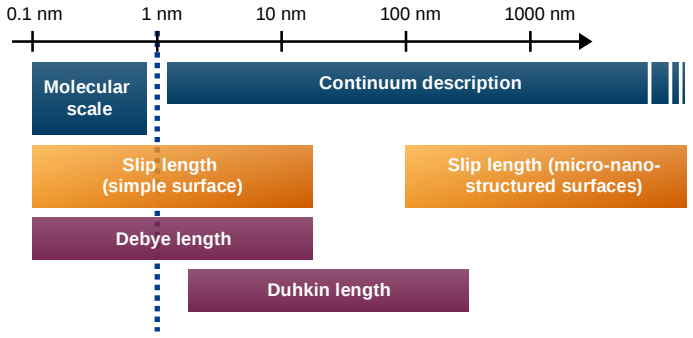

FIGURE 1.1: Overview of length scales at play in nanofluidics, freely inspired from reference [2].

The molecular length scale is associated with the finite size of the fluid's molecules and its components (molecules, ions...). More precisely, it is linked to their diameter σ, typically in the angstroms scale ($1\,\text{Å} = 1 \times 10^{-10}\,\text{m}$). For example, $\sigma \sim 3\,\text{Å}$ for the water molecule, $\sigma \sim 4 - 5$ Å for common ionic species (Na, K, Cl) [42]. This length defines *a priori* the ultimate limit of the study of nanofluidic transport [2]. In the vicinity of a confining wall, fluids can experience some structuring and ordering at the molecular length scale. An example of water molecules near a solid surface is shown in figure 1.2. This effect is exacerbated in confining pores, when there is only room for a limited number of molecules. In that case, strong deviations from continuum predictions can be expected. Another important effect related to the size of molecules, and thus to the molecular length is osmosis; which is the phenomenon by which a solvent moves across a semipermeable membrane (permeable to the solvent, but not to the solute) separating

two solutions of different concentrations. Note that the question of the robustness of hydrodynamics for confinement below one nanometer and the phenomenon of osmosis will both be discussed in this thesis.

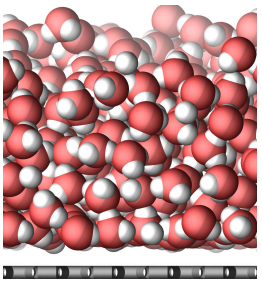

FIGURE 1.2: Water molecules (oxygen in red, hydrogen in white) next to a graphene sheet (in gray).

The Bjerrum length is defined considering two charged species in a solution. It corresponds to the distance at which the thermal energy $k_B T$, with k_B the Boltzmann constant and T the absolute temperature, is equal to the energy of electrostatic interaction. The Bjerrum length ℓ_B can be written as

$$\ell_B = \frac{Z^2 e^2}{4\pi\epsilon k_B T}, \tag{1.1}$$

with e the elementary charge, Z the valency, ϵ the dielectric permittivity of the medium. For two monovalent species in water at ambient temperature, ℓ_B is approximately equal to 0.7 nm. Depending on the considered solution (monovalent ionic species, organic solvent with low dielectric constant, etc.), ℓ_B can be either large enough to be clearly dissociated from the molecular length, or be of the same order as the molecular length. The physics has to be differentiated in each case. There are physical effects with important implications on nanofluidic transport that are linked to the Bjerrum length. For example, for confinements below ℓ_B, one expects a large free-energy cost to undress an ion from its hydration layer and make it enter the pore, with consequences on filtering processes of charged species.

The Gouy-Chapman length is constructed in the spirit of the Bjerrum length. It is defined as the distance from a charged wall where the electrostatic interaction of a single ion with the wall becomes of the order of the thermal energy. For a surface charge Σ, it writes

$$\ell_{GC} = \frac{e}{2\pi\Sigma\ell_B}. \tag{1.2}$$

For monovalent species in water and a typical surface charge $\Sigma \sim 50$ mC/m^2, ℓ_{GC} is approximately equal to 0.7 nm.

The Debye length is the characteristic length of the layer that builds up near a charged surface in an ionic solution. This layer counter balances the influence of the electric charge, and is of main importance in the study of transport at the nanoscale, as will be discussed later. The Debye length can be written as

$$\lambda_D = \frac{1}{\sqrt{8\pi l_B c_0}}, \tag{1.3}$$

with c_0 the concentration in ionic species. Indeed, when a solid surface is immersed in an aqueous solution, it usually acquires a surface charge Σ due to chemical reactions (dissociation of surface groups and specific adsorption of ions in solution to the surface [43, 44]). In response to this surface charge, the ionic species in the liquid rearrange themselves and form a layer that screens the influence of the surface charge. This layer of ionic species is called the Electrical Double Layer (EDL). Note that the Debye length is independent of the surface charge Σ, and inversely proportional to the square root of the salt concentration c_0. Typically λ_D is equal to 30 nm for $c_0 = 10^{-4}$ M, 3 nm for $c_0 = 10^{-2}$ M and 0.3 nm for $c_0 = 1$ M.

The Dukhin length is based on the comparison between the bulk to the surface electric conductance, which links the electric current to an applied electric field. It characterizes the channel scale below which surface conductance dominates over bulk conductance [2]. In a channel of width h and surface charge density Σ, the excess in counterion concentration is $c_e = 2\Sigma/he$ with e the elementary charge and where the factor 2 accounts for the two surfaces. One may define a Dukhin number $\mathrm{Du} = |\Sigma|/hc_0e$. A Dukhin length ℓ_{Du} can then be defined as

$$\ell_{\mathrm{Du}} = \frac{|\Sigma|}{c_0 e}. \tag{1.4}$$

For a surface with a surface charge density $\Sigma = 50$ mC/m^2, ℓ_{Du} is typically 0.5 nm for $c_0 = 1$ M, while $\ell_{\mathrm{Du}} = 5$ µm for $c_0 = 10^{-4}$ M.

The slip length is defined as the depth inside the solid where the linear extrapolation of the velocity profile vanishes. Unlike previous lengths, that are all related to electrostatics, the slip length comes from the dynamic of

the fluid near a solid surface. It characterizes the hydrodynamic boundary condition of fluids at interfaces. Its expression can be derived as follows: first, assume that the tangential force per unit area exerted by the liquid on the solid surface is proportional to the fluid velocity at the wall v_w: $\sigma_{xz} = \lambda v_w$, with λ the friction coefficient, z the normal to the surface, x the direction of the flow. Then, combining this equation with the constitutive equation for a bulk Newtonian fluid, $\sigma_{xz} = \eta \partial_z v_x$, one obtains the Navier boundary condition [15]:

$$v_w = \frac{\eta}{\lambda} \partial_z v_x \Big|_w = b \partial_z v_x \Big|_w , \tag{1.5}$$

where the slip length $b = \eta/\lambda$ is defined as the ratio between the *bulk* liquid viscosity and the *interfacial* friction coefficient. Accordingly, several kinds of hydrodynamic boundary conditions can apply:

- the no-slip boundary condition supposes that the fluid has zero velocity relative to the boundary, $v_w = 0$ at the wall, and corresponds to a vanishing slip length $b = 0$;
- the perfect-slip boundary condition corresponds to the limit of an infinite slip length ($b \to \infty$), or equivalently a vanishing friction coefficient ($\lambda \to 0$). It corresponds to a shear free boundary condition. Traditionally, the perfect-slip boundary condition is used when the slip length b is much larger than the characteristic length(s) of the system;
- the partial-slip boundary condition concerns intermediate slip length.

For simple liquids on smooth surfaces, slip lengths up to a few tens of nanometers have been experimentally measured [15].

1.2.2 Mathematical description of the EDL

The Electrical Double Layer (EDL) plays a fundamental role in nanofluidics due to a large surface area to volume ratio. It corresponds to the layer of ionic species that counter-balances the influence of a surface charge. Numerous phenomena, that will be discussed later, take their origin within

the EDL, so a mathematical description of this layer is of main importance here. The conventional description is given hereafter.

The Gouy-Chapman theory is at the basis of EDL's description. It is based on the following hypothesis [45]:

- ions are considered as (punctual) spots,
- the dielectric permittivity of the medium is supposed constant in the medium,
- the charge density and the electrical potential are seen as continuum variables,
- the correlations between ions as well as the ion-solvent interactions are not taken into account (mean field theory),
- only electrostatic interactions are considered.

Poisson-Boltzmann equation – Under the previous hypotheses, let us write the equation that underlies the distribution of ions near a flat surface. Consider monovalent ions near a flat surface S, located at $z = 0$, with homogeneous surface charge density Σ and surface potential V_s, as shown in figure 1.3. The link between the electrical potential $V(z)$ and the charge

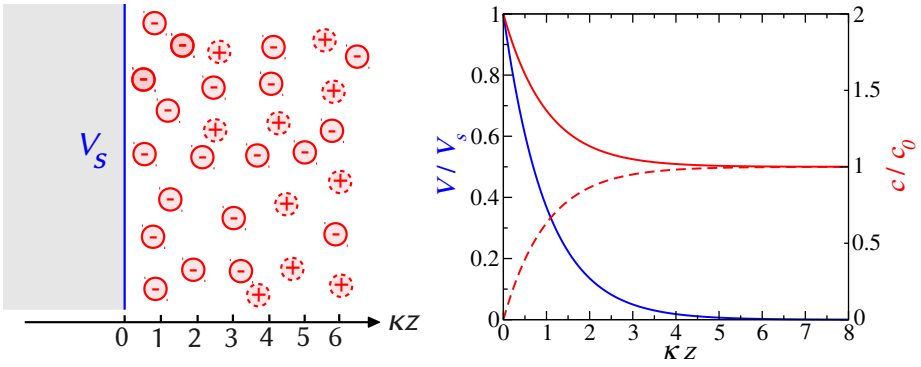

FIGURE 1.3: Left: scheme of the studied configuration. Right: Debye-Hückel solution (1.11) for the electrical potential V in blue and linearized Boltzmann equation (1.12) for the concentration profile $c_\pm$ in red.

density $\rho_e(z)$ at a z distance of the surface inside the ionic solution is given by a Poisson equation:

$$\Delta V = \frac{\mathrm{d}^2 V}{\mathrm{d}z^2} = -\frac{\rho_e}{\epsilon}, \tag{1.6}$$

where $\epsilon = \epsilon_0 \epsilon_r$ is the solvent permittivity (for water at ambient temperature, $\epsilon_r \approx 80$). The idea is to ignore the thermal fluctuations of V and ρ_e and to consider their respective averaged values only. At the thermal equilibrium, the densities of positive $c_+(z)$ and negative $c_-(z)$ ions are governed by the Boltzmann equation:

$$c_\pm(z) = c_0 e^{\mp \beta e V(z)}, \tag{1.7}$$

with $\beta = 1/k_B T$ and c_0 the concentration in ion of charge $\pm$ e far from the wall. The charge density reads $\rho_e = e(c_+ - c_-) = -2ec_0 \sinh(\beta eV)$. Coupling this equation with (1.6), we get the Poisson-Boltzmann equation for the electrical potential $V(z)$:

$$\frac{\mathrm{d}^2 V}{\mathrm{d}z^2} = \frac{2ec_0}{\epsilon} \sinh(\beta eV). \tag{1.8}$$

Introducing the previously described Bjerrum length ℓ_B, defined as the length at which the thermal energy balances the electrostatic one, we can rewrite the equation 1.8:

$$\beta e \frac{\mathrm{d}^2 V}{\mathrm{d}z^2} = 8\pi \ell_B c_0 \sinh(\beta eV) = \kappa^2 \sinh(\beta eV), \tag{1.9}$$

where $\kappa = (8\pi \ell_B c_0)^{1/2}$ corresponds to the inverse of the previously described Debye length λ_D. This equation describes the evolution of the electrical potential next to a charged surface.

Linearized Poisson-Boltzmann equation – In the general case, the Poisson-Boltzmann equation can not be solved analytically. For small potentials ($eV \ll k_B T$), an approximate form of the Poisson-Boltzmann, the Debye-Hückel equation, can be written as:

$$\frac{\mathrm{d}^2 V}{\mathrm{d}z^2} = \kappa^2 V. \tag{1.10}$$

Assuming that the electrical potential vanishes far from the surface, the solution of the Debye-Hückel equation reads

$$V(z) = V_s e^{-\kappa z}, \tag{1.11}$$

where V_s is the surface electrical potential. Equation (1.11) is plotted in figure 1.3. The electrical potential is screened over a distance $\kappa^{-1} = \lambda_D$,

the Debye length, which then gives the width of the EDL. The linearization of the equation (1.7) gives

$$c_\pm = \rho_s \exp(\mp\beta e V(z)) \approx c_0(1 \mp \beta e V(z)) = c_0(1 \mp \beta e V_s \exp(-\kappa z)). \quad (1.12)$$

Equation (1.12) is plotted in figure 1.3 for both $\pm$ species.

Non-linear Poisson-Boltzmann equation – In some situations, a solution for the non-linear Poisson-Boltzmann equation exists. Let us consider here the case of a single flat wall, the electrolyte is located in $z > 0$ and the solid wall in $z < 0$. A surface charge density $\Sigma < 0$ is located at $z = 0$. The electric field is taken to be equal to 0 inside the wall as well as far from the wall inside the electrolyte. At the wall, the electrostatic boundary condition links the electric field and the surface charge:

$$\left.\frac{\partial V}{\partial z}\right|_{z=0} = -\frac{4\pi}{\epsilon}\Sigma. \quad (1.13)$$

Solving the PB equation (1.8) with this boundary condition (1.13) leads to [46]

$$V(z) = -\frac{2}{e\beta}\ln\left(\frac{1+\gamma e^{-z/\lambda_D}}{1-\gamma e^{-z/\lambda_D}}\right), \quad (1.14)$$

where γ is the positive root γ_0 of the equation:

$$\gamma^2 + \frac{2\ell_{GC}}{\lambda_D}\gamma - 1 = 0. \quad (1.15)$$

For a positive surface charge Σ, the solution for V is identical, though with $\gamma = -\gamma_0 (< 0)$. The surface potential V_s can be written as $V_s = 4\arctan(-z/\lambda_D)/\beta e$.

In this thesis, the Poisson-Boltzmann solutions (linear and non-linear) will be frequently used.

1.2.3 Nanoscale forces

Now that the general ideas of the Gouy-Chapman description of the EDL have been given, let us describe some of the most important forces that play a role in nanofluidics. These forces are at the origin of the large range of phenomena observed in nanofluidics, and they give rise to both equilibrium

or kinetic phenomena [3]. Note that the distinction we will make between forces is artificial since they all are electrical in nature [47], but it still makes sense because of the many different ways in which the electrical force presents itself.

As a side note, each system depends fundamentally on individual forces that are applied between individual atoms. However, in practice, large systems ($\sim 10\,\mathrm{nm}$) can usually be described with continuum theory, which statistically averages the single interactions. This is why we may speak of forces exerted by walls on particles or molecules, or between walls, or between particle or molecules.

Electrostatic forces are long range interactions acting between charged atoms or ions [47]. Two particles of respective charges Q_1 and Q_2 at a distance r act on each other as follows:

$$F(r) = \frac{Q_1 Q_2}{4\pi\epsilon_0\epsilon_r r^2}, \tag{1.16}$$

where ϵ_r is the dielectric permittivity of the medium. $F(r)$ is directed along the axis defined by the position of the two particles. Equation (1.16) is known as the Coulomb law. Electrostatic forces can be either attractive or repulsive, depending on the sign of the product $Q_1 Q_2$. They are, for example, at the origin of the building of the Electrical Double Layer (EDL).

Van der Waals forces are residual forces of electrostatic origin which are always present, even between neutral atoms. They are relatively weak in comparison to chemical bonding for example (see below), but they nevertheless play a role in a large range of phenomena such as adhesion, surface tension or wetting. Van der Waals forces even manifest themselves at macroscopic scales since they are at the origin of the adhesion of gecko, a decimetric reptilia, on solid surfaces. Van der Waals forces include attractions and repulsions between atoms, molecules and surfaces. They have three possible origins such as:

- the force between two permanent dipoles,
- the force between a permanent dipole and an induced dipole,
- the force between two induced dipoles (London dispersion force).

Van der Waals forces are long-range, can bring molecules together or mutually align/orient them, and are not additive. They have to be described with the quantum mechanical formalism, which is beyond the scope of the present work.

The DLVO (Derjaguin, Verwey, Landau, Overbeek) theory gives a large picture of nanoscale forces which includes van der Waals forces and coulombic forces. However, some effects that appear at very short range can not be described in the framework of the DLVO theory. Non-DLVO forces are discussed in what follows.

Chemical or bonding forces link two or more atoms together to form a molecule [47]. Bonds are characterized by the redistribution of electrons between the two or more atoms. The number of covalent bonds that an atom can form with other atoms depends on its position in the periodic table. This number is called the valency. For example, it is equal to one for hydrogen and two for oxygen, which leads to water molecule H_2O (H-O-H). Notice that covalent bonds are of short range ($0.1 - 0.2\,\mathrm{nm}$) and directed at well-defined angles relative to each other. For example, they determine the way carbon atoms arrange themselves to form diamond structure. Notice that covalent bonding comes from complex quantum interactions which are beyond the scope of the present work.

Repulsive steric forces appear when atoms are brought too close together. It is associated with the cost in energy due to overlapping electron clouds (Pauli/Born repulsion). A consequence is the size exclusion, widely used in membranes from angström to micrometer [3]. It plays a role for example in aquaporins (water channels), that offer a low resistance for water molecules, but do not allow ions to pass through. To pass through this channel, the ion needs to lose its water shell, which is energetically unfavorable. Notice that, combining electrostatic forces and steric forces, it is possible to develop K^+ channels with a high selectivity for K^+ over Na^+ while both have water shells [48].

Solvation forces (or structural forces) are related to the mutual force exerted by one plate on another when they are separated by a structured

liquid [3]. Next to a solid surface, density oscillations are expected. If two solid surfaces immersed in a fluid are separated by a short distance, liquid molecules must accommodate the geometric constraint, leading to solvation forces between the two surfaces, even in the absence of attractive walls. Depending on both surface properties (well ordered, rough, fluid-like) and fluid properties (asymmetrically shaped molecules, with anisotropic or non pair-wise additive interaction potential), the resulting solvation forces can be either monotonic or non-monotonic, repulsive or attractive. See reference [47] for more details. Notice that, in the case of water molecules, solvation forces are called hydration forces.

Hydrophobic forces come from interactions between water and low water-soluble objects (molecules, clusters of molecules...). These substances usually have long carbon chains that do not interact with water molecules, resulting in a segregation and an apparent repulsion between water and nonpolar substances. The hydrophobic effect, which results from the presence of hydrophobic forces, is actually an entropic effect: each water molecule can form four hydrogen bonds in pure water, but can not form as much if surrounded by hydrophobic (apolar) species. Hence, apolar molecules (or clusters of molecules) will rearrange themselves in order to minimize the contact surface with water. An example is the mixing of fat and water, where fat molecules tend to agglomerate and minimize the contact with water.

Non-conservative forces, such as friction or viscous forces, are referred as non-conservative forces because they involve energy transfer from one body to another. Contrary to other forces, which act on a body and generate a motion according to the second law of Newton, non-conservation forces have no force law and arise as a reaction to motion. Inside a liquid, friction is linked to a fluid property: the viscosity, which is a property of a fluid to resist to a shear. It comes from collisions between neighbouring particles that are moving at different velocities. For example, when a fluid flows through a pipe, the particles generally move quickly near the pipe's axis and slowly near its walls, leading to stress. The friction between water molecules

[3] Liquid structuring has been mentioned in the subsection 1.2.1, and will be central in chapter 3

leads to a dissipation that has to be overcome, for example by a pressure difference between the two ends of the pipe, to keep the fluid moving.

Other forces, such as gravitational or inertial forces, are of lesser importance in nanofluidics and are not discussed here.

1.2.4 Some consequences

The previously described forces give rise to a large variety of phenomena. As an illustration, some of them are presented here.

Cohesion is related to attractive forces between molecules of the same substance. It is due to intermolecular attractive forces. They can be van der Waals forces or hydrogen bonding. Cohesion is at the origin, for example, of the tendency of liquids to resist separation.

Adhesion corresponds to attractive forces between unlike molecules. They are caused by forces acting between two substances, which can have various origins, such as electrostatic forces (attraction due to opposite charges), bonding forces (sharing of electron), dispersive (van der Waals forces) etc. For example, water tends to spread on a clean glass, forming a thin and uniform film over the surface. This is because the adhesive forces between water and glass are strong enough to pull the water molecules out of their spherical formation and hold them against the surface of the glass.

Surface tension is related to the elastic tendency of liquids which makes them acquire the least surface area possible. This results from the fact that when exposed to the surface, a molecule is in an energetically unfavorable state. Indeed, the molecules at the surface of the liquid lack about half of their cohesive forces, compared to the inner molecules of the bulk liquid [49]. Hence a molecule at the surface has lost about half its cohesion energy. Surface tension is a measure of this lost of energy per surface unit. In the thermodynamic point of view, it is defined as the excess of free energy due to the presence of an interface between two bulk phases [50]. The surface tension γ is of the order of magnitude of the bond energy ϵ between molecules of the fluid divided by the cross section area of a molecule σ^2:

$$\gamma \sim \frac{\epsilon}{\sigma^2}.$$

Finally one may notice that surface tension is also present at liquid-liquid, liquid-solid and solid-air interfaces.

Wetting is the study of the spreading of a liquid deposited on a solid (or liquid) substrate. When a small amount of liquid is put in contact with a flat solid surface, there are two different equilibrium situations: partial wetting, when the liquid shows a finite contact angle θ, and total wetting, in which the liquid spreads completely over the surface and where θ is not defined. The property of the fluid to spread on the surface is characterized by the spreading parameter S which measures the difference between the energy per unit area of the dry surface of the solid substrate and the wetted surface:

$$S = \gamma_{SV} - (\gamma_{SL} + \gamma_{LV}) \tag{1.17}$$

where γ_{SV}, γ_{SL} and γ_{LV} denote the free energies per unit area of respectively the solid-vapour interface, the solid-liquid interface and the liquid-vapour interface equal to the surface tension γ. In the case of a positive S, the surface energy of the dry surface is larger than the energy of the wetted surface, so the liquid tends to extend completely to decrease the total surface energy, hence θ is equal to zero. A negative S corresponds to a partial wetting situation, where the liquid does not completely spread on the surface and forms a spherical cap, adopting an angle $\theta > 0$. From the equilibrium of the capillary forces at the contact line or from the work cost for moving the contact line, one gets the Young-Dupré relation:

$$\cos\theta = \frac{\gamma_{SV} - \gamma_{SL}}{\gamma}. \tag{1.18}$$

Capillary forces originate in the adhesion between the liquid and the solid surface molecules. It is strongly linked to the existence of a surface tension, as well as to the concept of wetting and contact angle. In certain situations, those forces pull the liquid in order to force it to spread the solid surface. Depending on the configuration, it can make the liquid fill a solid channel for example. Capillary force will be discussed in greater details in chapter 3.

1.2.5 Transport in nanochannels

In this section, we consider various transport phenomena that can occur in a nanochannel separating two reservoirs containing an electrolyte. The purpose is to give a simple expression of each flux as a function of various driving forces (mechanical pressure, solute concentration and electrical potential gradients). For the sake of simplicity, the nanochannel is chosen to be a slit ($\sim$ 2D) and entrance effects are not taken into account [4]. The walls are perpendicular to z, respectively located in $z = \pm h/2$ and driving forces are applied along x, see figure 1.4. The channel has a length L along x and a width w along y. The Reynolds number $Re = \rho v L/\mu$ (where ρ and μ are respectively the fluid density and the dynamic viscosity and v and L are respectively the characteristic velocity and length of the flow) is assumed to be lower than one and the problem to be stationary. Hence, the governing equation for the flow is the Stokes equation:

$$\eta \triangle \vec{u} = \vec{\nabla} p + \vec{F} \tag{1.19}$$

where η is the fluid viscosity, $\vec{u}$ is the velocity field, p is the hydrodynamic pressure and $\vec{F}$ a volume force. The surface charge density is Σ, and will be different from 0 if specified only. Unless otherwise stated, the height of the channel h will be considered large in comparison to the typical range of the potential (i.e. the Debye length). Unless otherwise stated, the no-slip boundary condition will be used for the solvent along walls. The system is shown on figure 1.4.

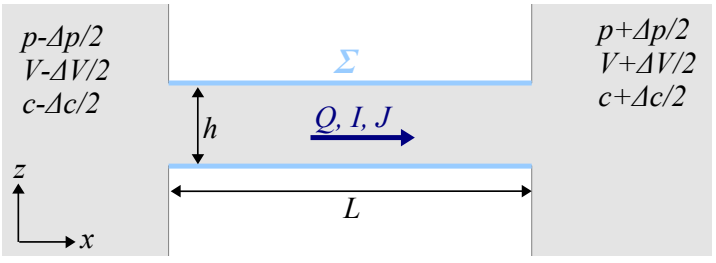

FIGURE 1.4: Sheme of the 2D channel used for the calculations.

A flow through the membrane can occur as a consequence of a force near the membrane [51]. Here we consider this force to be a mechanic pressure drop

[4] Notice that hydrodynamic entrance effects are discussed in this thesis, see chapter 2.

Δp, difference in solute concentration Δc or difference in electrical potential ΔV. We suppose that the considered forcing are weak, so equilibrium profiles remain unmodified along z, and flows are linear functions of the forces operating. Hereafter we will study the volume flow Q, the ionic flow J_i and the electrical current I_e resulting from Δp, Δc and ΔV. The phenomenological equations linking the three flows to the three forces write:

$$\begin{aligned} Q &= L_{11}\Delta P + L_{12}\Delta c + L_{13}\Delta V, \\ J_i &= L_{21}\Delta P + L_{22}\Delta c + L_{23}\Delta V, \\ I_e &= L_{31}\Delta P + L_{32}\Delta c + L_{33}\Delta V, \end{aligned} \tag{1.20}$$

where L_{IJ} are coefficients. According to Onsager's law, the matrix of coefficients L_{IJ} is symmetrical, i.e. $L_{IJ} = L_{JI}$. Finally, one assumes that in the middle of the channel (z=0), concentration, electrical potential and pressure evolve linearly with x.

Direct terms

The direct terms of the matrix of transport (1.20) correspond to the diagonal terms L_{II}. They link each flux with their natural force, respectively the solvent flow with the pressure gradient, the ionic flow with the salt gradient and the ionic current with the electrical gradient. Each of them is calculated hereafter in the previously described configuration (slit nanochannel).

$\mathbf{L_{11}$ – the hydrodynamic permeability} characterizes the flow transport across a given structure under a pressure gradient. Using both symmetry and impermeability of the walls, one gets for the velocity field: $\vec{u} = u_x(z)\vec{u}_x$. So the Stokes equation 1.19 can be written as $\eta\partial_z^2 u_x = \partial_x p$. A first integration of the Stokes equation between 0 and z gives $\eta\partial_z u_x = z\partial_x p$, where we used that $\partial_z u_x|_{z=0} = 0$ by symmetry, and that $\partial_x p$ does not depends on z. Another integration between $-h/2$ and z using that $\partial_x p = \Delta p/L$ gives

$$u(z) = u_w + \frac{1}{\eta}\left(\frac{z^2}{2} - \frac{h^2}{8}\right)\frac{\Delta p}{L}, \tag{1.21}$$

where u_w is the wall velocity, which depends on the hydrodynamic boundary condition (see the definition of the slip length, subsection 1.2.1). Finally,

L_{11} in case of the no-slip boundary condition ($u_w = 0$) can be written as:

$$\boxed{L_{11} = \frac{Q}{\Delta p} = -\frac{1}{12\eta} \times \frac{wh^3}{L}.} \tag{1.22}$$

Hence the hydrodynamic permeability of a membrane in the low Reynolds number regime is limited by the viscosity of the fluid, and depends strongly on the dimensions of the channel.

$\mathbf{L_{22}$ – the ionic permeability} characterizes the ionic flow through a membrane under a salt concentration gradient. From the Fick's law of diffusion:

$$\vec{j}_{\pm} = -D_{\pm}\vec{\nabla}c_{\pm}, \tag{1.23}$$

where $D_{\pm}$ are diffusion coefficients of the $\pm$ species respectively, one can write the total flow J_i assuming that $D^+ = D^- = D$:

$$J_i = \int_S (\vec{j}_+ + \vec{j}_-).\mathrm{d}\vec{S} = -wD \int_{-h/2}^{h/2} \partial_x(c_+(x) + c_-(x))\mathrm{d}z. \tag{1.24}$$

In a neutral channel, and assuming that $c_{\pm}(x) = x\Delta c/L + c_0$, it gives

$$\boxed{L_{22} = \frac{J_i}{\Delta c} = -D \times \frac{S}{L},} \tag{1.25}$$

where $S = hw$ is the surface of the channel. Notice that equation (1.25) describes ionic flow through a membrane under salt gradient in absence of surface charge. In case of the presence of a surface charge density Σ, the nanochannel exhibits a selective permeability for ion diffusive transport [2]. Consequently, the concentration of counterions inside the channel is higher that the bulk concentration, while the concentration in co-ions is lower. Therefore, ions of the same charge as the nanochannel exhibit a lower permeability, while ions of the opposite charge have a higher permeability through the nanochannel. Following Plesis et al., an effective nanochannel section can be defined for each species $S^{\pm}_{\mathrm{eff}} = \beta^{\pm}S$ where β is an exclusion/enrichment coefficient [52]:

$$\beta_{\pm} = \frac{1}{h}\int_{-h/2}^{h/2} e^{\mp\phi(z)}dz; \tag{1.26}$$

where $\phi(z) = \beta eV(z)$ with $V(z)$ the electrical potential. One can use the

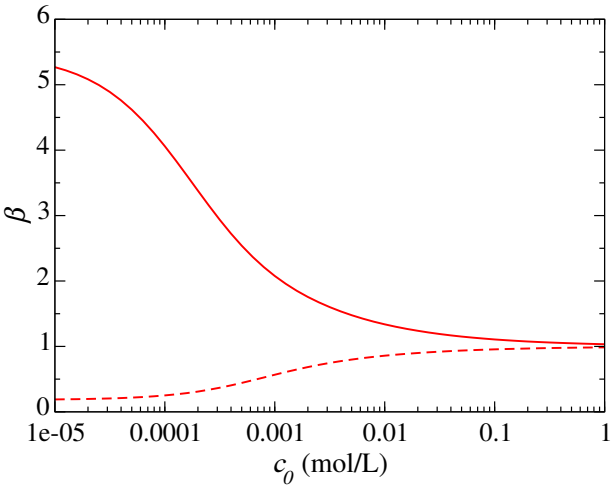

FIGURE 1.5: Equation (1.26) for β_+ (continuous) and β_- (dashed) as a function of the bulk concentration for a negatively charged surface.

linearised Poisson-Boltzmann equation to calculate the ion concentration profile in the slit. An example is shown in figure 1.5.

L_{33} – the ionic conductance characterizes the ionic current through a membrane under an applied electrical potential difference: $G = I_e/\Delta V$. First, let us define the (bulk) conductivity of the solution κ_b:

$$\kappa_b = e(\mu_+ c_+ + \mu_- c_-) \tag{1.27}$$

with $\mu_\pm$ and $c_\pm$ respectively the mobility and the volume density of $\pm$ ions [43]. At high ionic strength, or for a neutral channel ($\Sigma = 0$), equation (1.27) can be used directly to calculate the conductance of the channel $G_{\text{bulk}} = \kappa_b wh/L$. However, for a non-neutral channel ($\Sigma \neq 0$), if one looks at the ionic conductance versus the salt concentration on a log-log scale, a conductance plateau is observed at low ionic strength. This is due to the contribution to the total current of ions of the EDL. This excess counterions concentration can be written as [53]:

$$c_{\text{e}} = \frac{2\Sigma}{he} \tag{1.28}$$

where the 2 accounts for the two surfaces. From this excess counterions concentration, one can define a surface conductance $G_{\text{surf}} = e\mu c_{\text{e}} wh/L$. Then the total conductance is the sum of a bulk conductance and a surface conductance:

$$G = G_{\text{bulk}} + G_{\text{surf}} = \mu c_s e \frac{wh}{L} + 2\Sigma\mu\frac{w}{L} \tag{1.29}$$

where we assumed that $\mu_+ = \mu_-$ and defined $c_s = 2c_0$ with c_0 the salt concentration. Finally, the ionic current I_e and the voltage drop ΔV are linked as follows:

$$\boxed{L_{33} = \frac{I_e}{\Delta V} = \mu \left(c_s e h + 2\Sigma\right) \times \frac{w}{L}.} \tag{1.30}$$

Cross terms

Additionally to the direct terms, there are cross phenomena coming from couplings between hydrodynamics, ion diffusion and electrostatics. Using statistical mechanics, Onsager has shown the necessity of equality between the term L_{IJ} and L_{JI}. So in what follows, only three terms among the six cross coefficients are explicitly calculated, the last three being deduced from Onsager's relation.

$\mathbf{L}_{13}$ / $\mathbf{L}_{31}$ – The phenomenon by which a difference of electrical potential ΔV induces a water flow is called electro-osmosis (L_{13}). Its conjugate effect is called streaming current (L_{31}) and corresponds to the generation of an electric current by a pressure driven liquid-flow [54]. Hereafter, we will do explicit calculations for the case of electro-osmosis (L_{13}).

Electro-osmosis takes its origin in the ion dynamics within the Electrostatic Double Layer (EDL), in which the charge density $\rho_e = e(\rho_+ - \rho_-)$ is non-vanishing. The dynamics of the fluid is described by the stationary Stokes equation with a driving force for the fluid $F_e = \rho_e E_e$, where the electric tangential field E_e is defined as $E_e = -\partial_x V = -\Delta V/L$, and is directed along x [55]:

$$\eta \partial_z^2 u_x + \rho_e E_e = 0. \tag{1.31}$$

Using that the charge density is linked to the electrostatic potential of the EDL as follows:

$$\rho_e = -\epsilon \frac{\partial^2 V}{\partial z^2}, \tag{1.32}$$

one finds, after a double integration of the equation (1.31):

$$u_x(z) = \frac{\epsilon}{\eta}(V(z) - \zeta)E_e \tag{1.33}$$

where we used the no slip boundary condition and where ζ is the zeta potential, which is the value of the electrostatic potential at the shear plane, i.e. the position close to the wall where the velocity vanishes [5]. In the no-slip case, the zeta potential is equal to the surface potential V_s. As a remark, one can notice that in the case of a finite slip at the wall, characterized by a slip length b, the potential ζ takes the expression:

$$\zeta = V_s \times (1 + b\kappa_{\text{eff}}) \tag{1.34}$$

where V_s is the electrostatic potential at the wall and κ_{eff} the surface screening parameter ($\kappa_{\text{eff}} = -V'(z = 0)/V_s$). In the case of a weak potential, the screening parameter is approximately equal to the inverse of the Debye length λ_D. Note that the velocity in the fluid results from a balance between the driving electric force and the viscous friction force at the surface.

An integration of equation (1.33) gives the following expression for the total water flow:

$$Q = whU_{\text{EO}} - \text{surface correction terms}, \tag{1.35}$$

where U_{EO} is the eletro-osmotic velocity $U_{\text{EO}} = -\epsilon\zeta E_e/\eta$. Figure 1.6 shows

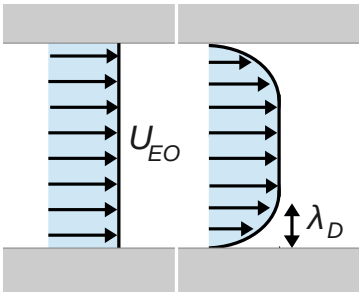

FIGURE 1.6: Schematic representation of the velocity profile, equation (1.33) without and with surface correction terms, respectively on the left and on the right.

a scheme of the velocity profile, with and without the surface correction terms. Finally, neglecting the surface correction terms (that are of the order of $\lambda_D/h \ll 1$), one can write:

$$\boxed{L_{13} = \frac{Q}{\Delta V} \approx \frac{\zeta\epsilon}{\eta} \times \frac{wh}{L}.} \tag{1.36}$$

[5] Notice that sometimes the zeta potential is defined as V_s and one has to consider an amplified electro-osmotic mobility to take into account the effect of slippage.

Hence electro-osmosis is caused by coulomb force and limited by viscous dissipation.

Accordingly, the streaming current (L_{31}), which is the electric current generated by a pressure driven liquid-flow can be written as:

$$\boxed{L_{31} = \frac{I_e}{\Delta P} = \frac{\zeta\epsilon}{\eta} \times \frac{wh}{L}.} \tag{1.37}$$

L_{12} / L_{21} – The generation of a flow under a solute gradient is called chemi-osmosis (L_{12}) [56]. Its conjugate effect is the generation of an excess flux of salt under a pressure drop Δp (L_{21}). Here the expression of the L_{12} coefficient is obtained in the case of a flow generated by a solute gradient.

So, let us assume the existence of a salt concentration difference Δc. The salt concentration in the middle of the channel, $c_{\text{mid}}(x)$, is assumed to vary linearly along the axis x: $c_{\text{mid}}(x) = c_0 + \Delta c \times x/L$, where c_0 is the concentration in the left reservoir (the concentration in the right reservoir being $c_0 + \Delta c$). From the mechanical equilibrium in z together with the Stokes equation along z, one can deduce the hydrostatic pressure profile:

$$p(x,z) = 2k_BTc_{\text{mid}}(x)\left[\cosh\phi(x,z) - 1\right] + p_0, \tag{1.38}$$

where $\phi(x,z) = e\beta V(x,z)$. Injecting this expression in the Stokes equation along x, $\eta\partial_z^2 u_x(z) - \partial_x p(x,z) = 0$, one finds:

$$\eta\partial_z^2 u_x(z) = 2k_BT\frac{\Delta c}{L}\left(\cosh\phi - 1\right). \tag{1.39}$$

Using Poisson-Boltzmann and assuming that $\lambda_D \ll h$, one can find that the flow is:

$$Q = whU_{\text{CO}} - \text{surface correction terms}, \tag{1.40}$$

with U_{CO} the chemi-osmotic velocity:

$$U_{\text{CO}} = -\frac{k_BT}{\eta}\frac{\ln(1-\gamma^2)}{2\pi\ell_B}\frac{\Delta c}{c_0 L}, \tag{1.41}$$

where $\gamma = \tanh(\phi_s/4)$. Neglecting surface correction terms (on the order of $\lambda_D/h \ll 1$), the coefficient L_{12} can be written:

$$\boxed{L_{12} = \frac{Q}{\Delta c} \approx -\frac{k_B T}{\eta c_0} \frac{\ln(1-\gamma^2)}{2\pi \ell_B} \times \frac{wh}{L}.} \tag{1.42}$$

Chemi-osmosis causes flow towards lower electrolyte concentration. As a complement we will discuss two interesting cases: the case of non-equal diffusion coefficient between + and − species, and the limit of large Debye length λ_D compared to the channel height h (this regime is called osmosis).

Supplement 1 – In the case of a difference in anion and cation diffusivities, an electric field is induced, and a supplementary electro-osmotic contribution has to be taken into account [57]. Assuming a vanishing local current in the outer region and a symmetric electrolyte, this diffusion-induced electric field is proportional to $\beta_0 = (D_+ - D_-)/(D_+ + D_-)$:

$$E^{\mathrm{D}} = \frac{k_B T}{e} \beta_0 \frac{\mathrm{d} \ln c}{\mathrm{d}x}. \tag{1.43}$$

So the contribution of this mechanism combined with the previously calculated velocity (equation (1.41)) gives the following diffusio-osmotic velocity:

$$U_{\mathrm{DO}} = -\frac{k_B T}{\eta} \left[\beta_0 \zeta \frac{\epsilon}{e} + \frac{\ln(1-\gamma^2)}{2\pi \ell_B} \right] \frac{\Delta c}{c_0 L}, \tag{1.44}$$

where we used equation (1.33). The first term corresponds to the electro-osmotic effect, the direction of the generated flow depending on the sign of the product $\beta_0 \zeta$, while the second term, called the chemi-osmotic effect, causes a flow towards the lower electrolyte concentration. Neglecting surface correction terms, one can write:

$$\boxed{L_{12} = \frac{Q}{\Delta c} \approx -\frac{k_B T}{\eta c_0} \left[\beta_0 \zeta \frac{\epsilon}{e} + \frac{\ln(1-\gamma^2)}{2\pi \ell_B} \right] \times \frac{wh}{L}.} \tag{1.45}$$

Supplement 2 – An interesting case is the limit where the Debye length λ_D is much larger than the channel height h. In this particular case, a constant potential (independent of z) called Donnan potential V_D builds up

in the entire channel. From the electro-chemical equilibrium one gets:

$$\frac{c_+}{c_-} = e^{-2\phi_D}, \tag{1.46}$$

$$c_+ c_- = c_0^2, \tag{1.47}$$

$$c_+ - c_- = -\frac{2\Sigma}{eh}, \tag{1.48}$$

where $\phi_D = e\beta V_D$. One can introduce the Dukhin number $\mathrm{Du} = \Sigma/(ec_0h)$. Then from equation (1.48), and using that $\cosh^2(x) - \sinh^2(x) = 1$, one gets

$$\cosh(\phi_D) = \sqrt{1 + \mathrm{Du}^2}. \tag{1.49}$$

Injecting this expression in equation 1.39, which has been obtained from mechanical equilibrium in z together with the Stokes equation, one gets

$$Q = -\frac{1}{12\eta}\frac{wh^3}{L} \times \Delta\Pi, \tag{1.50}$$

where the osmotic pressure $\Delta\Pi$ can be written as

$$\Delta\Pi = 2k_BT\Delta c\left(1 + \sqrt{1 + \mathrm{Du}^2}\right). \tag{1.51}$$

Hence, when $\lambda_D \gg h$, one may write

$$\boxed{L_{12} = \frac{Q}{\Delta c} = -\frac{k_BT}{6\eta}\left(1 + \sqrt{1 + \mathrm{Du}^2}\right) \times \frac{wh^3}{L}.} \tag{1.52}$$

$\mathbf{L_{23}}$ / $\mathbf{L_{32}}$ – The current generated under a salt concentration gradient is called osmotic current and the reciprocal effect is the generation of a salt flux under an electrical potential gradient. The expression of $\mathrm{L_{23}}$ is here obtained in the first case, i.e. in the case of the generation of current under a salt concentration gradient.

The electrical current I_e can be written as

$$I_e = w\int_{-h/2}^{h/2} e\left(j_+(z) - j_-(z)\right)\mathrm{d}z. \tag{1.53}$$

Two contributions to the current can be expected, a contribution from the diffusive flux of salt and a contribution from the convective flux of salt. The

first one can be written as

$$I_D = w \int_{-h/2}^{h/2} e \left(j_{D,+}(z) - j_{D,-}(z) \right) \mathrm{d}z, \tag{1.54}$$

with $j_{D,\pm} = -D_\pm \nabla c_\pm$ the diffusive flux of each ion. Assuming that $D = D_+ = D_-$ and rewriting the current as

$$I_D = -ew\partial_x \int_{-h/2}^{h/2} \left(c_+(z) - c_-(z) \right) \mathrm{d}z, \tag{1.55}$$

I_D appears to be equal to zero from the global charge electroneutrality

$$\Sigma + e \int_{-h/2}^{h/2} \left(c_+(z) - c_-(z) \right) \mathrm{d}z = 0. \tag{1.56}$$

Accordingly, considering the convective part in equation (1.53) only, the current can be written as

$$I_e = w \int_{-h/2}^{h/2} e \left(c_+(z) - c_-(z) \right) u_x(z) \mathrm{d}z, \tag{1.57}$$

where both species $\pm$ move at the same velocity $u_x(z)$ (i.e. there is no electric field along z). Using that $\lambda_D \ll h$ (thin electric debye layers as compared to the channel width), one writes:

$$I_e = 2w \int_{0}^{\infty} e \left(c_+(z) - c_-(z) \right) u_x(z) \mathrm{d}z. \tag{1.58}$$

In this assumption, one expects that the entire contribution to the current I_e comes from the convection of ions inside the electric double layers. From the Poisson equation (1.6), one gets that

$$c_+(z) - c_-(z) = -\frac{\partial^2 \phi}{\partial z^2} \frac{1}{4\pi \ell_B}. \tag{1.59}$$

Moreover, we know from previous section (see equation (1.39)) that the velocity field $u_x(z)$ under a solute gradient is solution of

$$\eta \frac{\partial^2 u_x}{\partial z^2} = 2 k_B T \frac{\Delta c}{L} \left(\cosh \phi - 1 \right). \tag{1.60}$$

Injecting equation (1.59) in equation (1.58), performing an integration by part (twice) in the spirit of [58], one gets

$$I_e = \frac{we}{2\pi\ell_B}\left[\phi\frac{\partial u_x}{\partial z}\right]_0^\infty - \frac{we}{2\pi\ell_B}\int_0^\infty \phi\frac{\partial^2 u_x}{\partial z^2}\mathrm{d}z. \tag{1.61}$$

From equation (1.60), one get

$$\left.\frac{\partial u_x}{\partial z}\right|_{z=0} = -\frac{2k_BT}{\eta}\frac{\Delta c}{L}\int_0^\infty (\cosh\phi - 1)\,\mathrm{d}z. \tag{1.62}$$

Hence, using that $\phi(z=\infty)=0$, one gets

$$I_e = -\frac{we}{\pi\ell_B}\frac{k_BT\Delta c}{\eta L}\int_0^\infty (\phi_s - \phi)\times(\cosh\phi - 1)\mathrm{d}z. \tag{1.63}$$

with ϕ_s the normalized surface potential. Using PB equation $\nabla^2\phi = \kappa^2\sinh\phi$, we make the following change of variable:

$$\mathrm{d}z = -\frac{\mathrm{d}\phi}{\kappa\sqrt{2(\cosh\phi - 1)}}, \tag{1.64}$$

which allows to solve the integral in equation (1.63). One finds [58]:

$$I_e = 2w\frac{e}{\pi\eta\ell_B}\frac{k_BT}{\kappa}\left(2\sinh\frac{\phi_s}{2} - \phi_s\right)\frac{\Delta c}{L}, \tag{1.65}$$

that can be rewriten in terms of surface charge (using $2\sinh\phi_s/2 = e\Sigma/\epsilon k_BT\kappa$):

$$I_e = 2w\Sigma\frac{k_BT}{2\pi\eta\ell_B}\left(1 - \kappa\ell_{GC}\,\mathrm{argsinh}\frac{1}{\kappa\ell_{GC}}\right)\frac{\Delta c}{Lc_0}, \tag{1.66}$$

where we have introduce the Gouy-Chapmann length $\ell_{GC} = e/(2\pi\Sigma\ell_B)$. Neglecting the surface correction terms one finds:

$$\boxed{L_{23} = \frac{I_e}{\Delta c} \approx 2w\Sigma\frac{k_\mathrm{B}T}{2\pi\eta\ell_\mathrm{B}}\frac{1}{Lc_0}} \tag{1.67}$$

Reciprocally, the flux of salt under electrical gradient can be written as:

$$\boxed{L_{32} = \frac{J_i}{\Delta V} \approx 2w\Sigma\frac{k_\mathrm{B}T}{2\pi\eta\ell_\mathrm{B}}\frac{1}{Lc_0}} \tag{1.68}$$

Various comments

We did not give an exhaustive list of phenomena that can occur at the nanoscale. For example thermic effects induced by temperature difference have not been discussed.

Notice that in practice, it is not easy to study each case alone. For example, a charged channel submitted to a difference of electrical potential will be subjected to various flux, leading to a charge accumulation at each entrances, i.e. the apparition of an induced salt difference. This is part of the complexity of nanofluidics.

1.3 Announcement of the plan

We just showed an overview of the complexity and richness of nanofluidics which is, in part, due to the large number of forces that apply as well as the numerous characteristic lengths that over-cross each other at this scale. In this context, and considering that nanofluidics is a quite recent field, a large range of issues remained unexplored at the beginning of this thesis, and most of them still are. Here we list the questions we address in this manuscript. All of them are closely related to nanofluidics and most of them have been assessed using the finite element method or molecular dynamics simulations. For the purpose of this thesis, we have chosen to regroup them into five chapters (the first one being the introduction) that can be read independently. **The second chapter** describes our work concerning hydrodynamic transport through a nanopore that focuses on the viscous dissipation arising at each entrance. Inspired by the aquaporin, an hourglass-shaped nanopore, we explored the role of the geometry on the overall hydrodynamic permeability of a nanopore, using both continuum hydrodynamics and molecular dynamics simulations. **The third chapter** is a study of subcontinuum capillary filling. We tested the validity of continuum predictions in subnanometric nanopores in which the granularity of the fluid is expected to play a role. **The fourth chapter** presents our work on nanofluidic diodes, an asymmetrically charged nanopore which presents rectified force-flux response. We explored the possibility of using a nanofluidic diode to control the solvent flow. Moreover, the possibility of rectifications in the absence of a full electrical double layer overlap was considered. Finally, **the fifth chapter** is a study of the fluctuations inside a nanopore. The goal was to explain the origin of the mysterious low frequency pink noise commonly observed in the power spectral density of ionic current. We found, using both molecular dynamics simulations and an analytical model, that the combination of reversible adsorptions of particles in surface and diffusion can lead to pink noise, and constitutes a serious candidate to explain its origin.

Note: the choice has been made not to include the experimental work on the permeability of solid state nanopore using FCS, see Ref. [59] for details.

Chapter 2

Optimizing water permeability through the hourglass shape of aquaporins.

Contents

This chapter is based on the following publications:

- Simon Gravelle et al. Optimizing water permeability through the hourglass shape of aquaporins. *Proceedings of the National Academy of Sciences* 2015 [60]
- Simon Gravelle et al. Large permeabilities of hourglass nanopores: From hydrodynamics to single file transport. *The Journal of Chemical Physics* 2014 [61]
- Simon Gravelle et al. Perméabilité optimale des aquaporines: une histoire de forme? *Médecine/Sciences* 2015 [62]

Abstract and main results – Optimizing the permeability of nanoporous membranes is of main importance in various domains, such as desalination, water filtration or energy conversion. At the nano-scale, the limitation of fast transport is usually governed by viscous dissipation, which has two possible origins: friction at the walls of the pore and entrance effects coming from the connection between the pore and the reservoirs. Materials that present a low solid/liquid friction, such as graphene, have been widely studied for the last decade. But entrance dissipation also needs to be studied, in order to reduce it as much as possible.

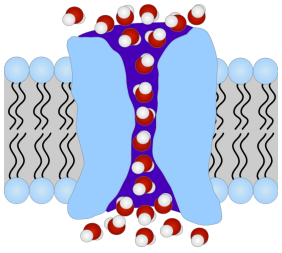

A

Our research was inspired by a natural hourglass-shaped nanopore called aquaporin, schematized in figure A. This protein is known to present a high water permeability and ensures water exchanges between the biological compartments inside mammalians, microorganisms or plants. Aquaporin is expected to face large entrance dissipation due to its dimensions. Because of its very peculiar shape of hourglass, we explored the possible connection between geometry and entrance effects (see a typical shape on figure B). We used classical hydrodynamics and molecular dynamics simulations to study the water flow in a biconical channel and explored the impact of the conical entrances on the flow permeability.

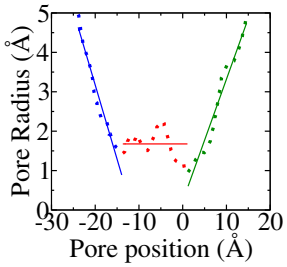

B

We found that hourglass nanochannels reduce significantly the entrance effects, with comparison to cylindrical channels. We also observed that, for a given pore dimension, there is one specific cone's angle that optimizes the water flow (see figure C), and that this angle is close to the angle observed in natural aquaporins. Our results show that aquaporins, due to their geometry, are well built to face entrance dissipation, and accordingly, to optimize the water flow. It is remarkable that hydrodynamics may contribute to ruling molecular channel characteristics.

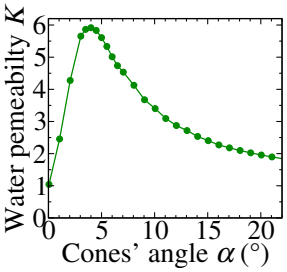

C

2.1 Introduction

2.1.1 State of the art

End effects in pipe flow have been discussed a century ago by Sampson who calculated the flow resistance across a circular pore in an infinitely thin membrane, within the framework of continuum hydrodynamics [63]. It has then been generalized to circular cylinder by Weissberg [64] in 1962, and Dagan et al. [65] in 1982. Then, during the next 30 years, entrance effects seem to have been forgotten by the nanochannel flow literature. For example, during the 2000s, Majumder et al. [10, 66], Holt et al. [11] or Du et al. [67] reported flow rate through carbon nanotubes 100-100,000 times greater that what have been measured for any other material. They choose to accommodate their results with theory by using small value for the friction parameter along the channel length, while their systems, due to their dimensions, clearly require significant end corrections. It was not until 2011 that Sisan and Lichter published *The end of nanochannels* [68], in which the authors remind us the existence of end effects, corresponding to viscous losses within the liquid near the channel's entrances. Notice that the same year (and apparently independently), Nicholls et al. [29] reported simulations of flow through CNTs and highlighted the importance of entrance effects.

In some cases, depending on both pore dimension and hydrodynamic boundary conditions, entrance effects may be significant, and sometimes may even govern the flow. For example, entrance effects are of main importance for long low-friction channels such as carbon nanotubes for which numerical simulations predict vanishing friction along walls for smallest radius [69]. Furthermore, entrance effects also govern the transport across thin membrane, such as pierced graphene [70]. Entrance effects provide a lower limit to the dissipation, and therefore to the speed at which liquid is transported. Consequently, flow rates measured by Majumder and Holt are larger that what is theoretically allowed, as noticed by Sisan and Lichter [68].

Since entrance effects have only been re-discovered recently, no study has been performed on the coupling with partial boundary condition for example. Also, as far as we know, no study has been performed to explore the role of

the geometry on entrance dissipation. This is the purpose of the present chapter.

2.1.2 Definition

In the framework of weakly out-of-equilibrium systems, the hydrodynamic resistance R characterizes flow transport across a given structure, and is defined as the ratio between the pressure drop ΔP and the corresponding flow rate Q between two reservoirs connected by the structure:

$$R = \frac{\Delta P}{Q}. \tag{2.1}$$

Notice that R is linked to the hydrodynamic permeability K, defined in chapter 1 (K=L_{11}), as $R = K^{-1}$. A nanopore can be considered as two "hydrodynamic resistances" put in series. While the flow rate Q is conserved through the circuit, the pressure drop accumulates throughout the two hydrodynamic resistors: $\Delta p = \Delta p_{\mathrm{in}} + \Delta p_{\mathrm{out}}$, where $\Delta p_{\mathrm{in}} = R_{\mathrm{in}} Q$ is the pressure drop inside the pore, and $\Delta p_{\mathrm{out}} = R_{\mathrm{out}} Q$ the total access pressure drop (sum of inlet and outlet pressure drops). R_{in} and R_{out} are the corresponding hydrodynamic resistances. In the absence of liquid/solid slip, the intrinsic resistance of a pore is given by the Poiseuille law [71]:

$$R_{\mathrm{in}}^{\text{no-slip}} = \frac{\Delta p_{\mathrm{in}}}{Q} = \frac{8\eta L}{\pi a^4}, \tag{2.2}$$

a is the radius of the pore, L is its length and η the fluid's viscosity. Liquid/solid slip inside the pore reduces friction. In the case of a partial slip boundary condition, characterized by a slip length b (see chapter 1), the velocity field at the surface obeying $b\,\partial_n v_t|_{\mathrm{surf}} = v_t|_{\mathrm{surf}}$, with v_t the tangential component of the velocity and n the normal component to the surface. As a consequence, the hydrodynamic resistance is reduced as follows [72]:

$$R_{\mathrm{in}}^{\mathrm{slip}} = \frac{R_{\mathrm{in}}^{\text{no-slip}}}{1 + 4b/a}. \tag{2.3}$$

In the case of a large slip length (corresponding to high-permeability pores), i.e. $b \gg a$, the velocity profile will be almost flat (plug flow), and the

resistance simplifies to:

$$R_{\text{in}}^{b\gg a} = \frac{8\eta L}{\pi a^4} \times \frac{a}{4b} = \frac{2\lambda L}{\pi a^3}. \tag{2.4}$$

where $\lambda = \eta/b$ is the friction coefficient. In this "plug-flow" regime, viscosity does not play a role, and R_{in} is only controlled by λ. Finally, one can note that R_{in} vanishes in the limit of a perfect slip BC ($\lambda = 0$). On the other hand, the access resistance is given by a simple scaling law. The pressure drop Δp and the flow rate Q are linked by $\Delta p \sim \eta Q/a^3$ (from a dimensional analysis), with a the aperture radius, η the liquid dynamic viscosity. Using the notations first introduced by Sampson in 1891, we write [63]:

$$\Delta p = \frac{C\eta}{a^3} \times Q, \tag{2.5}$$

with C a dimensionless coefficient, called the Sampson coefficient. Sampson calculated the exact solution for the Stokes flow through a circular aperture in an infinitely thin membrane and found that the coefficient C is equal to 3 in this particular case. An exact calculation in the case of a converging flow into a cylindrical pore have shown that equation (2.5) with $C = 3$ provides a very good estimate of the access pressure drop [64, 65]. The total pressure drop Δp is therefore related to the flow rate Q by:

$$\Delta p = (R_{\text{in}}^{b\gg a} + R_{\text{out}})Q = \left(\frac{2\lambda L}{\pi a^3} + \frac{C\eta}{a^3}\right) Q. \tag{2.6}$$

In the large slip limit, R_{in} and R_{out} share the same scaling with the pore radius. Therefore, *independently of the pore radius* (providing that $a \ll b$), the access resistance will become the limiting factor for a tube length below the critical pore length L_0 defined as:

$$L_0 = \frac{\pi C\eta}{2\lambda} = \frac{\pi C}{2} b. \tag{2.7}$$

If $L \gg L_0$, $R_{\text{in}} \gg R_{\text{out}}$: the pressure will drop linearly along the tube, with a negligible contribution from the entrances. On the contrary, if $L \ll L_0$, $R_{\text{in}} \ll R_{\text{out}}$: the pressure drop will be concentrated at the inlet and outlet, and the pressure will be almost constant along the pore. This was observed in previous MD works [70], and can be explained in the framework of continuum hydrodynamics. This could be used as a new definition of pore

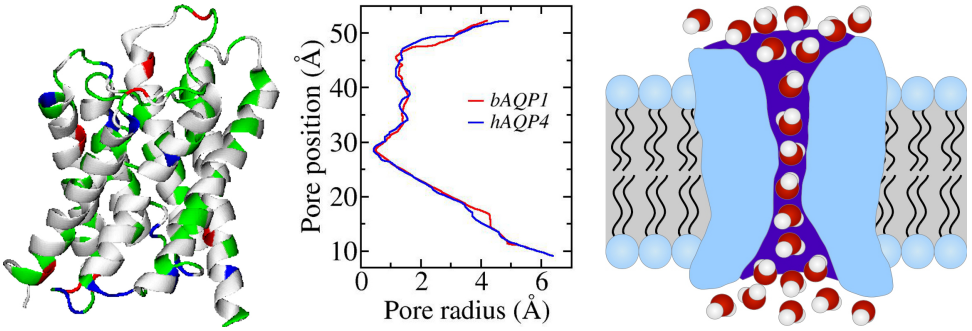

FIGURE 2.1: Left: molecular structure of human aquaporin 4 (hAQP4) obtained from the Protein Data Bank [73] and plotted with VMD [74]. Middle: profiles of two aquaporins collected from reference [75]. The pore dimensions were estimated using the HOLE program [76]. Right: scheme of an aquaporin included in a lipidique membrane, separating two reservoirs and crossed by water molecules.

and channel.

2.1.3 Aquaporins and motivations

One major motivation of our work on entrance effects come from the observation of the shape of some highly efficient, ubiquitous and natural water filter named aquaporin, see figure 2.1. This protein plays a fundamental role in osmotic water regulation, which is essential for all life forms [16, 17]. While dissipation in the inner part of aquaporin has not been fully characterized, a simple estimate nevertheless shows that entrance effects contribute for a large part to the global hydrodynamic resistance. Indeed, formula (2.5) gives a predicted hydrodynamic entrance resistance $R^{\text{th}} \sim$ 0.5-3 $\times 10^{27}$ Pa.s/m^3 while the measured hydrodynamic resistance of aquaporin can be extracted from physiology literature $R^{\text{exp}} \sim$ 1-3 $\times 10^{27}$ Pa.s/m^3 [1]. This indicate that entrance effects are most probably a major contribution on the overall hydrodynamic transport inside aquaporins.

For this study, two major pieces of information are extracted from X-ray profiles. First, as seen in figure 2.1, X-ray profiles highlight the quasi-hourglass shape of aquaporins, that can be approximated as one central

[1] The permeabilities of Aqp reported in the literature vary typically in the range $p_f = 0.5$ to 1.5×10^{-19} m^3/s [77]. The permeability p_f is defined in the physiology literature from the flux of water Φ_w (in moles per unit time) resulting from an osmotic pressure difference $\Delta\Pi$ across the pore, as $p_f = \Phi_w \mathcal{R}T/\Delta\Pi$, with $\mathcal{R}$ the gas constant [78]. It is related to the hydrodynamic permeability K defined as the ratio of the flow rate and pressure drop, as $p_f = K \times \mathcal{R}T/\mathcal{V}_w$, with $\mathcal{V}_w$ the molar volume of water.

channel connected to two truncated cones. This motivates the exploration of the impact of conical entrances on hydrodynamic dissipation, which is the main goal of the present study. Furthermore, X-ray profiles also indicate that aquaporins present dimensions down to $1 - 2\,\text{Å}$. For such dimensions, continuum hydrodynamics is expected to fail [2], and a complete study of transport through aquaporin-inspired channels requires a molecular study, which will be performed hereafter.

2.1.4 Outline

In this chapter we present a study of hydrodynamic entrance effects. The impacts of both hydrodynamic boundary condition and pore's geometry on the hydrodynamic permeability of a nanopore are considered. In the first part, we study a flow through a cylindrical geometry, inspired by carbon nanotube (CNT), and explore the impact of both the hydrodynamic boundary condition and entrances smoothness on the hydrodynamic permeability. In the second part, we study a flow through a hourglass shaped nanochannel, inspired by aquaporins, and discuss the role of the conical entrances. In both cases (CNT-like and AQP-like channels), our approach is the following: we first study hydrodynamics at the continuum level using the finite element method. Then, we test the robustnesss of continuum results at the molecular scale, using molecular dynamics simulations, since a breakdown of continuum hydrodynamic is expected for subnanometric system.

2.2 Cylindrical nanopore: mimiking a CNT

As a first step, we studied hydrodynamics through a cylindrical nanopore. The entrance resistance of a cylindrical nanopore with the no-slip boundary condition is well described by the Sampson formula 2.5 with $C = 3$. But *real* cylindrical nanotubes such as CNTs are known to be very slippery, and one may expect some changes for the entrance resistance. Moreover, the hydrodynamic boundary condition is expected to apply at approximately

one molecular size within the fluid, which leads to effective smooth entrances for smaller tubes. An influence of this smoothness on hydrodynamic permeability is expected, and is discussed hereafter as well.

2.2.1 Finite element calculations

As a first approach, we used finite element calculations to study water flowing through a solid nanopore [2]. We solved the Stokes equation $\eta\Delta\vec{v} = \vec{\nabla}p$ with the proper hydrodynamic boundary condition in a 2D-axisymmetric geometry. The nanopore was connected to two reservoirs of characteristic size L_r [3]. Far from the pore, we imposed a difference of pressure Δp between the two reservoirs and then measured the water flow Q across the tube. The hydrodynamic resistance of the pore was then deduced from $R = \Delta p/Q$. A typical system is presented in figure 2.2.

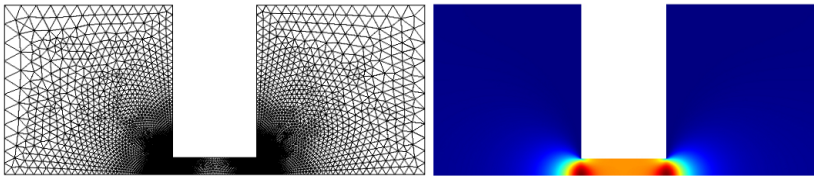

FIGURE 2.2: Left: example of a meshed system made with Comsol and used for the resolution of the Stokes equation. Right: velocity profile of the flow through a cylinder (red: high velocity, blue: low velocity).

2.2.2 Role of hydrodynamic boundary conditions

Before considering the impact of geometry on entrance effects, we studied the role of hydrodynamic boundary conditions. It is well known that the inner resistance (Poiseuille) strongly depends on the slip length b, but as far as we know, the impact of slippage on the entrance dissipation had not been studied at the beginning of this thesis. With a no-slip boundary condition, it has been shown that the entrance resistance in a cylinder is well described by Sampson formula: $R = C\eta/a^3$, with C equal to 3 regardless of the length of the cylinder [64]. To go further, we considered here the case of

[2] calculations made with the commercial software COMSOL

[3] We checked that a characteristic size of reservoir $L_r \sim 10a$, with a the pore radius, ensures an error of ca. 0.25 %.

a perfect slip boundary condition. We used the system presented in figure 2.3 with a slip length $b = \infty$ (perfect slip boundary condition). The ratio

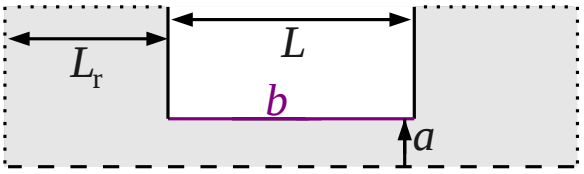

FIGURE 2.3: System used for finite element calculations. The slip b was taken to be infinite of null.

of length L over radius a was varied, while measuring the hydrodynamic resistance of the system. Then, the value of the C coefficient was deduced, see figure 2.4. For very short tubes, the boundary condition at the inner wall becomes irrelevant, and Sampson's result for the infinitely thin membrane is recovered with $C = 3$. As the tube gets longer, however, the C coefficient increases up to a plateau value of $C_\infty \approx 3.75$, implying that switching from no-slip to perfect slip inside the tube yields a 25% *increase* in the access resistance. Though counter-intuitive at first sight, this behaviour can be qualitatively understood by examining the flow profile at the channel end. In the no-slip case (figure 2.4), this "entry" flow profile is, to a very good approximation, halfway between the parabolic profile of Poiseuille flow and the elliptic profile found in Sampson's solution [65]. As a result, the transition to a plain parabolic profile inside the channel involves only a small dissipation. Because the velocity must vanish at the corner, the

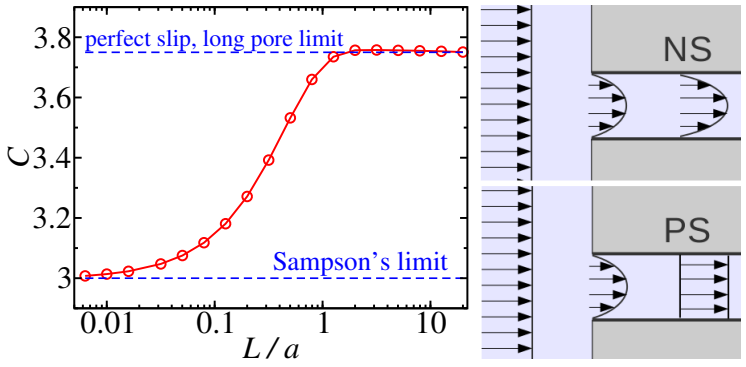

FIGURE 2.4: Left: $C = Ra^3/\eta$ (see text) as a function of the pore length L for a perfectly slipping cylindrical channel, obtained with FE calculations (points). The red line is a guide for the eyes. Right: schematic profiles of axial velocity in a channel with no slip (NS) and perfect slip (PS) boundary condition. From left to right: outside far field, entry profile and inside far field.

entry profile in the perfectly slipping tube is quite similar to the no-slip

case, suggesting a comparable amount of viscous losses outside the tube. Now, inside a tube with the perfect slip at the boundaries, the transition to a plug profile requires a significant reorganization of the streamlines (figure 2.4), resulting in a higher dissipation, hence a higher coefficient C. As a side remark, we find that the BC on the external wall has a negligible impact on the access resistance, presumably because any slip that could happen there is strongly hampered by the vanishing velocity at the corner.

2.2.3 Smooth entrances: what consequence?

After having considered the impact of the hydrodynamic boundary condition on the entrance dissipation, one may wonder what is the influence of the channel geometry. Indeed, when studying water flow in a large tube (radius > 1 nm) one may consider that the hydrodynamic radius a_{eff} (i.e. the radius effectively seen by the fluid) and the radius defined by the position of atoms wall a_{c} are the same. In this case, the tube can be considered as a cylinder with sharp entrances and with a well defined radius $a = a_{\text{eff}} = a_{\text{c}}$. But, when considering extremely small tubes, for example a CNT with a radius close to the molecular diameter (below 1 nm), the position where the hydrodynamic boundary condition applies has to be questioned. Typically, one expects the hydrodynamic boundary condition to applies within the fluid at a distance of $\sim \sigma_{OC}$, i.e. one molecular size from the wall [79]. This has two consequences: first, the effective radius of the tube is smaller than the radius defined by the position of atom's wall: $a_{\text{eff}} \approx a_c - \sigma_{OC}$. Second, the entrances of the tube are smooth ($\sim$ chamfered with a chamfer of radius σ_{OC}). At the level of a continuum description, this is expected to modify the Sampson coefficient C in the equation: $\Delta p/Q = C\eta/a^3$.

Figure 2.5 shows the system used for finite element calculations. Along membrane and tube walls we used perfect the slip boundary conditions. This choice has been motivated by simulation showing a vanishing friction along CNT's wall for small radius [69]. We explored a large range of radius a_{eff} for fixed $a_{\text{c}} - a_{\text{eff}}$. Figure 2.6 shows the effect of the aspect ratio on the value of the C coefficient, for 2 different membrane thicknesses. As we can see, for a ratio $a_{\text{eff}}/(a_{\text{c}} - a_{\text{eff}}) \approx 1$, which corresponds to a (5,5) armchair tube, C is around 1.5 instead of 3.75, corresponding to a 60 % improvement of the pore

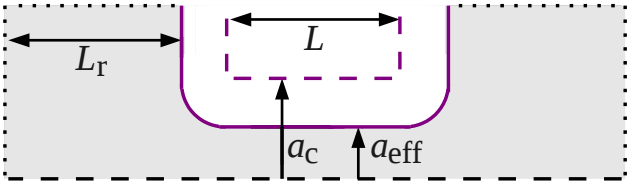

FIGURE 2.5: Cylindrical geometry used for FE calculations. Two reservoirs of size L_r are separated by a membrane pierced by a channel of radius a_{eff} and length L . The black dashed line correspond to an axisymmetric boundary condition. The full line represent the liquid/solid interface. The pressure was imposed on the dotted lines.

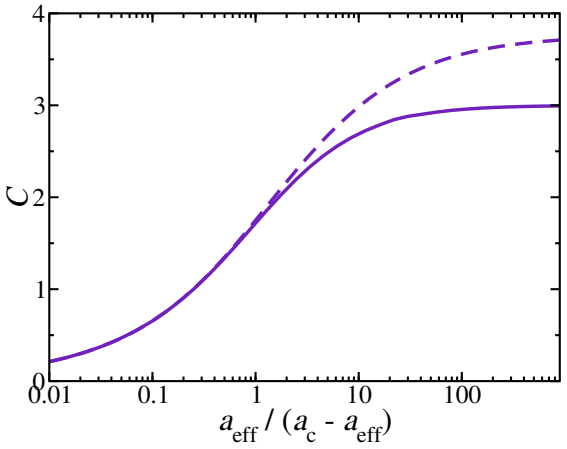

FIGURE 2.6: Measured Sampson coefficient as a function of the ratio between the effective radius a_{eff} and the chamfer radius $a_c - a_{eff}$. Nanotube limit $L/a_{eff} = 5$ (long dashed line), atomically thin membrane nanopore limit $L = 0$ (solid line).

permeability. Continuum hydrodynamics indicates that pore geometry may impact the entrance resistance. Those predictions are expected to be quite robust for a system with characteristic dimensions above one nanometer, but deviations are expected for a system with dimensions below one nanometer [2]. Molecular dynamics simulations are required to test the robustness of the present result, and are presented hereafter.

2.2.4 Molecular dynamics simulations

The goal of the present section is to test the validity of the previous results obtained with continuum hydrodynamics, and accordingly to test the validity of Sampson's formula $R = C\eta/a^3$, where the value of C is presented in figure 2.6. To do so, we performed molecular dynamics simulations of water flow inside a cylindrical nanotube. Molecular dynamics simulations were

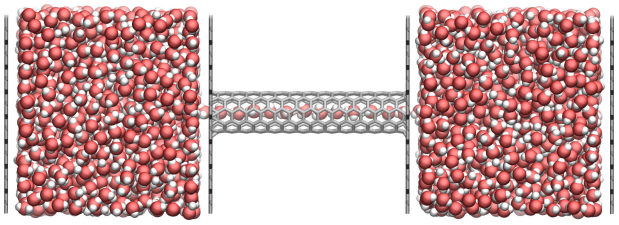

FIGURE 2.7: Snapshots of considered system: tube armchair (6,6). Oxygen atoms are colored in red, hydrogen atoms in white, and carbon atoms in grey.

performed in the geometry depicted in figure 2.7: two water reservoirs are separated by a membrane consisting of two parallel graphene sheets, and pierced with a carbon nanotube (CNT). The radius a_c of the CNT is defined by the center of carbon atoms, and the length L of the CNT was $L = 10 \times a_c$. Nanotubes were made by rolling a graphene sheet with respect to unit-cell. Tube radius a_c were varied from 25 Å down to 3.5 Å. Both armchair and zigzag nanotubes were considered.

Simulations details– The Amber96 force field [80] was used, with TIP3P [81] water and water-carbon interaction modeled by a Lennard-Jones potential between oxygen and carbon atoms, with parameters $\varepsilon_{OC} = 0.114\,\text{kcal/mol}$ and $\sigma_{OC} = 3.28\,\text{Å}$. There were no need to define a potential between carbon atoms since they were fixed. Simulations were performed using LAMMPS [82]. Long-range Coulombic interactions were computed using the particle-particle particle-mesh (PPPM) method [83, 84], and water molecules were held rigid using the SHAKE algorithm [85]. The equations of motion were solved using the velocity Verlet algorithm with a timestep of 2 fs. Water molecules were kept at a temperature of 300 K using a dissipative particle dynamics (DPD) thermostat [86]. This amounts to adding pairwise interactions between atoms, with a dissipative force depending on the relative velocity between each pair and a random force with a Gaussian statistics. This method has the advantage of preserving hydrodynamics, even for complex 3-dimensional flows as the ones considered here. The amplitude of the dissipative term was carefully tuned to ensure that the liquid viscosity is negligibly affected by the thermostat (this thermostating method was extensively tested and compared to other approaches in a previous work [72]). The positions of the carbon atoms of the membrane were fixed (simulations with flexible and fixed walls were shown to give similar results for the statics and friction of confined liquids [87–89]). Two pistons made of graphene

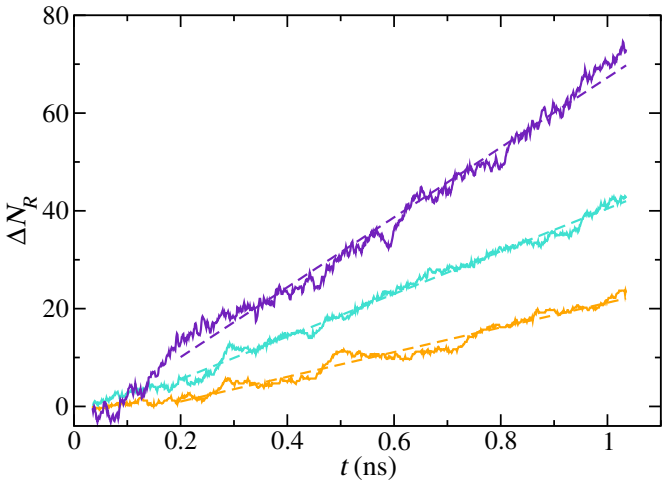

FIGURE 2.8: Number of crossing water molecules toward the right reservoir ΔN_R as a function of time, for different tube radii a_c ($a_c = 3.51$ Å in orange, 4.31 Å in cyan, and 4.69 Å in purple). Full lines represent the MD results and dashed lines are linear fits.

sheets were used in order to maintain each reservoir at the desired pressure. The periodic boundary conditions were imposed in all directions. In order to avoid hydrodynamic interactions between the tube and its periodic images in the plane of the membrane, a box with lateral dimensions (x,y) equal to 10 times a_c was used. We also made sure that reservoirs were bigger than 10 times a_c along z. Finite element calculations indicate that, in that configuration, the error due to finite size effects should be lower than 0.25 %. There were 3.2 k water molecules and 2.7 k carbon atoms for the smallest system ($a_c = 3.5$ Å), and 800 k water molecules and 78 k carbon atoms for the biggest system ($a_c = 25$ Å).

Water molecules were initially disposed on a simple cubic lattice with equilibrium density. Pressure differences were imposed using the reservoir pistons, and a steady-state flow quickly appears, within less than 200 ps (see figure 2.8). Note that this timescale matches the expected time for momentum diffusion in reservoirs, in agreement with the dominant role of the entrance resistance. We then measured the steady-state flow rate by counting the number of water molecules crossing the tube. This is shown in figure 2.8 for several tube radii under a given pressure drop.

Independently from the above calculation, we also calculated the slip length of water on a graphene sheet. To this end, we performed simulations of Couette and Poiseuille flows of water confined between two graphene planes,

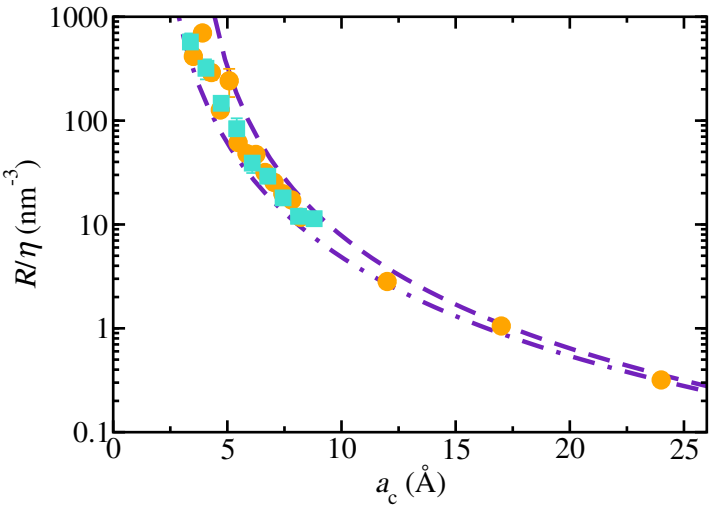

FIGURE 2.9: Resistance of a single nanotube $R = \Delta P/Q$, normalized by the bulk liquid viscosity η, as a function of the radius a_c of the tube. Circles represent MD results with armchair tubes, squares represent MD results with zigzag tubes. Lines are hydrodynamic predictions using FE calculations, for $a_c - a_{\text{eff}} = 3.2\,\text{Å}$ (dashed dotted line) and $a_c - a_{\text{eff}} = 1.7\,\text{Å}$ (dashed line).

in line with previous work [90, 91]. We measured a quite large slip length $b = 123 \pm 21\,\text{Å}$. This means that tubes with nanometer range diameters can be considered as perfectly slipping. We also measured the water viscosity, and found it to be equal to $0.31 \pm 0.02\,\text{mPa.s}$, in good agreement with the expected value of $0.31\,\text{mPa.s}$ for the TIP3P model at $300\,\text{K}$ [92].

Data acquisition – The flux Q was deduced from the linear fit of the time dependent variation of the number of crossing water molecules $\Delta N_R(t)$: $Q = M/(\rho \mathcal{N}_\text{A}) \text{d}\Delta N_R/\text{d}t$, with M and ρ the molar mass and density of water, and $\mathcal{N}_\text{A}$ the Avogadro constant. Finally, the hydrodynamic resistance was computed as $R = \Delta P/Q$. For each geometry we ran a number (up to 10) of independent simulations from different initial conditions, in order to estimate and reduce statistical uncertainties. The production times ranged from $\sim 1\,\text{ns}$ for the largest pores, to $\sim 6\,\text{ns}$ for the smallest ones. Although the results presented in this article were obtained for a pressure drop of $1000\,\text{atm} - 1\,\text{atm}$, we emphasize that linearity between flux and pressure drop has been checked systematically in all our simulations.

Results – We plotted in figure 2.9 the resistance normalized by the bulk viscosity of the TIP3P model, R/η, as a function of the tube radius a_c. These data were compared with continuum predictions obtained using FE calculations in the same geometry. We used two different values for the

hydrodynamic pore radius: one where the perfect slip hydrodynamic BC is located right at the surface of carbon atoms, i.e. $a_c - a_{\text{eff}} = \sigma_c/2 \approx 1.7\,\text{Å}$; and the other where the perfect slip hydrodynamic BC is located at the first layer of water along the wall $a_c - a_{\text{eff}} \approx \sigma_{OC} \approx 3.2\,\text{Å}$, in line with results from reference [79, 90]. As shown by Figure 2.9, we obtain a very good agreement between the MD results and the continuum hydrodynamic predictions. In line with previously quoted expectations, we found that a reasonable choice for the value of the hydrodynamic radius is $a_{\text{eff}} \simeq a_c - 2.5\,\text{Å}$. Note that nanotube's chirality has no significant influence on entrance effects. It is particularly interesting to observe that the hydrodynamic prediction is valid for nanotubes with effective radii well below one nanometer, even when single file transport occurs. In such case, we expect a full breakdown of hydrodynamics inside the tube. However, entrance effects originate mainly from the bending of the streamlines *outside* the tube, which occurs in the bulk on length scales larger than the tube radius. This certainly explains the robustness of hydrodynamics to predict entrance effects.

2.3 Nanopore with conical entrances: mimiking an AQP

The study of a cylindrical nanochannel indicates that both the hydrodynamic boundary condition and the geometry impact the entrance dissipation. The entrance dissipation will ultimately limit the performance of an ideal channel, and one may wonder if it is possible to reduce it. Inspired by the aquaporin (AQP) shape (figure 2.1), we investigated hydrodynamic entrance effects in hourglass shaped nanopores. The first part presents a continuum study of the role of conical entrances on the hydrodynamic permeability. Then, we present a simple analytical model with the aim of describing the entrance resistance of a hourglass shaped nanopore. Then we compare our continuum prediction with real aquaporins. Finally, since continuum hydrodynamic is expected to fail to describe systems below one nanometer, we test the robustness of our results at the molecular level using molecular dynamics simulations.

2.3.1 Finite element calculations: impact of conical entrances

Method – The impact of conical entrances on the hydrodynamic permeability was first explored using finite element calculations. A pore made of a central cylinder with radius a and length L, connected to two conical vestibules, with length L_c and opening angle α was considered, see figure 2.10. In a real aquaporin, the fluid transport inside the central part belongs

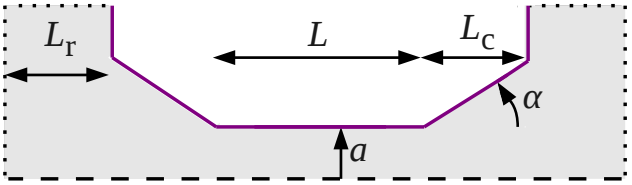

FIGURE 2.10: Hourglass geometry used for finite element calculations.Two reservoirs of size L_r are separated by a membrane pierced by a channel of central radius a and total length $L + 2L_c$, with L the length of the cylindrical part and L_c the length of cones. Cones have got an angle α. The black dashed line corresponds to an axisymmetric boundary condition. The full line represents the liquid/solid interface. The pressure was imposed on the dotted lines.

to the single-file regime and the physics at play here cannot be captured by a continuum description. However, we are not interested here in the specific selectivity of the AQP – which would indeed require a detailed atomic modeling [16, 75, 93, 94]. In order to isolate the entrance contribution, we consider a simplified view in which all dissipation in the AQP central channel is neglected. This is done by assuming a *perfect-slip* boundary condition on the pore surface, so that surface friction is vanishing in this central part. The hydrodynamic boundary condition in the conical regions have also to be prescribed. As shown to be relevant for nano-scale flows [15], we assumed a partial slip BC on the cones' walls, characterized by a slip length b. Interestingly, the molecular structure of the AQP in contact with water is mostly hydrophobic [95–97] (with hydrophilic patches to ensure that water penetrates through the pore), and in line with recent work on hydrodynamic slippage [2, 15], a slip length in the range of tens of nanometers may typically be expected. This value is large as compared to the other typical length scales of the nanopore, $b \gg a$. Consequently, we will start our discussion by assuming perfect slip BC ($b = \infty$), and then relax this condition in a second step.

Results – Our main result is illustrated in figure 2.11, which shows the hydrodynamic permeability K of the a hourglass channel as a function of the opening angle α for various cone's length L_c. The permeability

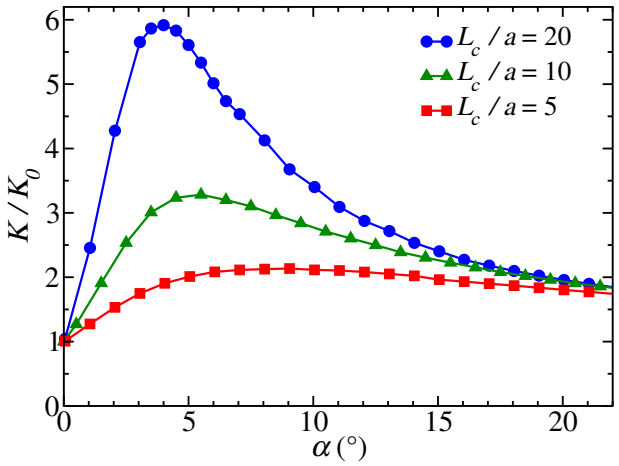

FIGURE 2.11: Hydrodynamic permeability $K = Q/\Delta p$ of the hourglass nanochannel as a function of the opening angle α, obtained from finite element calculations. K is normalized by $K_0 = K(\alpha = 0)$. Perfect slip ($b = \infty$) is assumed on the cones inner walls. Each curve corresponds to a cone length L_c.

$K = Q/\Delta p$ provides the flow rate Q for a given pressure drop Δp. As highlighted in this figure, for any cone length L_c, the permeability is a *non-monotonic* function of the opening angle of the pore: starting from the cylinder geometry ($\alpha = 0$), the permeability starts by increasing very quickly with α, before decreasing slowly for larger angles. There is accordingly an optimal angle α_{opt} which maximizes the channel permeability, i.e. yields a maximal flow rate under a given pressure forcing. Compared to the cylindrical case ($\alpha = 0$), the optimal geometry ($\alpha = \alpha_{\text{opt}}$) yields a very significant increase in permeability, especially for long cones. At $L_c/a = 20$ for instance, the optimal permeability is 6 times larger than the one of a cylinder. Although it increases for shorter cones, the optimal angle remains small, below 10° for $L_c/a > 5$. Surprisingly, a tiny departure from the straight cylinder makes for a large effect on entrance dissipation. This is an unexpected result and in order to gain insight into its origins, we now develop a simplified model to rationalize viscous dissipation in the hourglass channel.

2.3.2 An analytical model for the hourglass nanopore

The present goal is to obtain an analytical expression that describes viscous dissipation in hourglass channel. We assume in a first step a negligible friction on the cone's surface (perfect slip). In this situation, the dissipation is expected to occur mostly within the two transition regions: from the reservoir to the cone (first entrance), and from the cone to the cylinder (second entrance). This is confirmed by the numerical results, as highlighted in figure 2.12, where we have plotted the local viscous dissipation rate $D = 2\eta \mathbf{\Delta} : \mathbf{\Delta}$, with $\mathbf{\Delta} = \left[\nabla \mathbf{v} + \nabla \mathbf{v}^T\right]/2$ the strain rate tensor. The spatial

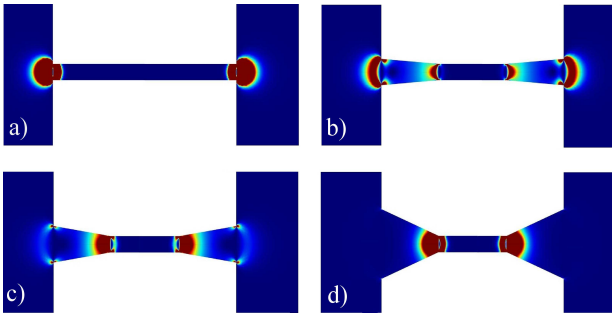

FIGURE 2.12: Local viscous dissipation rate D (see text) inside the nanochannel for different values of the angle α. The color scale, from blue to red, indicates increasing values of local viscous dissipation. Perfect slip boundary condition is imposed on the cone walls. From a) to d), $\alpha = 0, 5, 10$ and $25°$.

extent of both regions is given by the local radius, with a prefactor close to unity. This figure shows that increasing the opening angle shifts the dissipation from the first entrance to the second. This is to be expected if one realizes that the streamlines have basically to follow the surface of the pore, and that the second angle between the cone and the cylinder increases as the first angle between the wall and the cone decreases (the sum of the two angles being constant due to geometry).

This picture suggests to describe the total hydrodynamic resistance of the pore, $R = K^{-1} = \Delta p/Q$ (the inverse permeability), as the sum of the various contributions (channel entrance, cone region, and cylinder entrance [4]) in series, as for a resistive circuit:

$$R = R^{\text{ent}} + R^{\text{cone}} + R^{\text{ent,cyl}}. \tag{2.8}$$

[4]Note that the three resistances do not identify with dissipation inside the volume of reservoir, cone and cylinder respectively. For example, the entrance resistance includes dissipation taking place both in the reservoir and in the cone.

For such a decomposition to hold, both the cylinder radius a and the entrance radius $a' = a + L_c \tan\alpha$ should remain small compared to L_c, which is valid for large L_c/a ratio and small opening angle α.

In a cone of infinite extent with arbitrary opening angle and perfect slip at the wall, the Stokes flow is purely radial with a velocity that decreases as $1/r^2$, where r is the distance from the apex. One may then verify that the pressure drop, evaluated from $\nabla p = \eta \Delta \mathbf{v}$, vanishes in this situation. Accordingly, for the case $b = \infty$ that we consider so far, R^{cone} is thus negligible, in agreement with numerical results, see figure 2.12.

Now, to proceed further and estimate the remaining contributions in equation (2.8), we need to estimate entrance hydrodynamic resistances for two configurations: (i) a conical aperture with a finite angle and perfect slip; (ii) a cone-to-cylinder entrance. These are generalized Sampson geometries, which we consider now.

Conical aperture with a finite angle – The hydrodynamic resistance of the connection between the reservoir and the cone is written

$$R^{\text{ent}} = \frac{C_\infty \eta}{a'^3}, \quad a' = a + L_c \tan\alpha, \tag{2.9}$$

with $C_\infty = 3.75$ and a' the largest radius of the channel. In this expression, a possible impact of the angle α on the C_∞ value is neglected, which is expected to be valid for small angle α.

Cone-to-cylinder entrance – Finally, an expression of the last term, $R^{\text{ent,cyl}}$, which concerns the connection between the cone and the central part of the channel was needed. $R^{\text{ent,cyl}}$ is expected to writes $R^{\text{ent,cyl}} = f(\alpha)\, C_\infty \eta/a^3$, with $f(\alpha)$ a function that ensures that if $\alpha = \pi/2$, $R^{\text{ent,cyl}} = C_\infty \eta/a^3$, and if $\alpha = 0$, $R^{\text{ent,cyl}} = 0$. Numerical calculations indicate that $f(\alpha) \approx \sin\alpha$. In order to extract the contribution of the cone-cylinder junction to the total resistance of the channel, we performed the following numerical calculations. Reservoir parts are removed to eliminate the outer entrance contribution R^{ent}, leaving only a system composed of a central channel and two truncated cones (figure 2.13). We imposed perfect slip BC along both the cone and cylinder's walls, and the incoming flow fields is imposed using the far-field exact expression for frictionless cones. We varied the angle α and observed that the hydrodynamic resistance of such a junction

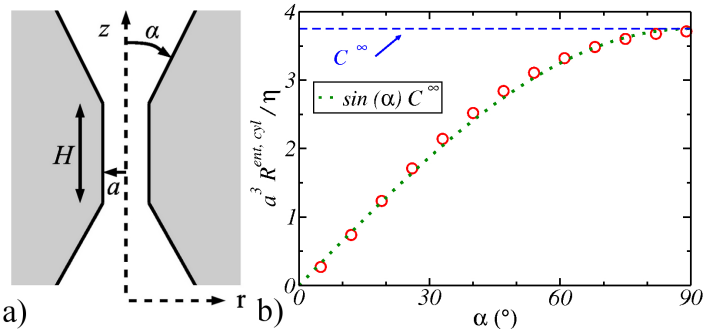

FIGURE 2.13: a) Schematic of the system used to compute the cone-to-cylinder hydrodynamic resistance. b) Cone-to-cylinder resistance $R^{\mathrm{ent,cyl}}$ versus cone angle α: finite element calculations (red circles) and analytical approximation by a sine function (dotted line).

is to a good approximation proportional to the sine of the angle of the cone α (figure 2.13). This can be rationalized on the basis of the following "back-of-the-envelope" argument. Far from the junction, streamlines are parallel in the cylinder and radially divergent in the cone. The dissipation occurs only in the vicinity of the junction, where the streamlines change direction by an angle α, so that $\nabla v \sim v_0 \sin\alpha/a$. The pressure drop Δp is then given roughly as $\Delta p \sim \eta \nabla v \approx \eta v_0 \sin\alpha/a$. Altogether, the hydrodynamic resistance at a cone-to-cylinder transition can be well approximated by

$$R^{\mathrm{ent,cyl}} = C_\infty \sin\alpha \, \frac{\eta}{a^3}, \tag{2.10}$$

with again $C_\infty = 3.75$.

Comparison between model an numerical calculations – Collecting equations (2.8), (2.9) and (2.10), and remembering that $R^{\mathrm{cone}} \approx 0$, yields the total resistance of the hourglass channel in our simplified model:

$$R = \frac{C_\infty \eta}{a^3} \left[\left(1 + \frac{L_c}{a} \tan\alpha \right)^{-3} + \sin\alpha \right]. \tag{2.11}$$

This relation exhibits a non-monotonous behaviour with the angle α, as shown in figure 2.14: the first term in the right-hand-side decreases rapidly with α, while the second term steadily increases. Physically, these two terms account for dissipation at the first and second entrance respectively, and their variations confirm the qualitative picture illustrated in figure 2.12. A minimum for the resistance – thus a maximum for the permeability $K = R^{-1}$ – is then found. In particular, for long cones and small angles,

$R \sim (\alpha L_c/a)^{-3} + \alpha$, and the optimal angle decreases with the cone length as $\alpha_{\rm opt} \sim (L_c/a)^{-3/4}$. More quantitatively, figure 2.14 compares finite element calculations and the predictions of our simplified model. While a quantitative agreement is not expected in view of the simplifying assumptions underlying our model, the latter is found to capture the optimization phenomenon. In particular, the variation of the optimal angle $\alpha_{\rm opt}$ versus length L_c/a is well reproduced, see inset of figure 2.14.

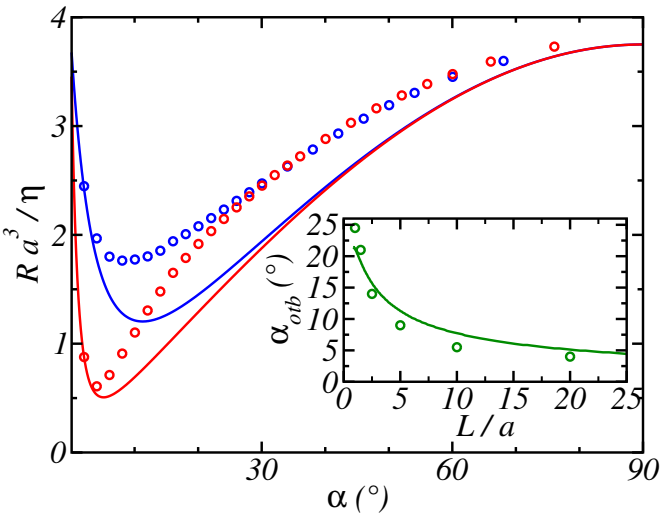

FIGURE 2.14: Pore resistance R versus cone angle α for perfect slip in the cones: comparison between finite element calculations (circles) and equation (2.11) (lines). Results are presented for two pore lengths: $L_c/a = 20$ (red) and $L_c/a = 5$ (blue). Inset: optimal angle α_{opt}, for which the resistance is minimized, as a function of cone length.

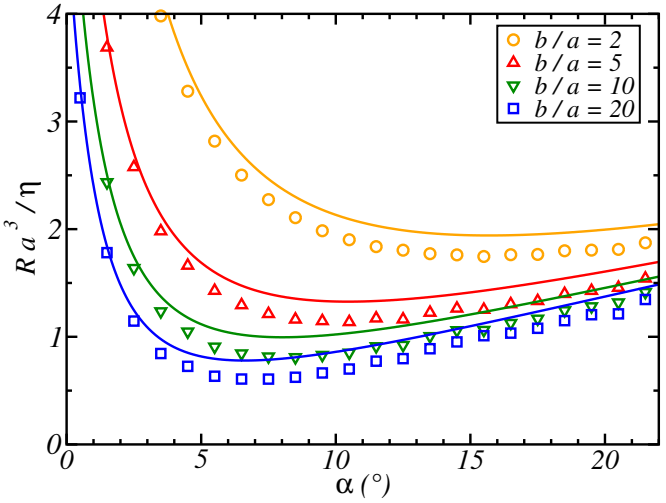

FIGURE 2.15: Pore resistance R versus opening angle α, for various slip lengths b in the conical regions: comparison between finite element calculations (symbols) and analytical expression (lines), see text for detail. The cone length is fixed to $L_c/a = 20$.

Finite slip on cone's wall – Up to now, we assumed a perfect slip BC at the cones' surfaces, corresponding to the limit of large slip lengths compared to transverse dimensions $b/a \to \infty$. We now relax this assumption and consider finite b/a. Figure 2.15 reports the results of numerical calculations for the hydrodynamic resistance versus opening angle, for various slip lengths b at the cone surface and a fixed cone length, $L_c = 20\ a$. As shown in this figure, an optimal angle minimizing the hydrodynamic resistance is still found for finite slip, and its value increases with decreasing slip length, see also figure 2.17.

Again a simplified model can be built. While we do not expect entrance effects to be radically modified, a supplementary dissipation will now occur due to finite slippage at the cone surface. This contribution, R^{cone} in equation (2.8), can be calculated within lubrication theory, valid for small angles α, as

$$R^{\text{cone}} = 2\int_0^{L_c} dz\, \frac{8\eta}{\pi a(z)^4}\left(1+\frac{4b}{a(z)}\right)^{-1}, \tag{2.12}$$

with $a(z) = a + z\tan\alpha$ the local radius of the cone. Accordingly, an analytical expression for R^{cone} can be obtained, but its cumbersome expression is not particularly illuminating and we do not report it here. Gathering all contributions in equation (2.8) leads to an analytical expression for the hydrodynamic resistance of the hourglass pore with finite slip length b on the cones. This expression is compared to the numerical calculations in figures 2.15 and 2.17. A good agreement is found and the approximate expression is able to capture both the dependency of R^{cone} with α and b, as well as the order of magnitude of the optimal angle and its variation with b and L_c/a. Altogether, our results show that the hourglass geometry, associated with small surface friction, does optimize the permeability by reducing considerably the magnitude of entrance effects. A small opening angle in the range $5 - 20°$, depending on the precise geometry and boundary conditions, can increase the permeability by a large factor, reaching hundreds of percent for typical parameters.

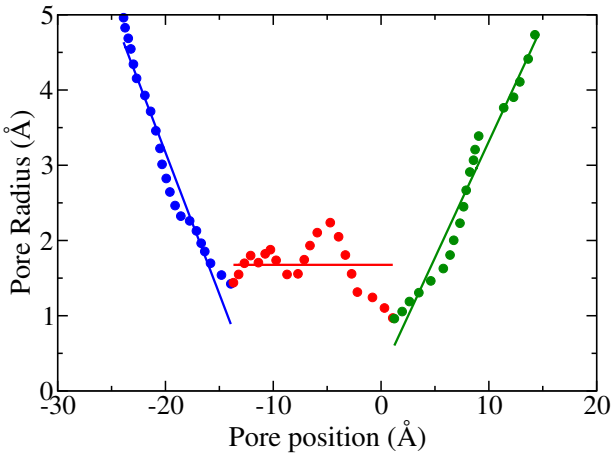

FIGURE 2.16: Profile of an aquaporin (hAQP4 [98], circles) and linear curve fitting (solid lines).

2.3.3 Comparing our model with actual aquaporins

To conclude, we discuss the relevance of these effects for the shape and the hydrodynamic permeability of aquaporins. As explained in the introduction, AQPs have hourglass shapes resembling the model geometry considered here. Furthermore, due to their mostly hydrophobic inner surface, a small friction, and large slip length, is expected at the cone walls. Overall, they exhibit the main ingredients associated with permeability optimization discussed above. In order to push further the comparison, we have extracted some generic shape parameters of a large variety of AQPs. We used molecular structures obtained from high-precision X-ray crystallography – which are available for several aquaporins – and obtained the radius profile of the channel, as estimated by the HOLE program [76]. We have chosen to divide the aquaporin in three parts; two conical entrances and one central part (see figure 2.16). Each part of the aquaporin was linearly fitted to extract the relevant parameters. The central part of the aquaporin gives us the value of the central radius a. From conical entrances, we extracted both the length L and the angle α. Due to the asymmetry of the aquaporin, we obtained two values of cone length and angle for each aquaporin. The results for the opening angle α of the AQPs conical section are displayed in figure 2.17. Two conclusions can be drawn from this figure: (i) the opening angle keeps rather low values, within the range $10 - 25°$; (ii) the optimal angle decreases as the cone gets longer. It is therefore striking that the adopted

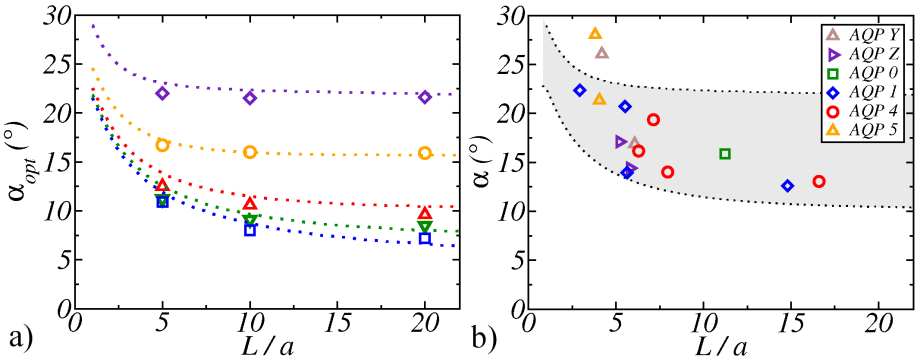

FIGURE 2.17: a) Optimal angle as a function of cone length L for various slip lengths (from top to bottom, $b/a = 1, 2, 5, 10, 20$): finite element results (circles) and model (lines). b) Angle α evaluated in six aquaporins. The gray shaded area corresponds to model predictions for $b/a = 1$ to 5 (as shown in left panel). Data are extracted from Refs. [75, 98–103].

global geometry follows the expectations for the hydrodynamic optimization process discussed above to minimize the entrance permeability.

Obviously, some more detailed features of the AQP geometry can not be discussed within the previous results. In particular, the structure and shape selection of AQPs follows from a number of constraints and requirements, many of them from the molecular level and the subtle balances to achieve selectivity and efficient transport in the inner single-file constriction. For instance, aquaporins channels are not symmetric with respect to the membrane half-plane, as the cone towards the cell exterior is apparently longer and more divergent than the interior cone. Within our model, this could be explained only if the inner and outer cylinders radii were different. While this is often the case, we have considered only the average radius of the central portion, so as to keep a small number of parameters.

2.3.4 Molecular dynamics simulations: validity of continuum results

Continuum hydrodynamic calculations indicate that an hourglass shape leads to a large increase of the overall channel permeability as compared to the cylindrical geometry. The robustness of this result has to be questioned, particularly when the middle part of the considered channel is subjected to the single-file transport, as occurs *e.g.* in aquaporin channels. To do so,

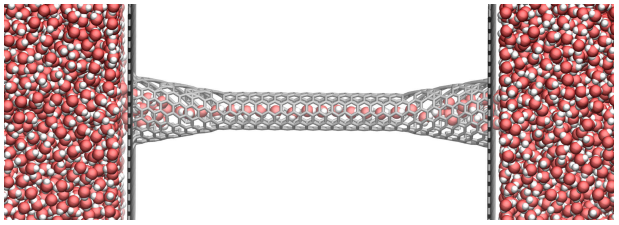

FIGURE 2.18: Snapshots of considered systems. Biconical system [armchair (5,5) tube, $L_c/a_{eff} = 20$ and $a_c = 3.38\,\text{Å}$; see text for definition of the parameters]. Oxygen atoms are colored in red, hydrogen atoms in white, and carbon atoms in gray.

we performed molecular dynamics simulations of water flowing through an hourglass nanochannel.

The considered system was a biconical nanochannel, with a central cylindrical nanotube and two conical entrances, made of graphene-like sheets. Conical entrances were made alike by rolling graphene sheet, thus leaving now a structural defect line. Note that the overall pore's permeability was not affected by this defect line as tested using alternative cone generating methods. Each cone exhibited an angle α, which was varied between 0 and 20 °. Inspired by aquaporins, we used a configuration in which there is single-file flow inside the cylindrical central part: $a_c = 3.38\,\text{Å}$. Moreover, still inspired by aquaporins, we used cones' lengths $L_c \approx 20 \times a_{eff} = 17\,\text{Å}$. We used reservoirs with a size at least ten times the opening radius, a' (with $a' = a_{eff} + L_c \tan\alpha$), which is sufficient to reduce finite size effects down to a negligible level, as estimated by FE calculations. MD results are shown in figure 2.19. We found that the hydrodynamic resistance is again minimized in the hourglass geometry for a cone angle $\alpha \sim 5\,°$, *even if the transport in the center part of channel is single-file*. The minimal resistance is approximately 5 times smaller than the one of a tube with a straight entrance ($\alpha = 0$). Furthermore, as demonstrated in figure 2.19, the continuum hydrodynamic predictions exhibit a good agreement with the results of the MD simulations for the hydrodynamic resistance. In particular, we highlight the critical importance of the position of the hydrodynamic BC by showing two different cases of hydrodynamic radius for the inner part of the pore. We finally compare the results with our theoretical prediction for

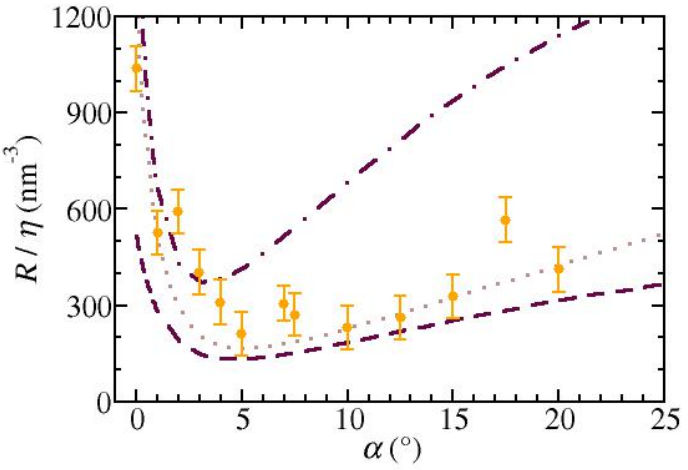

FIGURE 2.19: MD results for the hydrodynamic resistance $R = \Delta P/Q$ of an hourglass channel (normalized by the bulk viscosity η) as a function of the angle of the biconical vestibules. Circles represent MD results. The dotted line represents the prediction of equation (equation (2.13)), with $a_{\text{eff}} = 1\,\text{Å}$. The lines show the FE calculations with two different hydrodynamic radii: $a_{\text{eff}} = 1.08\,\text{Å}$ (dashed line), $a_{\text{eff}} = 0.68\,\text{Å}$ (dashed-dotted line).

the hourglass resistance obtained previously, which can be written as

$$\frac{R}{\eta} = \frac{C}{a_{\text{eff}}^3}\left[\sin\alpha + \left(1 + \frac{L_c}{a_{\text{eff}}}\tan\alpha\right)^{-3}\right]. \tag{2.13}$$

We used the values $L_c/a_{\text{eff}} = 20$, and the parameter $C = 1.15$ obtained from previous FE calculations in the case of an aspect ratio $a_{\text{eff}}/(a_c - a_{\text{eff}}) = 0.33$. The effective radius was fixed to $a_{\text{eff}} = 1\,\text{Å} = a_c - 2.4\,\text{Å}$ in order to obtained the best agreement. With this value, equation (2.13) reproduces quite well the MD results (see figure 2.19). Note that MD results are best fitted with FE calculations for the same value of a_{eff} (not shown for clarity). Therefore, the "hydrodynamic size" of the wall atoms obtained with the biconical geometry, $a_c - a_{\text{eff}} = 2.4\,\text{Å}$, is quite close to the one obtained with a cylindrical pore in previous section ($a_c - a_{\text{eff}} = 2.5\,\text{Å}$). Additionally, one may notice that a number of MD results are slightly outlying the main tendency, beyond the error bar. We conjecture that these may be attributed to discrete geometric effects which may occur preferably for specific values of the cone angles.

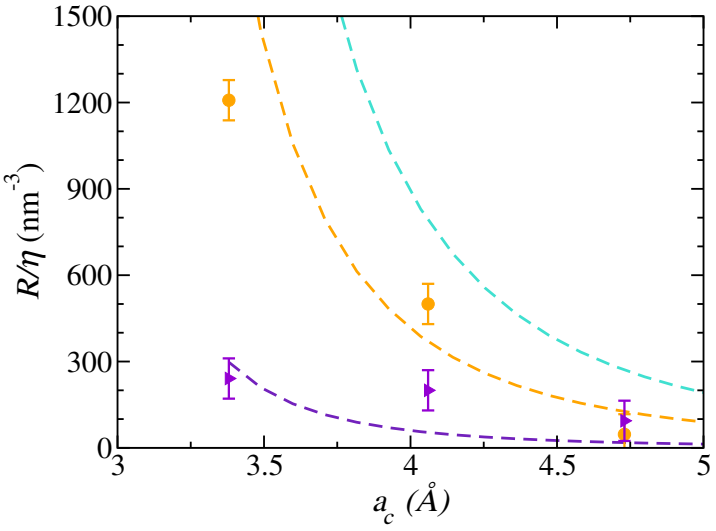

FIGURE 2.20: Comparison of hydrodynamic resistance of hourglass, biconical systems (purple triangles) and graphene sheets pierced with a single hole (orange circles). Dashed lines are continuum hydrodynamics predictions (see text). The cyan dashed line is the Sampson formula for a hole in an infinitely thin membrane.

2.3.5 Biconical nanochannel versus pierced graphene

As a final illustration of the biconical nanochannel efficiency, let us make a comparison with the system that could be seen as the ultimate tools for water filtration: pierced graphene. Indeed, pierced graphene was discussed lately to represent a very efficient geometry for desalination purpose [28, 104, 105], in particular due to its large permeability combined with an excellent rejection ability. The large permeability of pierced graphene is due to the molecular thickness of the graphene sheet: in this case, the transport is fully controlled by the entrance effect, and belongs to the Sampson's class of problem. It is therefore interesting to compare the performance of this geometry to the hourglass one which was precisely found to reduce entrance effects. To this end we have performed MD simulations of transport across nanopores drilled in a graphene sheet with various pore sizes, and measured the corresponding hydrodynamic resistance. This is compared to the hydrodynamic resistance of an hourglass shape nanopore with an inner channel having the same radius. We used hourglass systems with three different inner pore radii, respectively $a_c = 3.38$, 4.06 and 4.73 Å. We kept the cone lengths ratio L_c/a_c equal to 20 and the angle α equal to 5 °. The radius of the hole a_c in the graphene sheet was equal to 3.38, 4.06 and 4.73 Å. Results are shown in figure 2.20. As can be seen in this figure, the hourglass

nanopore has a hydrodynamic resistance which is systematically smaller than the graphene for the same inner pore diameter. As a comparison, we plotted the result of the classic Sampson formula, equation (2.5), with a hydrodynamic radius equal to $a_{\text{eff}} = a_c - 2.5\,\text{Å}$ (see above) and a coefficient $C = 3$. As seen in figure 2.20, this overestimates the MD results for the hydrodynamic resistance of porous graphene. In an attempt to improve this result, we took into account at the continuum level the finite thickness of the graphene membrane, as compared to the pore radius. This leads to a reduction of the coefficient C in the Sampson formula. The value of C depends on the ratio $a_{\text{eff}}/(a_{\text{c}} - a_{\text{eff}})$, and in the present conditions it varies between 1.15 and 1.6 for the considered radii. We took $C \simeq 1.3$ in equation (2.5) as a compromise, showing a good agreement with the MD results. For the hourglass geometry, we compare the MD results with the prediction of equation (2.13), using the same coefficient $C = 1.3$. This shows again a good agreement with the MD results. Altogether these results show that tuning the geometry of nanopores allow to strongly optimize water transport through membranes. The hourglass shape outperforms both nanotubes and pierced, molecular thick, graphene.

2.4 Conclusion

The aim of this work was to determine the effect of the geometry and the hydrodynamic boundary condition on hydrodynamic entrance effects in a nanochannel. Inspired by carbon nanotubes and aquaporins, we explored transport through both chamfered cylindrical and hourglass shaped nanopores. Using finite element calculations and molecular dynamics simulations, we have shown that compared with a plain cylindrical pipe, a biconical channel of optimal angle can provide a spectacular increase in hydrodynamic permeability. This hourglass shape proves to substantially enhance the water transportation efficiency down to the single-file regime, with an optimum for shallow opening angles $\sim 5°$, all in line with continuum hydrodynamics predictions.

A simplified model based on entrance effects and lubrication approximation rationalizes the observed behaviour. Compared with the promising system made of a circular nanopore drilled in graphene sheets, or straight carbon

nanotubes, the hourglass shape pore appears far more efficient, illustrating the dominant role of entrance dissipation in all these systems. We also investigated the fate of hydrodynamic entrance effects in the limit of molecular scale nanopores, down to the single-file regime. Strikingly, we found an extremely good agreement between MD simulations and continuum hydrodynamics predictions of entrance resistance obtained from FE calculations. For straight nanopores, comparison between MD and FE approaches incorporate the position of the solid-liquid interface as an important parameter, which therefore could be located using such an approach.

Although speculative, this could indicate that the hourglass geometry of AQPs results from a shape optimization, to reduce end effects and maximize water permeability. We found that biconical entrances can increase the water permeability of a nanopore, leading to better performance than simple cylindrical pore or graphene sheet. Overall, this stresses the necessity for finely tune the geometry of nanopores for strongly optimizing water transport across membranes, a task for which simple continuum approaches can be astonishingly reliable.

Chapter 3

Subcontinuum capillary filling

Contents

This chapter is based on the following publication:

- Simon Gravelle et al. Anomalous capillary filling and wettability reversal in nanochannels. *Physical Review E* 2016 [106]

Abstract and main results – This chapter focuses on the capillary filling of subnanometric carbon nanopores by a fluid. While capillary filling in macroscopic channels has been thoroughly explored, it is worthwhile to reconsider it for subnanometric channels. In subnanometric channels, the importance of the molecular aspect of fluids is enhanced, the role of the surface becomes more important, and a deviation from the classical no-slip boundary condition may occurs. These phenomena are expected to lead to a failure of the continuum predictions, and possibly an appareance of new interesting regimes.

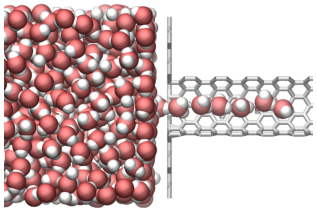

A

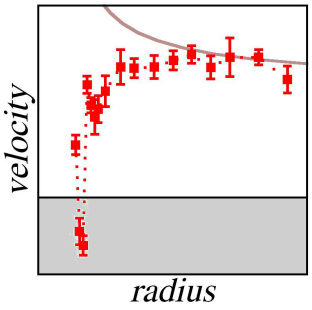

B

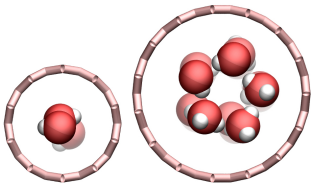

C

To explore capillary filling inside subnanometric CNTs, we used Molecular Dynamics (MD) simulations (see figure A). Results show that, for tube radii below one nanometer, the filling velocity is a non-monotonic function of the tube radius, as shown in figure B which shows the capillary filling velocity of water as a function of the CNT radius. This is in contradiction with continuum assumptions (brown line). Beyond this non-monotonic dependancy, an even more striking phenomenon is the possibility to switch pore from hydrophilic to hydrophobic behaviour just on specific radius values (gray area on figure B).

To reconcile continuum predictions and MD results, one has to take into account the excess pressure which is due to the structuring of the fluid, represented in figure C. The so-called disjonction pressure, whose sign depends on the pore dimensions, has been found to strongly impacts the dynamics for the smallest CNT radii. MD measurements in slit nanochannels, for which the expression of the disjoining pressure is known, confirm the link between the observed non-linearities and the disjoining pressure.

3.1 Introduction

3.1.1 State of the art

Scientists have been interested in capillarity-induced phenomena for at least 500 years. The first studied configuration of capillary filling was capillary rise, which has been proposed as the phenomenon at the origin of mountain streams by Leonardo da Vinci (1452-1519). He suggested that water rises thanks to capillarity through a network of cracks. Later, Geovanni Borelli (1620-1675), Francis Hauksbee (1666-1713) and James Jurin (1684-1750) demonstrated independently the so-called Jurin's law which states that the height of the raised liquid h is inversely proportional to the size of the pore r: $h \propto 1/r$. One may also notice that capillary rise has been invoked as the phenomenon at the origin of the circulation in plants by Geminiano Montanari (1633-1687), who compared the rise of a liquid in a tube to that of the sap in a plant [49].

Later, in the early 19th century, Young and Laplace have developed the concept of capillarity, which is traditionally defined as the tendency of wetting liquids to be drawn into the confined space of a narrow tube [107, 108]. But capillarity is also associated with the phenomenon of enhanced pressure inside a droplet due to the constrictive surface tension force, or the collapse of smaller drops in favor of bigger ones inside an emulsion. So a wider definition of the concept of capillarity would involve all situations in which two phases are separated by a curved interface [109, 110]. Behind this concept of capillarity stands a central relation, the Young–Laplace equation, which describes the capillary pressure difference sustained across the interface (assumed to be infinitely thin) between two static fluids, such as a liquid and a gas, due to surface tension. It relates the pressure difference Δp between the two fluids to the shape of the surface and can be written as

$$\Delta p = \gamma \left(\frac{1}{R_1} + \frac{1}{R_2} \right) \tag{3.1}$$

where γ is the surface tension and $R_{1,2}$ the principal radii of curvature. Equation (3.1) indicates that there is a jump of pressure when a curved surface is crossed.

Today it is known that capillarity is involved in a large number of geophysical and biological effects and is used in numerous industrial applications. For example, soil contains an infinity of cracks in which excess water runs to the surface when it is hot and dry and allows trees to survive. Capillary rise has also been reported as a drinking strategy of insects, birds and bats [111]. Moreover, capillarity is used by some animals (flies, bugs, grasshoppers, tree frogs and beetles) to stay and walk on steep or downward-facing surfaces [112]. On the other hand, capillarity is present in numerous industrial disciplines such as pharmacology, cosmetic, glass industry, textile, painting or insecticides. Some other applications that deal with capillarity are electrospray or nano-fountain pen writing.

This non-exhaustive overview shows that capillarity is present in a large number of everyday phenomena, and consequently, is a widely studied effect. Nevertheless, some of the recently arisen aspects or complications occurring at the nanoscale remained largely unexplored at the beginning of this PhD work. Understanding capillarity at this scale is important to fully describe the porous medium imbibition dynamics. The concerned media are for example organic inclusions (kerogen) with sub-nanometer pore space, or nanoporous systems used for example in water desalination such as zeolites. The present study focuses on some aspects of capillary filling at the nanoscale, and its objectives (expectations) are described in the following section. Then some important notions are detailed as well as the theoretical equations describing capillary filling of tubes.

3.1.2 Expectations/motivations

As mentioned above, capillary filling is an old and widely studied problem. However, it has to be revisited since nanometric pores introduce two new features [43, 113]. The first one is a breakdown of continuum hydrodynamics expected for systems with characteristic dimensions below one nanometer [2]. The second one is an important impact of the hydrodynamic boundary condition on the filling dynamics, expected due to the increasing role of surfaces. For example, deviations from the classical hypothesis of a no-slip boundary condition (BC) at the liquid/solid interface have been predicted theoretically and observed experimentally [15]. The impact of liquid/solid

slip on capillary dynamics has been highlighted by Joly [72]. He found that, in the short-time limit, the filling velocity of water in a carbon nanotube (CNT) is limited by viscous dissipation at the tube entrance. We will push this study further by considering the capillary filling inside CNTs with subnanometric diameters. The important point is that effective radii of subnanometric tubes are close to the fluid molecules' diameter, and strong deviations from the continuum predictions are expected. For example, the structuring of the fluid is not taken into account by classical hydrodynamics, and an important impact on the capillary dynamics can be anticipated.

In what follows, the equations of motion for several classical regimes are described. Note that the basic notions concerning capillarity are described in chapter 1.

3.1.3 From Lucas-Washburn law to the specific case of CNTs

Capillary filling is a consequence of the existence of surface tension and wetting, that are described in chapter 1. The equations that govern this process inside pipes are described below, and some transport regimes are highlighted. We start by a description of the classical case that considers friction along the tubes' wall and negligible entrance dissipation. Then, we extend this description to the specific case of CNTs, for which most of the dissipation comes from the entrances, due to the large slip length in comparison to the tube radius, as discussed in chapter 2.

The Lucas-Washburn law

Let us consider a cylindrical pore of radius a and length H in contact with a reservoir of liquid (density ρ, viscosity η), see figure 3.1. The liquid/vapor surface tension is written γ, and the contact angle of the liquid on the solid surface is noted θ. We call L the length of the liquid column inside the tube. The velocity of the meniscus is related to L through: $v_c = \mathrm{d}L/\mathrm{d}t$. The equation of motion for the liquid inside the pore can be written

$$\frac{\mathrm{d}(Mv_c)}{\mathrm{d}t} = F_c + F_v, \tag{3.2}$$

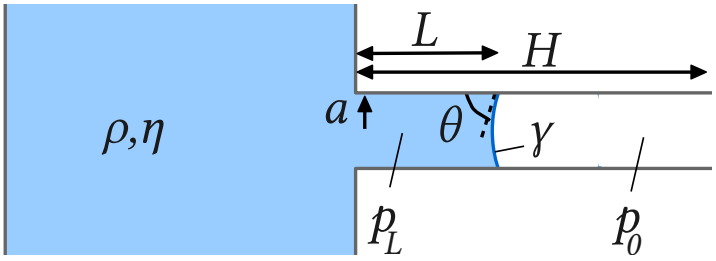

FIGURE 3.1: Schematic of the system.

where $M = \rho\pi a^2 L$ is the mass of liquid inside the pore, F_c the capillary force and F_v the friction force. The capillary force can be written as

$$F_c = 2\pi a \Delta\gamma, \tag{3.3}$$

where $\Delta\gamma = \gamma_{\mathrm{SG}} - \gamma_{\mathrm{SL}} = \gamma\cos\theta$ is the capillary force per unit length at the contact line. Note that this force results from the integration of the pressure force on the meniscus. One can show that it is equivalent to a force per unit length acting at the contact line. γ_{SG} and γ_{SL} are respectively the solid-gas and the solid-liquid surface tensions. The friction force is given by the Poiseuille law, modified to take into account liquid/solid slip:

$$F_v = -\frac{8\pi\eta L v_c}{1 + 4b/a}, \tag{3.4}$$

which leads to the following equation of motion

$$\frac{\mathrm{d}(\rho\pi a^2 L v_c)}{\mathrm{d}t} = 2\pi a\Delta\gamma - \frac{8\pi\eta L v_c}{1 + 4b/a}. \tag{3.5}$$

The solution of this nonlinear equation can be written as [72, 114]:

$$L(t) = L_c\left(\frac{t}{\tau_c} + \frac{e^{-2t/\tau_c} - 1}{2}\right)^{1/2}, \tag{3.6}$$

with

$$\tau_c = \frac{\rho a^2}{4\eta}\left(1 + \frac{4b}{a}\right), \tag{3.7}$$

and

$$L_c = \frac{(2\gamma\rho a^3)^{1/2}}{4\eta}\left(1 + \frac{4b}{a}\right). \tag{3.8}$$

In the long time limit, where the liquid inertia can be neglected compared to the viscous friction inside the tube, the equation (3.6) simplifies to the

Lucas-Washburn law:

$$L^2(t) = \frac{\Delta\gamma a}{2\eta}\left(1 + \frac{4b}{a}\right)t. \tag{3.9}$$

In this regime $L \propto \sqrt{t}$, so $v_c \propto \mathrm{d}L/\mathrm{d}t \propto 1/\sqrt{t}$: the filling slows down with time, which is logical since there is friction between the increasingly long water column and the tube. In the short time limit, the viscous friction can be neglected in comparison to the inertia, and one gets an equation that does not depend on the liquid friction nor the slip length b :

$$L(t) = \left(\frac{2\Delta\gamma}{\rho a}\right)^{1/2} t. \tag{3.10}$$

Note that a pre-inertial regime appears for $L < a/2$ as highlighted by reference [115], but we will always ignore it here due to the dimension of the considered system (i.e. $a < 3$ nm). The Lucas-Washburn law is a standard equation in capillary filling study, but it is not suitable for describing the dynamics of the present work. Indeed, due to the extremely low friction at the CNT wall, one has to consider the viscous dissipation at the entrance, just like in chapter 2. When the entrance dissipation dominates the overall dissipation, the length of the column does not matter and the filling velocity is constant over the time. The equations of motion of this particular situation are described now.

The special case of subnanometric CNTs

Viscous dissipation – As seen in chapter 2, when studying transport inside a subnanometric nanochannel, one has to take into account a viscous entrance dissipation. The pressure drop at the entrance of the tube Δp is linked to the total flow Q as

$$\frac{\Delta p}{Q} = R_{\text{out}} = \frac{1}{2} \times \frac{C\eta}{a^3}, \tag{3.11}$$

where the factor $1/2$ comes from the fact that there is only one entrance in the situation of capillary filling, and $C \sim 3$. As seen in chapter 2, the competition between entrance and inner dissipations leads to the appearance of a critical pore length $L_0 = \pi C b/2$ which separates a regime dominated

by entrance dissipation and a regime dominated by inner dissipation. Since b is in the range of several tens of nanometers in our case, and since the considered tube length L is equal to 10 nm, we made the assumption that CNTs filled by water are in the regime $L \ll L_0$.

Neglecting the inertia – Hereafter, inertial effects will always be neglected. An argument based on the dissipated power confirms the limited importance of inertial effects, in comparison to viscous ones. Indeed, since most of the dissipation is expected to come from entrances, the power dissipated by viscosity $\mathcal{P}_v$ can be roughly estimated as :

$$\mathcal{P}_v = \frac{\eta}{2} \int_V (\partial_i v_j + \partial_j v_i)^2 \mathrm{d}V \sim \eta a v^2, \tag{3.12}$$

where V is the volume of the system and where we used that the only length scale is the tube radius a. On the other hand, the kinetic power of the liquid can be written as

$$\mathcal{P}_k \sim \rho a^2 v^3. \tag{3.13}$$

In the present study, we consider nanotubes with radii below 3 nm, and typical fluid velocities are around 10 m/s. One finds $P_k/P_v \sim 0.03$ (using $a = 3\,\mathrm{nm}$, $v = 10\,\mathrm{m/s}$, $\rho = 1000\,\mathrm{kg/m^3}$ and $\eta = 1\,\mathrm{mPa.s}$), which indicates that inertial effects can be neglected in comparison to viscous ones.

Capillary filling velocity – After neglecting both inner viscous dissipation and inertial effects, two contributions to the equation of motion are remaining. The first one is the capillary force $F_c = 2\pi a \Delta\gamma$, which leads to the following pressure jump through the meniscus:

$$\Delta p^{\mathrm{men}} = \frac{2\Delta\gamma}{a}. \tag{3.14}$$

The second one is the viscous entrance dissipation, which leads to the following pressure jump at the entrance of the nanochannel:

$$\Delta p^{\mathrm{ent}} = \frac{Q}{2} \times \frac{C\eta}{a^3}. \tag{3.15}$$

Using that $Q = \pi a^2 v$ and writing $\Delta p^{\mathrm{men}} = \Delta p^{ent}$, one finds the expression (3.16) for the capillary velocity v_c:

$$v_c = \frac{4\Delta\gamma}{\pi C \eta}. \tag{3.16}$$

Hence in this particular regime, the filling velocity is the result of a competition between surface tension and entrance dissipation, and is constant along time.

3.1.4 Outline of the present work

Classical expressions of capillary filling dynamics have been presented here. The goal of the present work is to check the validity of these expressions for subnanometric nanopores. In a first part, molecular dynamics simulations are used to measure capillary filling dynamics inside CNTs of various radii (from 3.9 Å to 24 Å). Both capillary velocity and Laplace pressure are evaluated. Results show strong deviations from continuum predictions, particularly for subnanometric channels. In a second part, in order to model this effect, a theory involving a disjunction pressure originating in the fluid structuring is proposed. To support this model, capillary filling measurements inside slit nanochannels, for which the expression of disjunction pressure is well known, have been performed using molecular dynamics simulations. Results show a good agreement between molecular dynamics simulations and continuum theory corrected by a disjunction pressure term.

3.2 Method and results

3.2.1 Molecular dynamics simulations

The system consists in a water reservoir in contact with an initially empty carbon nanotube (CNT) enclosed between pierced graphene sheets, see figure 3.2. Empty rigth reservoir is not shown here. Water molecules were initially disposed on a simple cubic lattice with equilibrium density. The CNT length was 10 nm, with radii a_c varying between 3.9 Å and 24 Å. Note that a_c refers to the position of the center of carbon atoms. We showed in the previous chapter that the effective radius a seen by water molecules is smaller: $a_c - a \approx 2.5$ Å, see Chapter 2. The axis of the CNT defines the axis z. Periodic boundary conditions were imposed in all directions and

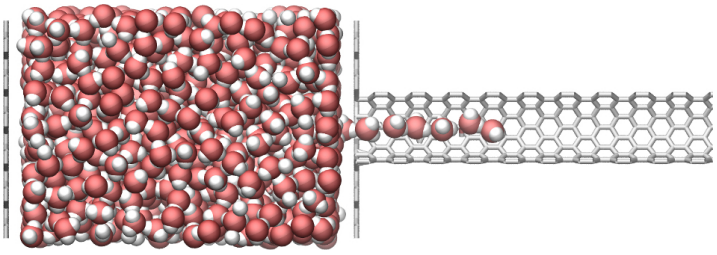

FIGURE 3.2: Snapshot of a system used for the molecular dynamics simulations. The radius of the tube is equal to 3.9 Å. The snapshot has been made using VMD [74].

a third graphene sheet was used as a piston. The role of this piston was first to prevent the evaporation, and to stop the fluid if needed (to measure the capillary pressure in static conditions, see below). Molecular dynamics simulations were performed using LAMMPS [82]. Long-range Coulombic interactions were computed using the particle-particle particle-mesh (PPPM) method. Water molecules were held rigid using the SHAKE algorithm. The equations of motion were solved using the velocity Verlet algorithm with a timestep of 2 fs. The positions of the carbon atoms (wall+CNT) were fixed. Simulations with flexible and fixed walls were shown to give similar results for the statics and friction of confined liquids in previous works [87–89]. Water molecules located at more than 5 Å from the membrane enclosing the tube entrance were kept at a temperature of 300 K using a Berendsen thermostat, which rescales the molecule velocities every timestep [116]. We used the TIP4P/2005 water model [**Abascal2005b**] and used the AMBER96 force field for the carbon-oxygen interactions, i.e. a Lennard-Jones potential with the following parameters: $\epsilon_{CO} = 0.114\,\text{kcal/mol}$ and $\sigma_{CO} = 0.328\,\text{nm}$ [117]. The cut-off value r_c for the Lennard-Jones potential was taken to be equal to 12 Å, which is slightly larger than conventional values that are around $8.5 - 10\,\text{Å}$ [**Abascal2005b**, 117]. Indeed, the filling velocity have been found to be strongly dependent of the value of r_c, converging only for $r_c > 12\,\text{AA}$. Moreover, the box size along the x and y directions is taken sufficiently large to ensure that interactions between images CNTs do not affect the velocity measurements, typically twice the tube diameter [118]. Finally we make sure that the reservoir is bigger than 10 times a_c along z. Finite element calculations indicate that, in that configuration, the error due to finite size effects should be lower than 0.25 % [61].

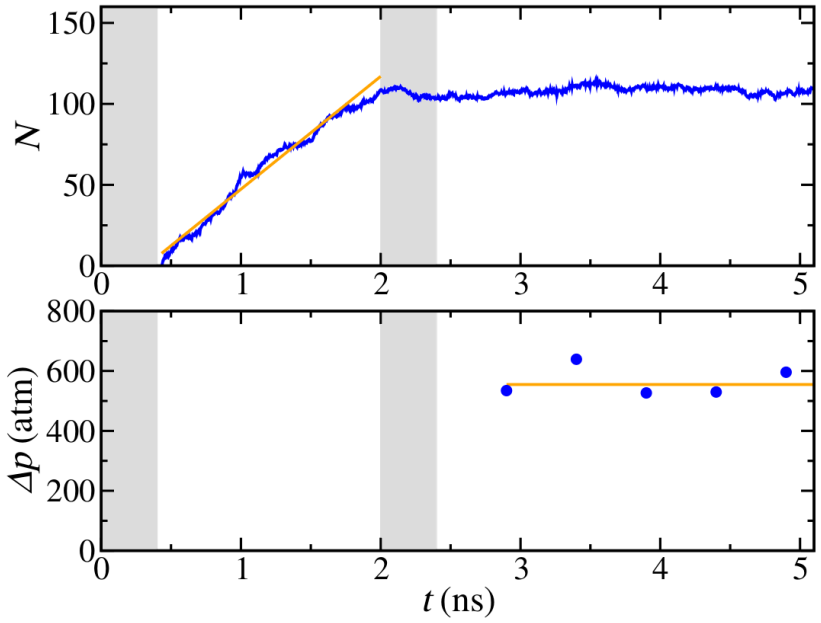

FIGURE 3.3: Up: number of particles inside the tube N as a function of the time. Down: measured Laplace pressure $p_L = \Delta p$. MD results are in blue, linear fits in orange and equilibrium steps are gray areas.

3.2.2 Data acquisition

The protocol of data aquisition has been divided in four stages in order to extract the two quantities of interest which are the filling velocity (dynamic phase) and the Laplace pressure (static phase). Before each phase, equilibrium stages were performed. Let us describe those stages as well as the corresponding measured quantities. First the system was equilibrated during 0.4 ns, with a plug at the tube entrance to prevent water from entering. Then the plug was removed and the evolution of the number of molecule inside the tube N was recorded as a function of time. This constituted the dynamic stage. Note that, for a given tube radius, the filling velocity appeared to be constant during the simulation (not taking into account thermal fluctuations). So the filling velocity v_c can be defined as

$$v_c = \frac{dN}{dt}\frac{1}{\lambda} \tag{3.17}$$

where dN/dt is the temporal derivative of the number of molecules inside the tube N fitted during the dynamic stage and λ is the linear density of fluid inside the tube, measured once the tube is filled. The dynamic stage lasted until the tube was partially filled (typically 1 or 2 ns, depending of the tube radius). Then the piston was frozen, which prevented water molecules

to fill the tube despite the presence of the capillary force. After another equilibrium step of 0.4 ns, the pressure exerted by the fluid on the piston (measured by recording the total force on the piston, divided by its surface) was recorded during 2.5 ns. In the absence of flow, this pressure corresponds to the Laplace pressure. An example for a tube radius $a_c = 5.1$ Å is plotted on figure 3.3. For each case, the simulation was performed 5 times with different initial conditions; the resulting velocity and pressure values were averaged and standard deviation were calculated.

Note that the described acquisition process applies for hydrophilic tube only. For hydrophobic tubes, the water is forced to enter the channel thanks to a pressure applied with the piston (until the tube is half-filled) in a first time. In the second time, the piston is frozen and the pressure is recorded before the piston is freed and the velocity recorded while the water leaves the tube.

3.2.3 Results

The measured filling velocities v_c for various tube radii a_c are shown in figure 3.4. For $a_c < 15$ Å, the filling velocity deviates from the continuum

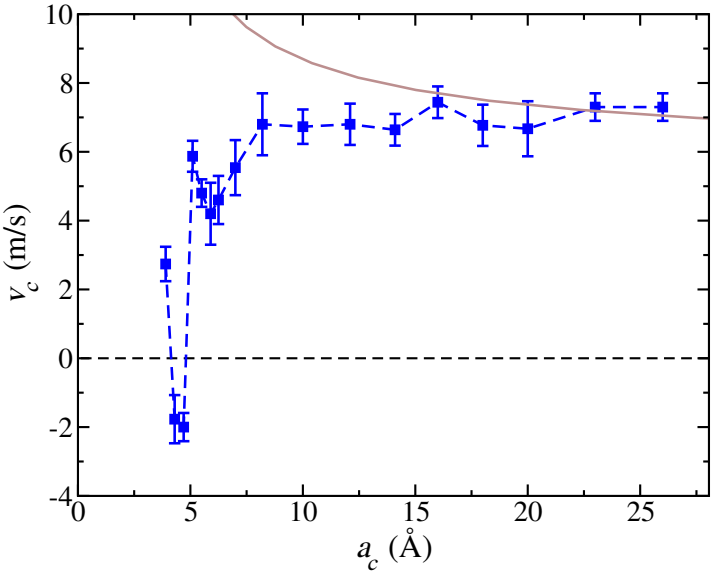

FIGURE 3.4: Filling velocity v_c as a function of the tube radius a_c measured from molecular dynamics simulation (green symbols). The brown line corresponds to formula $v_c = 4\Delta\gamma/\pi\eta C$, with C being estimated from finite element calculations, and $\Delta\gamma$=14 nN/m.

prediction, calculated with macroscopic surface tension and viscosity, $v_c =$

$4\Delta\gamma/\pi C\eta$, which predicts only a continuous variation of v_c with a_c through the Sampson coefficient C. For radii between 5.1 and 15 Å, v_c decreases by a factor up to 2 compared to continuum predictions. Note that the decrease is not monotonous on this range of radii, and that a small increase of v_c is measured for a_c around 5.1 Å. For radii $a_c = 4.3$ and 4.7 Å, v_c is found to be negative, which means that for a tube initially filled with water, the liquid is ejected (reverse capillary flow). For radii $a_c = 3.9$ Å, v_c is positive again.

Hence velocity measurements show deviations from the continuum prediction. Referring to the continuum equation $v_c = 4\Delta\gamma/\pi\eta C$, it appears that those deviations may have several origins. First, the fluid viscosity η may differ from the bulk value inside the pore. Second, the entrance dissipation coefficient C may differ from the finite element prediction. Finally, the capillary force per unit length $\Delta\gamma = \gamma\cos\theta$ may deviate from the continuum prediction, since γ and θ both are macroscopic values. In order to identify the origin of the deviations of the velocity from the continuum prediction, let us perform an independent measurement of the last term, i.e. the capillary force per unit length. Note that the results of the chapter 2, where we performed measurements of the product $C \times \eta$, indicates that entrance effects is not a good candidate to explain the behaviour presented in figure 3.4. To measure $\Delta\gamma$ independently of C and η, static simulations using a fixed piston to block the flow were performed, as described previously. The measured quantity was the Laplace pressure, which is linked to $\Delta\gamma$ as $p_L = 2\Delta\gamma/a$, with a the effective radius of the tube. The measured Laplace pressure p_L is shown on figure 3.5. p_L is found to strongly vary with the tube radius, particularly for a_c below 12 Å. The Laplace pressure is negative for a_c =4.3 and 4.7 Å only, but positive otherwise, in very good qualitative agreement with velocity measurements. Moreover, for large tube radius, a good agreement between pressure measurements and formula $p_L = 2\Delta\gamma/a$ is found for $\Delta\gamma = 12.8$ mN/m, in good agreement with velocity measurements from which a value of $\Delta\gamma = 14$ mN/m has been extracted.

One may wonder whether or not the pressure is the only reason of the difference between molecular dynamics results and continuum predictions. In other words, is there an other phenomena that contribute to the non monotonic behaviour of the velocity? In that purpose, MD results for velocity and pressure normalized respectively by $4\Delta\gamma/\pi\eta C$ and $2\Delta\gamma/a$ are

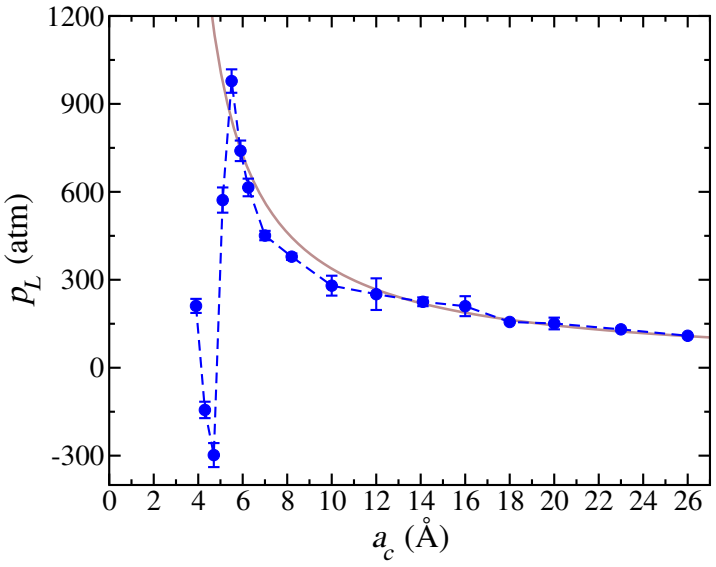

FIGURE 3.5: Laplace pressure p_L estimated from static measurements of the pressure drop Δp. Molecular dynamics simulations: blue dots. Continuum prediction $\Delta p = 2\Delta\gamma/a$ with $\Delta\gamma = 12.8$ mN/m: continuous brown line.

plotted in figure 3.6. One can see a quite good qualitative agreement between

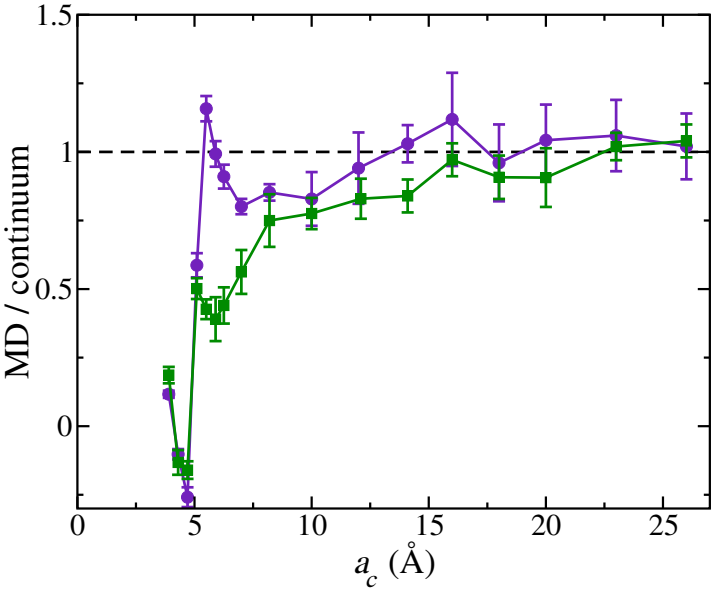

FIGURE 3.6: Ratio between Molecular Dynamics (MD) results and continuum prediction for the velocity (green squares) and for the pressure (violet circles).

normalized pressure and velocity, which indicates that pressure variations are the main cause of velocity gap between molecular dynamics results and continuum predictions. However, while essentially agreeing for the most striking part of the deviations from continuum predictions (non monotonous behaviour and hydrophilicity reversal), some deviations can be seen for tube radii between 5.5 and 7 Å. Hence they might be another phenomenon that

increases the gap between dynamic and static measurements. For example entrance effects, which have been considered as a bad candidate to explain the oscillations of the filling velocity (based on the results of chapter 2) could still be at the origin of the deviations ($\sim$ factor 2) observed in figure 3.6. Indeed, some deviations at small radius in the product $C \times \eta$ may impact the filling velocity (dynamic situation) but not the Laplace pressure (static situation).

In summary, we found that the filling velocity of water inside a CNT differs from continuum predictions, particularly for tube radii below 1.5 nm. We also found that the force per unit length at the origin of capillary filling explains most of the deviations observed in the capillary velocity. To understand the origin of the gap between molecular dynamics results and continuum hydrodynamic, an important question must be addressed: are those results water specific? Or are they general and observable regardless of the liquid? To answer this question, capillary filling of CNTs with a simple liquid were performed.

3.2.4 Are those results water specific?

As a final step, numerical simulations of capillary filling inside CNTs using a liquid metal instead of water were performed. Again, the filling velocity and the Laplace pressure were recorded for various tube radii (from $a_c = 3.5\,\text{Å}$ to $23\,\text{Å}$). Liquid water is known to present anomalous properties, and has the particularity of directional interactions (hydrogen bonds), that impact the relative orientation of neighbouring molecules [119]. Then, one may wonder if our main observations on the subcontinuum capillary filling behaviour of water also apply on simple liquids. "Simple" refers here to the absence of directional interactions between fluid molecules. To answer this question, molecular dynamics simulations of capillary filling of CNT with a liquid metal were performed. The advantage of liquid metals, in comparison with the even simpler Lennard-Jones liquids for example, is their high cohesion which allows the liquid to resist to the high negative pressures at play in (sub)nanometric capillary filling.

Method – Liquid metals are commonly described by the embedded atom method (EAM) [120]. Therefore, we based our model liquid metal on the

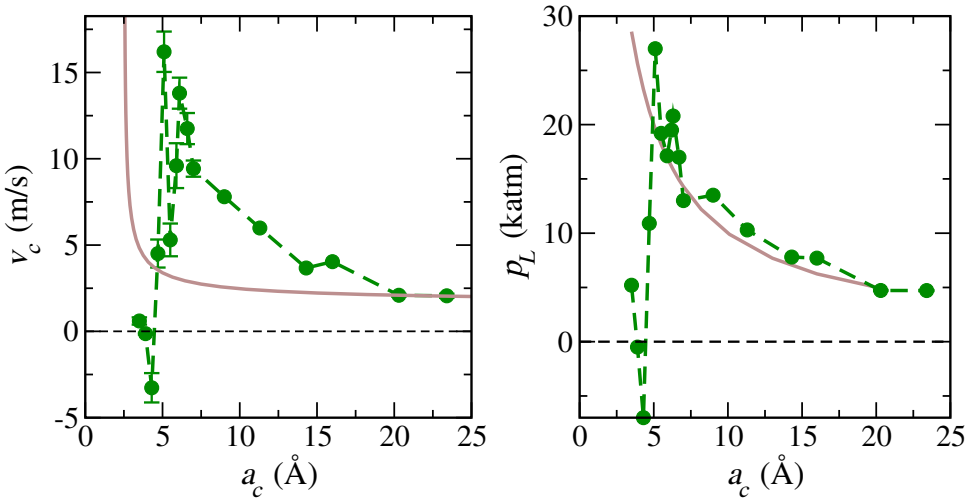

FIGURE 3.7: Left: filling velocity of the model liquid metal v_c measured in a single CNT as a function of the radius a_c. Right: Laplace pressure p_L estimated from static measurements of the pressure drop Δp. Molecular dynamics simulation results are green symbols, the brown line corresponds to continuum prediction (see text).

liquid gold (Au) model developed by Grochola and al [121]. The fluid temperature was 1200 K. The distance space parameter was chosen to be $dr = 0.6410^{-3}$ Å to reproduce water density, which makes the comparison easier. We measured both the liquid metal viscosity and surface tension, and found a viscosity $\eta_m = 30 \pm 4$ mPa.s and a surface tension $\gamma_m = 777 \pm 2$ mN/m. Finally we chose an interaction parameter $\epsilon_{MC} = 0.052$ kcal/mol while keeping $\sigma_{\mathrm{MC}} = \sigma_{OC} = 3.28$ Å and $\epsilon_{MC} = 0.052$ kcal/mol, where M refers to metal, C to carbon and O to oxygen.

Results – The filling velocity v_c and the Laplace pressure p_L were measured for various radii and plotted on figure 3.7, and compared with continuum predictions, respectively $4\Delta\gamma/\pi\eta C$ for the velocity and $2\Delta\gamma/a$ for the pressure. Similarly to what we observed for liquid water, both the filling velocity v_c and Laplace pressure p_L show deviations from continuum prediction for radius below 1 nm. For example, for both liquids, negative velocities have been found for tube with radii $a_c \sim 4.3 - 4.7$ Å, as well as positive velocities for $a_c = 3.9$ Å and $a_c \geq 5.1$ Å. Note that the quantitative behaviour of the filling dynamics in case of metal differs from the case of water. We do not discuss this difference here. Altogether, our results indicate that the hydrophilicity reversal and non monotonous evolution are not water-specific, and are obtained with simple liquids too.

3.3 Discussion

Strong deviations from continuum theory of capillary filling dynamics have been observed in sub-nanometric CNTs. Strikingly, for some specific radii ($a_c = 4.3 - 4.7\,\text{Å}$), reverse capillary filling has been observed in this study. Note that deviations from continuum prediction have been observed with both water liquid and liquid metal. One may link this result with the work of Song and Corry [122, 123]. They measured, via umbrella sampling method, the potential of mean force for water passing through CNTs. They found that the pore with radius $a_c = 4.6\,\text{Å}$ shows the highest energy barrier to water molecules in comparison with smaller ($a_c = 3.4\,\text{Å}$) or larger pores ($a_c = 5$ to $10\,\text{Å}$). These results highlight the existence of some singular radii, and are in quite good agreement with the present study. Pascal et al., who found that water inside CNTs is more stable than in the bulk, also highlight the presence of some singular radii [124]. They found that the nature of the favourable confinement of water changes dramatically with CNT diameter. Both relative entropy and relative enthalpy for water inside CNTs has been found by Pascal *et al.* to be non monotonic functions of the radius. Indeed, while water in the smallest tube (single-file) is stable thanks to an high relative entropy in comparison with bulk water, the stability of slightly larger tubes is ensure by a favourable enthalpy. This is another hint of the presence of singular radii.

Altogether, these observations confirm the existence of singular radii. Hence, one has to find the origin of the non monotonic behaviour of filling dynamics of water inside CNT. The fact that both water and metal liquids have shown non-monotonic filling dynamics with tube radius indicates that hydrogen bonds are not the key ingredient to describe the observed behaviour. By contrast, water and liquid metal, as all liquids, both structure themselves near solid surfaces. Hence one may wonder if the structuring of the fluid has an impact on the capillary filling dynamics. To illustrate the structuring of the fluid inside CNT, snapshots of fluid structure are given in figure 3.8. From single-file (a_c=3.9 Å) to quasi-continuum state ($a_c = 8.2\,\text{Å}$), the geometrical patterns shown by water molecules can be correlated to the velocity measurements presented in figure 3.4. The smallest tubes ($a_c = 3.5$, 4.3 and $4.7\,\text{Å}$) are single-file, i.e. molecules are standing/moving one behind the other. It appears from figure 3.4 that a_c=3.9 Å is filled by water, while

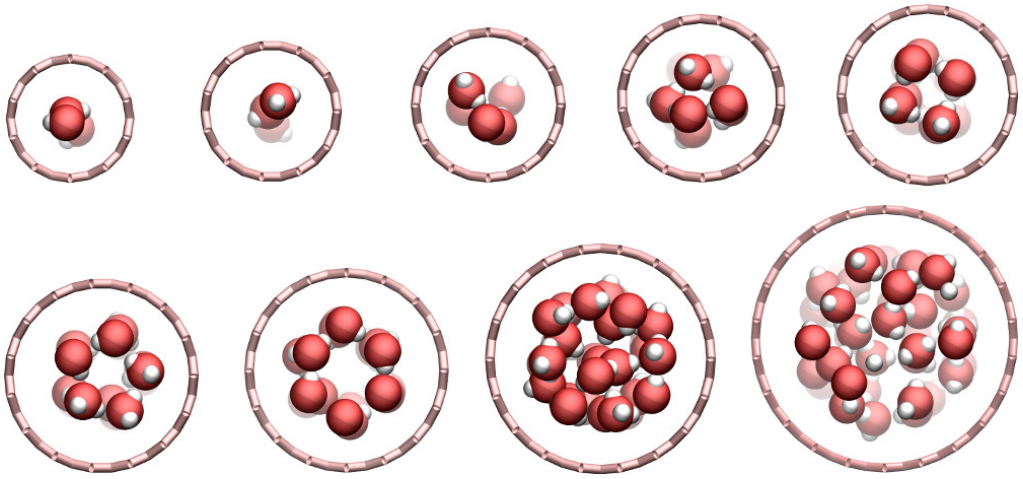

FIGURE 3.8: Snapshot of water molecules inside CNTs of various radii, $a_c = 3.9$, 4.3, 4.7, 5.1, 5.5, 5.9, 6.2, 7.0, 8.2 Å.

$a_c = 4.3$ and 4.7 Å are not. This may be understood by the fact that there is too much vacuum in the biggest single-file tubes, and it is not very profitable for water to fill it, since there is a large water-gas contact surface. This is obviously not the case for the smallest tube, in which water molecules are closely surrounded by carbon atoms, which should correspond to a large liquid-solid contact surface. In other words, there is a loss of water-carbon interactions from $a_c = 3.5$ Å to $a_c = 4.7$ Å. For the larger radii $a_c = 5.1$ and 5.5 Å, side-by-side molecules are allowed, and those tubes show an increase in capillary filling velocity. This is probably related to the very small amount of vacuum that is present in those tubes. For tube radii $a_c = 5.9$ and 6.2 Å, ring structure is observed, and the curve v_c versus a_c shows a local minimum. This minimum could be related to the cost of having vacuum in the centre of the tube and therefore, loosing water-water interaction energy rather than water-carbon as for smaller tubes. Finally, for the larger presented radii ($a_c = 7.0$ and 8.2 Å), the fluid loses its structure, corresponding to a velocity that tends toward the continuum value (~ 7 m/s).

Velocity and pressure measurements combined with water structure observations show that the structuring of the fluid is at the origin of the strong deviations observed from continuum predictions. Let us now give an analytical description of the observed behaviour.

3.3.1 Mathematical description

Continuum theory predicts that the filling dynamics is generated by a pressure drop $\Delta p = 2\Delta\gamma/a$ and limited by an entrance dissipation $\Delta p = C\eta Q/2a^3$. But this continuum expression does not include the effects coming from the discrete nature of the liquid. For example, for the smallest tubes (a_c = 3.9, 4.3 and 4.7 Å), the flow is single-file. However, for a slightly larger tube ($a_c = 5.5$ Å), four water molecules can fill the tube side-by-side, and so on. These strong structuring effects are good candidates to explain variations of the filling dynamics. They generate a disjoining pressure Π_d that can be added to the total pressure [125]. Π_d is a function of the ratio between the fluid molecules diameter σ and the tube radius a. The total pressure drop, previously defined as $\Delta p = p_L - p_0 = p_L$, can be written as

$$p_L = 2\frac{\Delta\gamma}{a} + \Pi_d. \tag{3.18}$$

One may then define an effective force per unit length $\Delta\gamma^* = \Delta\gamma + a\Pi_d/2$, to recover the classical expression for the Laplace pressure $p_L = 2\Delta\gamma^*/a$. While the expression of $\Delta\gamma^*$ as a function of the radius a is not trivial for a cylinder, the expression for the slit case (2D) can be found in the literature:

$$\Pi_d^{\mathrm{2D}}(h) = -\rho_\infty k_B T \cos\left(2\pi h/\sigma\right) e^{-h/\sigma}, \tag{3.19}$$

with σ the fluid particle diameter, ρ_∞ the bulk fluid density and h the distance between walls [47]. In equation (3.19), fluid particles are expected to be hard spheres and channel walls are expected to be smooth.

To test the validity of equation (3.18) together with (3.19), molecular dynamics simulations of water filling slit nanochannels were performed.

3.3.2 Capillary filling inside slits

To highlight that the disjunction pressure is at the origin of the non monotonic variations of the filling velocity as a function of the channel dimensions, MD simulations of water filling slit nanochannels were performed. The system was similar to the previous one, at the exception that the channel was made up with two planar graphene sheets, separated by a distance h_c. The

width w of the system was taken to be bigger than 10 nm to avoid finite size effects in the lateral direction. The distance h_c was varied from 7.2 to 18 Å.

From static measurements, the total capillary pressure p_L was evaluated in the spirit of CNTs measurements, see figure 3.9. In 2D, the total capillary

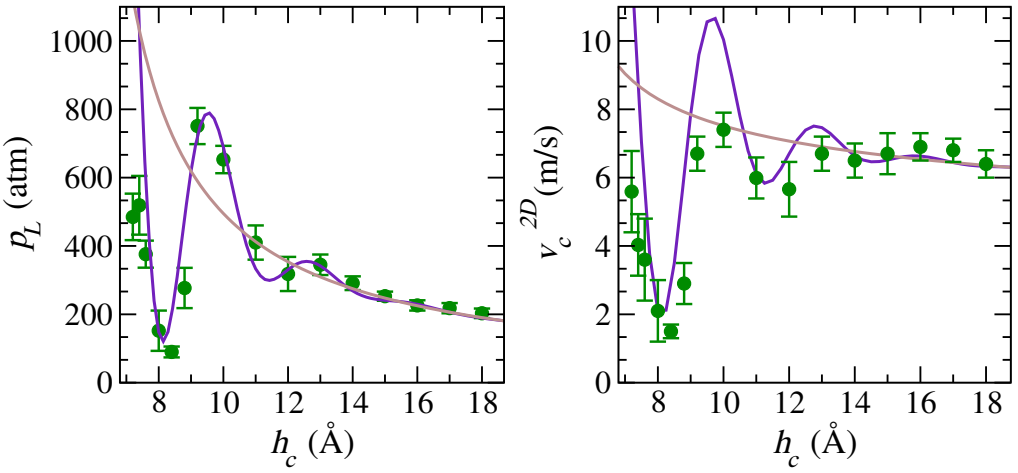

FIGURE 3.9: Left: Laplace pressure measured in static simulations. Symbols are molecular dynamics results. The brown line is the continuum prediction $p_L = \Delta\gamma/h$, i.e. without structuring effects, with $\Delta\gamma = 25\,\mathrm{mN/m}$ and with h an effective slit size defined as $h = h_c - 5\,\text{Å}$. The violet line corresponds to equation (3.20). Right: capillary velocity in slit v_c^{2D} as a function of the inter-plate distance h_c. Symbols are molecular dynamics results. The brown line is the continuum prediction $v_c^{2D} = \Delta\gamma/C^{2D}\eta$ with $\Delta\gamma = 25\,\mathrm{mN/m}$. The violet line corresponds to equation (3.22).

pressure can be written as

$$p_L = \frac{\Delta\gamma}{h} + \Pi_d^{2D}, \tag{3.20}$$

where Π_d^{2D} is given by formula (3.19), and h is the effective inter-slit distance taken to be $h \approx h_c - 5\,\text{Å}$. Equation (3.20) has been added to figure 3.9, as a comparison with molecular dynamics results. The agreement between theoretical predictions and molecular dynamics simulations is quite good, even if one has to add the following small corrections in the expression of the disjoining pressure:

$$\Pi_d^{2\mathrm{D},\,*}(h) = -\rho_\infty^* k_B T \cos(2\pi h/\sigma)\, e^{-\alpha h/\sigma} \tag{3.21}$$

where ρ_∞^* is a modified water bulk density, taken to be $\sim 3.5 \times \rho_\infty$ that the measured density, and α was taken to be ~ 1.5 and acts as a screening parameter. These adjustments have to be made since equation (3.19) applies

to a system of hard spheres, while the considered liquid is water. It highlights that the effect of the disjoining pressure is stronger for water than for a hard sphere system (at short inter-plate distance), but decreases faster with the inter-plate distance. A difference between water and hard sphere was expected since water molecules interact with each other with an orientation dependent potential [47].

On the other hand, the filling velocity is expected to write

$$v_c^{\mathrm{2D}} = \left[\Delta\gamma - h \times \Pi_d^{2D,*}\right] \frac{1}{\eta C^{\mathrm{2D}}} \tag{3.22}$$

where C^{2D} is the Sampson coefficient, here for the slit geometry, such as $\Delta p = C^{\mathrm{2D}}\eta Q/wh^2 = C^{\mathrm{2D}}\eta v_c^{\mathrm{2D}}/h$. C^{2D}, which is a function of h, was estimated from finite element calculations, in the spirit of chapter 2. A comparison between equation 3.22 and molecular dynamics simulations is shown in figure 3.9. As expected, the capillary filling velocity shows oscillations when varying the inter-plate distance h_c, and the qualitative agreement between theory and molecular dynamics simulations is good. Note a quantitative difference for $h_c \sim 9 - 10\,\text{Å}$, for which the measured velocity values are lower than predicted ones. This can be linked to the deviations observed in the case of the cylindrical geometry, see figure 3.6. Again, this could be due to entrance effects.

To synthesize, note that for growing inter-plate distance h_c, the number of water molecules in the direction normal to the slit vary from one to five for the considered situations. As previously observed with the tubes, this leads to changes in the fluid structure. It is clear, in the case of the slit, that each local maximum of velocity corresponds to $h/\sigma = 3/2$, $5/2$ etc, while local minima correspond to $h/\sigma = 1$, 2 etc. This confirms the major role played by structuring effects, and indicates that the disjoining pressure is at the origin of non-linearities in the filling dynamics inside subnanometric channels.

3.3.3 Illustration

As a final illustration, a Jurin-like experiment was performed. A gravity field g equal to $4 \cdot 10^{-4}\,\text{kcal/Å-g}$, i.e. twelve orders of magnitude larger than

the typical gravity magnitude on Earth, was applied along the tube axis, and the rise L of the fluid column inside the tube was recorded. A snapshot of the simulation is shown in figure 3.10. From the classical Jurin law, L is

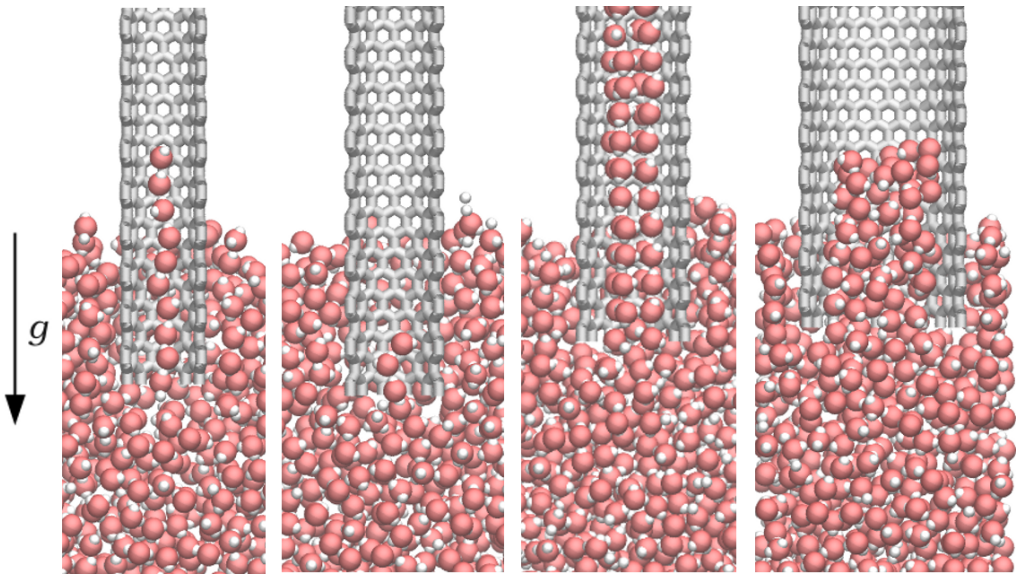

FIGURE 3.10: Ascension under a gravity field g (Jurin-like experiment) inside subnanometric nanotubes. Tube radius from left to right: 3.9 Å, 4.7 Å, 5.1,Å and 6.25 Å.

expected to be:

$$L = \frac{2\Delta\gamma}{\rho g a}. \tag{3.23}$$

So L should increase when the effective radius decreases. As expected from the current study, this is not the case for subnanometric channels, as seen in figure 3.10. To re-conciliate equation (3.23) with our results, one has to substitute $\Delta\gamma$ by $\Delta\gamma + a\Pi_d(a)$, with a the effective radius of the pore.

This illustrates an important consequence of the phenomenon discussed in this chapter. The imbibition of porous media with subnanometric pores is strongly affected by the discrete nature of the fluid and the resulting disjoining pressure. A striking phenomena being the possibility to switch pore from hydrophilic to hydrophobic just on specific radii values.

3.4 Conclusion

This chapter focused on the capillary filling of subnanometric carbon nanopores by a fluid. Molecular dynamics simulations indicated that the

capillary velocity strongly depends on the channel dimensions, particularly for tube radii below one nanometer. This is in contradiction with continuum hydrodynamics which predicts a filling velocity quasi-independent of the tube radius. During this study we observed that the fluid structuring inside the pore creates a disjoining pressure which adds to the classical Laplace pressure. The combination of continuum hydrodynamics and disjoining pressure allows to theoretically predict a capillary velocity which varies significantly with the channel size, especially for the very small channels. This has been discussed in the case of capillary filling inside a 2D geometry (slit), for which the expression of the filling velocity is known. Note that our predictions are not water-specific and concern most liquid types, as confirmed by results obtained with both water and a *simpler* liquid than water: a liquid metal. Finally, one has to notice that we only considered the complications linked to the appearance of a disjoining pressure. However, at the nanoscale, one could also have questioned the value of the surface tension at the meniscus. Indeed, some deviations from the macroscopic value are expected, and can be quantified by the Tolman length. Even if the present study shows that this effect is not dominant, it may still play a role.

A striking consequence of these results is the possibility to switch the pore behaviour from hydrophilic to hydrophobic for some specific radius values. For example, in the case of water filling CNTs, radii $a_c = 4.3 - 4.7\,\text{Å}$ have been found to show reverse capillary filling, contrary to continuum prediction. Moreover, tubes of radius $a_c = 3.9\,\text{Å}$ or $a_c \in [5.1 - 16]\,\text{Å}$ have been found to present lower filling properties in comparison with continuum expectations.

The present result may be of main importance in the study of the filling of nanoporous media. Indeed the hydrodynamic permeability of the medium is expected to vary non-monotonically with the pore size distribution and the effect can be quite brutal, particularly in the case of water filling porous medium whose nanopores radii are distributed around $3.9 - 5.1\,\text{Å}$. The Darcy law should be adapted to take into account disjoining pressure effects, for example by introducing a modified permeability K^*. Moreover, the present result could result in some consequences for the selectivity, with potential consequences for example in the understanding (and fabrication)

of selective ion channels [34], or in the study of confined ionic liquids in supercapacitors made of porous medium [126, 127].

In the end, this study allowed us to reach a very complex aspect of selectivity by giving a simple molecular (finite size) vision mostly based on geometrical arguments.

Chapter 4

Nanofluidic osmotic diodes

Contents

This chapter is based on the following publication:

- Clara B. Picallo, Simon Gravelle et al. Nanofluidic osmotic diodes: theory and molecular dynamics simulations. *Physical Review Letter* 2013 [128]

Abstract and main results – Analogous to diodes in solid state electronics, a nanofluidic diode is a system presenting an ionic current rectification when submitted to an external electrical potential drop. This property can be used to turn the ionic flow on and off depending on the polarity of the applied voltage. A nanofluidic diode usually consists of an asymmetric and charged nanochannel, as schematized in figure A.

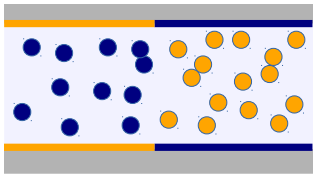

A

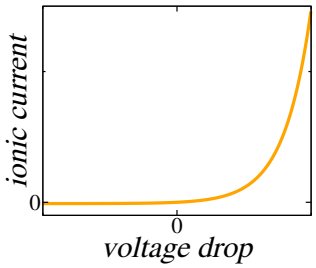

B

The ionic response to an applied electrical field of a nanofluidic diode has already been theoretically studied and experimentally observed, a typical current versus voltage response of a nanofluidic diode is presented in figure B. By contrast, this thesis is the very first work considering the behaviour of the solvent within a nanofluidic diode, even though controlling water flow using nanofluidic diodes opens up new prospects for desalination and water purification. In this chapter, we focus on the behaviour of the solvent inside a nanofluidic diode, and particularly on the osmosis phenomenon, i.e. the response to an applied salinity gradient.

We show that a surface charge asymmetry built on a nanochannel surface leads to non-linear couplings between the water flow and the ion dynamics, which results in a water flow rectification. A typical water flow versus an applied voltage drop curve is presented in figure C. Then, we explore the possibility of having rectification of flow under external forcing without electrical double layers (EDL) overlap. This possibility is of great interest since an EDL overlap requests channel dimensions close to the molecular size (or extremely low salt concentration) which constitutes an important technological constraint. Ionic and water rectifications without EDL overlap could be the first step toward an efficient desalination device.

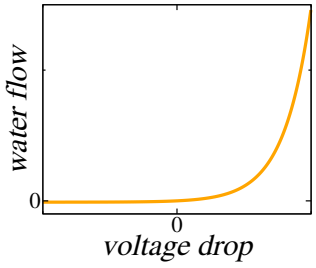

C

4.1 Introduction

This chapter focuses on nanofluidic diodes, an appealing application of nanofluidics. It consists of a nanochannel which allows to conduct ionic current preferentially in one single direction (and inhibits the current flow in the opposite direction). Accordingly, a nanofluidic diode rectifies the ionic current depending on the polarity of the applied electric-field, analogous to a diode in solid-state electronics [129]. This section starts with a brief state-of-the-art relating to nanofluidic diodes. Then it provides a short description of the qualitative behaviour of this component. Finally it presents the road-map of the present chapter.

4.1.1 State of the art

Investigations on nanofluidic diodes have started only recently, with a theoretical study of nanochannels bearing an *asymmetric surface charge* (for an illustration see figure 4.1). In 2005, Daiguji et al. theoretically predicted the rectified ionic current across nanofluidic channels with a tuned surface charge density [13]. Based on Poisson-Nernst-Plank (PNP) and Navier-Stokes equations, they found that tuning the surface charge in an asymmetrically charged nanochannel allows to modulate ion current. Two years latter, Karnik et al. experimentally measured the rectified ionic current in a nanofluidic diode fabricated by introducing a surface-charge discontinuity [22]. They studied the current-voltage response of the diode and found a large rectification, which depends on the salt concentration. Nanofluidic diodes have also been obtained by tuning the channel's geometry, i.e. by using an *asymmetric shape* rather than an asymmetric charge. Indeed, asymmetric nanochannels have been found to lead to similar electrical current rectifications, as reported by Siwy et al. [130–133]. Note that nanopores pierced in solid membranes are often asymmetric, since they are conically shaped due to the shape of the beam used to drill them. Usually, a nanofluidic diode's response to an external forcing is well described by 1D-PNP equations [13, 134, 135], which will be used in this study.

Until now, most groups have focused on the ionic response of a nanofluidic diode to an external electric potential. To extend these studies, its osmotic

response will be considered in the first part of this chapter. In particular, we show that a nanofluidic diode can be used to rectify water flow. Also, nanofluidic diodes have mostly been studied in the case of an electrical double layer overlap. It corresponds to the case where the Debye length λ_D (see section 1.2.1) is comparable or larger than the channel height h. The possibility of rectifying flux without Debye overlapping is evidenced in the second part of this chapter.

4.1.2 A brief description of nanofluidic diodes

A nanofluidic diode generally consists of a charged nanochannel pierced in a membrane, and presenting an asymmetry. A drawing of a typical nanodiode is shown in figure 4.1. The nanochannel of length L and height h separates two reservoirs of bulk salt concentration c_0. The channel is asymmetrically charged, with a surface charge Σ on the left, and a surface charge $-\alpha\Sigma$ on the right, with α a constant, typically taken to be positive. To ensure electroneutrality, EDLs build up at the charged surfaces, and they may overlap depending on the height of the channel and salt concentration. Depending on the applied voltage ΔV, counterions may be either depleted (figure 4.1 middle) or accumulated (figure 4.1 bottom) in the transition zone, i.e. in the middle of the channel. This leads respectively to a blocked state with a weak ionic current crossing the diode, or an open state, with a high ionic current. The typical ionic current I_e crossing the nanodiode as a function of the applied voltage drop ΔV can be written as

$$I_e = I_{\text{sat}} \left(e^{\Delta V e \beta} - 1 \right), \tag{4.1}$$

where I_{sat} is a saturation current and $\beta = 1/k_B T$. Formula (4.1) is plotted in figure 4.1, with a comparison with the expected (linear) response of a uniformly charged nanochannel. Note that for a large voltage drop difference formula (4.1) do not applies any more, and a linear response I_e versus ΔV has to be recovered. The important consequence of formula (4.1) is that, depending on the applied potential drop ΔV, one can turn on and off the ionic current by simply changing the electric field polarity.

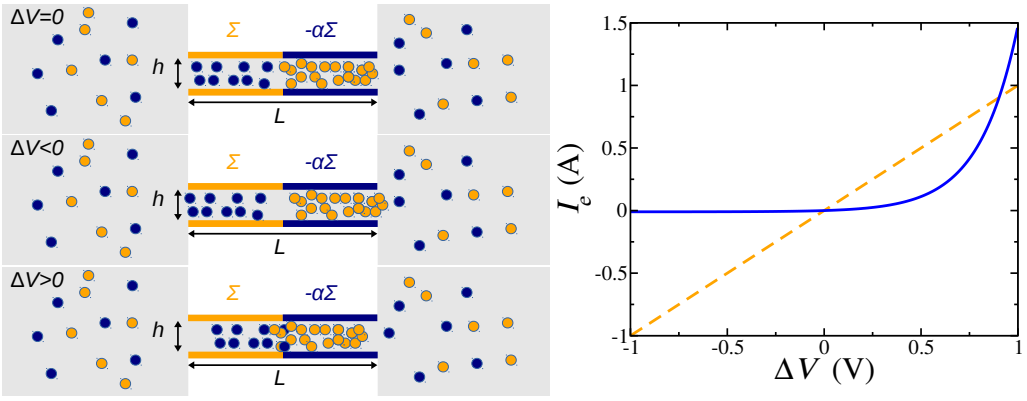

FIGURE 4.1: Left: a nanofluidic diode with counterions. Up: no external forcing ($\Delta V = 0$). Middle: negative external potential drop ($\Delta V < 0$), the diode is blocked. Down: positive external potential drop ($\Delta V > 0$), the diode is open. Right: typical current i_e versus applied voltage drop ΔV signal, in a nanofluidic diode (continuum blue line) and in a simple nanochannel (dashed orange line).

4.1.3 Outline

This chapter is based on the study of the solvent inside a nanofluidic diode, and particularly on its coupling with an external forcing such as an electric field or a salt concentration gradient. In a first part, we study the possibility of using a nanofluidic diode to control the water flow in a regime of electrical double layer overlap. Then, we extend the study in a regime of no-overlapping electric double layer and show that a diode-like behaviour is expected in this case as well.

4.2 Controlling water flow with a nanofluidic osmotic diode

The ability of a nanofluidic diode to rectify ionic current has been widely studied theoretically and measured experimentally. By contrast, the coupling between the diode and the solvent had not been explored at the beginning of this thesis, and is at the basis of the present chapter. Theoretical equations are derived, and supported by molecular dynamics results.

4.2.1 Theoretical model

Osmotic pressure – Let us consider the classical osmosis, which appears in the configuration where a semipermeable membrane separates two reservoirs containing a solvent and a solute (water and salt here). If a solute concentration difference Δc exists between reservoirs, an osmotic pressure drop $\Delta\Pi$ builds up and induces a water flow toward the reservoir with the largest salt concentration. The expression of the osmotic pressure difference is given by the van't Hoff formula [136]

$$\Delta\Pi = k_B T \Delta c. \tag{4.2}$$

Note that equation (4.2) applies to ideal solutions with infinitesimal concentration difference.

Apparent osmotic pressure – However, in full generality the nanochannel is usually only partially semipermeable, meaning that ions may still permeate through it, although this process is strongly affected by the surface charge [52]. This gives raise to an apparent osmotic pressure, which is defined hereafter. As seen in subsection 1.2.5, inside a charged nanochannel, the force balance on the fluid takes the form of the Stokes equation for the velocity field $\vec{v}$ and the hydrodynamic pressure p, with a supplementary electric force $\rho_e\,(-\vec{\nabla}V)$ due to the local charge imbalance inside the EDLs

$$\eta\nabla^2\vec{v} = \vec{\nabla}p - \rho_e\,(-\vec{\nabla}V), \tag{4.3}$$

where $\rho_e = e(\rho_+ - \rho_-)$ is the local charge density ($\rho_\pm$ the density of cations and anions, assumed to be monovalent), e the elementary charge, η the fluid viscosity, and V the local electric potential. Integrating equation (4.3) over the nanochannel allows to express the total water flux Q as

$$Q = -K\left[\Delta p - \Delta\Pi_{\text{app}}\right], \tag{4.4}$$

with K the hydrodynamic permeability of the channel, and $\Delta\Pi_{\text{app}}$ the total electric driving force per channel cross section A, defined as

$$\Delta\Pi_{\text{app}} = \frac{1}{A}\int \mathrm{d}A \int_0^L \mathrm{d}x\,\rho_e\,(-\vec{\nabla}V), \tag{4.5}$$

where L is the length of the channel. Combined with equation (4.4), this allows to interpret the electric force acting along the channel, $\Delta\Pi_{\text{app}}$, as an apparent osmotic pressure. Considering an absence of steric exclusion of the ions in the permeable pore, only this contribution to the osmotic pressure exists, so that $\Delta\Pi_{\text{app}}$ identifies with the full osmotic pressure.

Connecting the osmotic pressure and the ionic flux – To connect $\Delta\Pi_{\text{app}}$ to the ion fluxes $J_\pm$ through the nanochannel, we assume that the ion dynamics obeys the Poisson-Nernst-Planck (PNP) transport equations [2]. By doing this, we assume a 1D geometry with the various quantities averaged over the cross area, depending only on the x-coordinate along the channel [137]. The detailed equations are presented in appendix A. The PNP framework introduces the ion fluxes as a key quantity, defined as

$$J_\pm = -D\nabla c_\pm \mp \mu c_\pm \nabla V, \tag{4.6}$$

with D the ion diffusion coefficient and $\mu = eD/k_BT$ the (electrical) mobility, taken to be the same for both species. In the stationary state, the ion fluxes are homogeneous in space and time, leading to a spatially constant electric current $I_e = e(J_+ - J_-)$ and a solute flux $J_i = J_+ + J_- = -D\nabla c - \mu\rho\nabla V$, with $c = c_+ + c_-$ the total ion concentration and $\rho = c_+ - c_-$ the difference in salt concentration between + and - species. Using this relation to express the electric force $\rho_e\,(-\nabla V)$ as a function of the solute flux J_s, equation (4.5) can thus be rewritten as

$$\Delta\Pi_{\text{app}} = k_BT\left(\Delta c + J_i \times \frac{L}{D}\right), \tag{4.7}$$

where $\Delta c = 2(c_R - c_L)$ is the salt concentration difference (the factor two coming from the two ion species), and where c_R and c_L are salt concentrations in the right and left part of the channel, respectively. Note that an equivalent relation was obtained by Manning [138], using a generic potential-energy profile to represent the membrane. In the absence of solute flux, $J_i = 0$, the previous equation reduces to $\Delta\Pi_{\text{app}} = k_BT\,\Delta c$, i.e. matches the van't Hoff expression for the osmotic pressure drop across a perfectly semi-permeable membrane (equation (4.2)). For a fully permeable neutral channel, $J_i = -D\,\Delta c/L$ and $\Delta\Pi_{\text{app}} = 0$, which is also expected. In general the nanochannel is only partly permselective and $\Delta\Pi_{\text{app}}$ takes a non-vanishing

value depending on the solute flux. Thus the driving force acting on the water takes the value $\Delta p_{\text{tot}} = \Delta p - \Delta\Pi_{\text{app}}$, and $\Delta\Pi_{\text{app}}$ is the apparent osmotic pressure that one needs to overcome in order to counteract osmosis.

Towards the osmotic diode – We can now obtain an analytical expression for the apparent osmotic pressure based on equation (4.7). In the following we will discuss more specifically a geometry with an asymmetric surface charge, as sketched in figure 4.2: the left side has a positive surface charge density Σ while the right side has a negative surface charge $-\alpha\Sigma$, with $\alpha > 0$ a numerical coefficient. In a similar geometry, for the ionic diode,

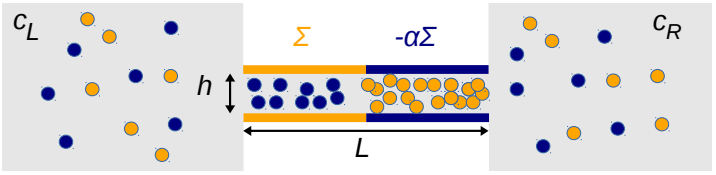

FIGURE 4.2: Scheme of the system showing the asymmetry of the surface charge in the nanochannel, and the different salt concentrations in the left and right reservoirs.

it has been shown that the corresponding 1D PNP equations obeyed by the ion concentrations can be solved for an applied voltage drop ΔV across the nanochannel [22, 139, 140]. In contrast, no solution exists yet for the response under an *osmotic* gradient Δc. Deriving such a solution was the initial purpose of this work. Our derivation follows the general strategy of previous works [22, 139, 140].

Transition zones – Now, one should treat specifically the discontinuities associated with the step change of surface charge between the two reservoirs and the inner nanochannel ends, as well as at the junction between the two sides of the nanochannel with different surface charges. Following previous descriptions [22, 139, 140], which made use of the analogy with p-n junctions in semiconductors, one may treat these discontinuities by neglecting the extension of the space charge zone and writing accordingly the continuity of the electro-chemical potential. Neglecting the subtle effects at junctions and channel ends constitutes obviously a simplifying assumption, which allows to obtain an analytical prediction for the transport properties and osmotic pressure. However such assumptions were shown to provide *in fine* a good description of transport, comparing favourably with experiments and numerical calculations [22, 140].

First, one may notice that the surface charge carried by the walls leads to a local ion charge imbalance inside the nanochannel,

$$c_+ - c_- = -2\frac{\Sigma}{he} \text{ (on the left)}, \tag{4.8}$$

$$c_+ - c_- = 2\frac{\alpha\Sigma}{he} \text{ (on the right)}. \tag{4.9}$$

Moreover, at equilibrium (i.e. $c_R = c_L = c_0$), a Donnan potential V_D builds up in the nanochannel in order to ensure a spatially homogeneous electrochemical potential over the system [2]

$$\mu_\pm = k_B T \log(n_\pm) \pm eV_D \equiv \mu_0 = k_B T \log(n_0), \tag{4.10}$$

where $\mu_\pm$ is the electrochemical potential of $\pm$ species, and $n_\pm = c_\pm/c_0$ the dimensionless concentration normalized by the average concentration c_0. Along with the charge electroneutrality condition, equation (4.10) allows to link the local ion concentrations and the electrical potential in the different parts of the system. Details are given in the appendix A.

Out-of-equilibrium – Now, under the combined action of a voltage drop ΔV and an osmotic forcing Δn, non-equilibrium ion fluxes $J_\pm$ build up in the system. Using the spatial homogeneity of the fluxes along the nanochannel in the stationary state, one can deduce the spatial dependence of ion densities and potential. One gets a system of 6 equations and 6 unknowns (I_e, J_i, the concentration values near the central junction (x2) and the potential values near the central junction (x2)), that can be solved numerically (appendix A). However, an analytical expression for I_e and J_i can be obtained in the regime of *high surface charge* also called *large Dukhin number limit*.

Large Dukhin number limit – Altogether, in the regime $\mathrm{Du} \gg 1$, with Du the Dukhin number defined as the ratio between the Dukhin length and the channel size $\mathrm{Du} = \ell_{\mathrm{Du}}/h$, one obtains analytical expressions for the concentration profiles and electrostatic potential, as well as for the corresponding solute and electric fluxes:

$$J_i = \frac{D}{L}\left(2\frac{(n_R - n_L)}{\mathrm{Du}} - \frac{\alpha - 1}{\alpha\,\mathrm{Du}}\frac{n_R}{n_0}\left[n_L e^{\Delta\phi} - n_R\right]\right) \tag{4.11}$$

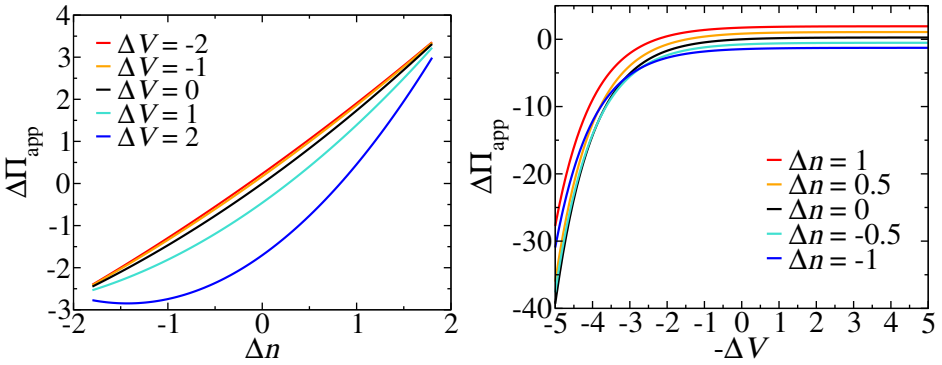

FIGURE 4.3: Apparent osmotic pressure $\Delta\Pi_{\text{app}}$ versus the salinity gradient $\Delta n = n_R - n_L$ (left) and applied voltage $\Delta V = V_R - V_L$ (right) obtained from equation 4.13. All the quantities are depicted in reduced units of k_BT, k_BT/e, and c_0 (average salt concentration); $\text{Du} = 3$, $\alpha = 5$.

and

$$I_e = \frac{e}{\alpha - 1}\left[(\alpha + 1)\, J_i - 4\, D \frac{(n_R - n_L)}{\text{Du} L}\right]. \tag{4.12}$$

Using equation (4.7), one deduces an analytical expression for the apparent osmotic pressure in the large Dukhin number limit:

$$\frac{\Delta\Pi_{\text{app}}}{k_BT} = 2\left(1 - \frac{1}{\text{Du}}\right)(n_R - n_L) - \frac{\alpha - 1}{\alpha\, \text{Du}} \frac{n_R}{n_0}\left[n_L e^{\Delta\phi} - n_R\right]. \tag{4.13}$$

The apparent osmotic pressure thus exhibits a rectified salinity gradient contribution, coupled to a strong non-linear dependence on the imposed voltage, with an exponential form that resembles the characteristic equation of a semiconductor diode, see figure 4.3. Note that the apparent divergence of the second term as $\alpha \to 0$ is due to the assumption of a high Dukhin number. Finally, we emphasize here that the predicted exponential dependency of the fluxes with the applied voltage ΔV results from the increasingly large potential gradients inside each part and at junctions inside the channel, and not from an increased salt concentration inside the channel (see appendix A for details). The previous expression applies for moderate applied voltage, while for very large voltage $e\Delta V/k_BT \gg 1$, the system goes back into a linear regime with a linear dependence of the fluxes on ΔV, associated with surface conduction (see appendix A).

Recalling that in the absence of applied pressure drop $\Delta p = 0$, the flow rate Q is proportional to $\Delta\Pi_{\text{app}}$, see equation (4.4), this rectified osmotic pressure directly translates into a *rectified water flow*. It thus behaves as an *osmotic diode*. To highlight the analogy to Shockley diodes, one may gather

formally the various terms in equation (4.13) to write the water flux as

$$Q = K\xi\, k_B T \Delta c + Q_{\mathrm{S}} \left[e^{\Delta\phi} - 1 \right], \tag{4.14}$$

where the expression for the reflection coefficient $\xi(\delta, \alpha, n_L, n_R)$ follows immediately from equation (4.13), and Q_{S} plays the role of a "limiting water flux" with

$$Q_{\mathrm{S}} = K \times k_B T\, c_R c_L \frac{1-\alpha}{\alpha \mathrm{Du} c_0}. \tag{4.15}$$

This phenomenon opens the way towards an elaborate control of fluid flows at the nanoscale, by coupling salinity and electric gradients.

In order to assess these counter-intuitive behaviours, we present the results of molecular dynamics simulations of ion and water transport inside a nanochannel, using the LAMMPS package [82]. In view of the computational cost required, we have conducted these simulations at two different levels. In a first set of simulations, we focused on the ion dynamics, using an implicit solvent. The full ion dynamics was explicitly computed, and the solute flux and electric current were measured. In a second set of simulations, both water molecules and ions were included, and the water flow was measured.

4.2.2 Implicit solvent simulations

Method – Using the LAMMPS software [82] we performed molecular dynamics simulations in a setup like figure 4.2. A FCC lattice of fixed atoms is used to build the channel walls. Water is modelled only in an implicit way, as a medium that has the dielectric permittivity of water $\epsilon_r = 80$. The interaction between the solute and the water molecules is mimicked by applying a Langevin thermostat on the ions [141]. The same damping time $\tau = 23\,\mathrm{fs}$ – controlling the amplitude of the viscous drag in the Langevin model – is imposed for both species, to ensure that they have the same diffusion coefficient, with a value $D \approx 2 \times 10^{-9}\,\mathrm{m}^2/\mathrm{s}$, close to the experimental ones for typical microions. The atomic mass of the species is chosen to be $m_{n_+} = m_{n_-} = 39.1\,\mathrm{g/mol}$, and we consider monovalent ions. A Weeks–Chandler–Andersen potential, keeping only the repulsive part of the Lennard-Jones potential, was applied. All particles (ions and solid atoms)

share the same size $\sigma = 3.74\,\text{Å}$. Long-range Coulombic interactions were calculated by means of a particle-particle particle-mesh (PPPM) solver.

At each side of the junction, charges were homogeneously distributed between the wall atoms at the surface, and the required amount of counterions to ensure electroneutrality was placed in the vicinity of the walls. For the $\Delta n = 0$ case we used a single diode in contact with left and right reservoirs with the same concentration and periodic boundary conditions (PBC) in all space directions. A channel width equal to the Debye length $\lambda_D = 15\,\text{Å}$ was imposed to ensure Debye overlap. Each side of the diode in the x and y directions, as well as the reservoirs, had a length equal to $5\lambda_D$ to ensure that the concentration and voltage profiles reached a plateau value. To induce a voltage drop across the channel while keeping PBC, we imposed an electric field E_x to the system (in practice, by applying an electric force $F_x = qE_x$ on charged particles, with q the particle charge) [142].

To avoid PBC problems in the $\Delta n \neq 0$ case, we constructed a double diode system containing two diodes in series along the x direction in such a way that the right reservoir of the first diode was also the left reservoir of the second one, and vice versa. We inverted the orientation of the second diode in a way that allows to impose PBC in all space directions, and from the same simulation we obtain the results for $(\Delta n, -\Delta V)$ from the first channel and for $(\Delta n, +\Delta V)$ from the second channel.

Results – The osmotic pressure is defined in terms of the solute flux J_i according to equation (4.7). Figure 4.4 (left) presents MD results for the dependence of osmotic pressure with the salinity gradient, under several imposed voltage drops. Despite fluctuations due to thermal noise, a very good agreement with the theoretical predictions of equation (4.13) (solid lines) is found. In particular, the asymmetric behaviour can clearly be observed. In figure 4.4 (right), the molecular dynamics simulations reveal a clear diode-like behaviour for the osmotic pressure versus voltage drop, in agreement with the theoretical prediction (solid line). The voltage values reported here were taken from the direct measurement of the electric potential profiles measured in the system. These are computed using the Coulomb law, taking into account the contributions of all charges in the system and of the external applied field.

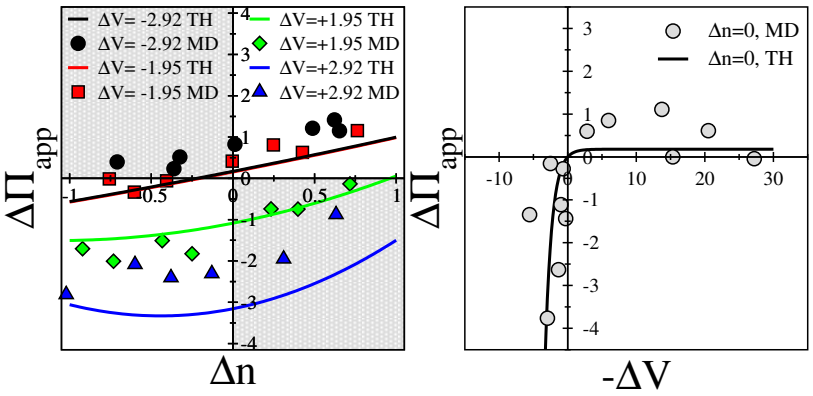

FIGURE 4.4: Comparison of the theoretical (TH) and molecular dynamics (MD) simulations results for the apparent osmotic pressure versus the osmotic gradient (left) and the applied voltage (right). The water flux is expected to be proportional to $\Delta\Pi_{\text{app}}$. Surface charges are chosen such that the surface-to-bulk-charge ratios are $\text{Du}_L = 5$ and $\text{Du}_R = -\alpha \text{Du}_L$, with $\alpha = 10$. All the quantities are depicted in reduced units of k_BT, k_BT/e, and n_0 (average salt concentration).

In a second, more detailed level involving full complexity, we performed a restricted number of simulations with full ion and water dynamics to highlight the rectified water flux we analytically predicted.

4.2.3 Explicit solvent simulations and reverse water flow

We present results of molecular dynamics simulations using water as an explicit solvent. The aim here was to build a realistic system in which water is explicitly described.

Method – Molecular dynamics simulations were performed in a setup similar to the one in figure 4.2, used for the implicit solvent simulations. The diode walls consist of an array of graphene sheets with homogeneously distributed charges. Each side of the horizontal slabs is positively or negatively charged, with a surface charge Σ and $-\alpha\Sigma$ respectively. As shown in figure 4.5 a system of parallel horizontal graphene slabs creates an array of diodes working in parallel. The simulated systems contained ~ 5000 water molecules, and five potassium and chloride atoms were typically present in each reservoir. In the spirit of [143], air-water interfaces are created at the two ends of the water reservoirs (not shown in figure 4.5). This ensures that the left and right reservoirs are independent and at the same (liquid/vapor

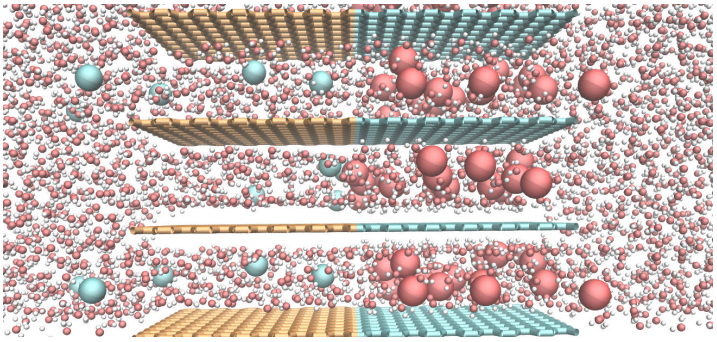

FIGURE 4.5: Snapshot of the simulation made with VMD [74], with counterions and water molecules.

coexistence) pressure, although periodic boundary conditions are imposed in all directions.

The AMBER96 force field [117] was used, with TIP3P water, and water-carbon interaction modeled by a Lennard-Jones potential between oxygen and carbon atoms, with parameters $\varepsilon_{OC} = 0.114\,\text{kcal/mol}$ and $\sigma_{OC} = 3.28\,\text{Å}$. The values of the Lennard-Jones parameters for ions were taken as in reference [144] to avoid the formation of unrealistic clusters of ions in a very confined geometry. Long-range Coulomb forces were computed using the particle-particle particle-mesh (PPPM) method. Water molecules were held rigid with the SHAKE algorithm. A time step of 2 fs was used. The positions of the carbon atoms were fixed. Water molecules and ions were kept at a constant temperature of 300 K using a Nosé-Hoover thermostat, applied only to the degrees of freedom perpendicular to the flow direction, with a damping time of 100 fs.

A channel width $h = 12\,\text{Å}$ was used, which provides a good Debye overlap, since the Debye length λ_D is equal to $\lambda_D = 8\,\text{Å}$. Each side of the diode measured $3\lambda_D$ in the x and y directions, which gives almost flat concentration and voltage profiles on each side. The reservoirs and vacuum layers measured $\sim 10\lambda_D$. Besides the air-water interfaces, a vertical graphene wall is also included in the vacuum part of one side (not shown in figure 4.5) to assure that no evaporation occurs from one side to the other and hence water transfer can only occur through the channels.

Results – This system is obviously much heavier computationally speaking than the previous one (subsection 4.2.2) and hence we cannot perform exhaustive measurements with it. However, these simulations allow to

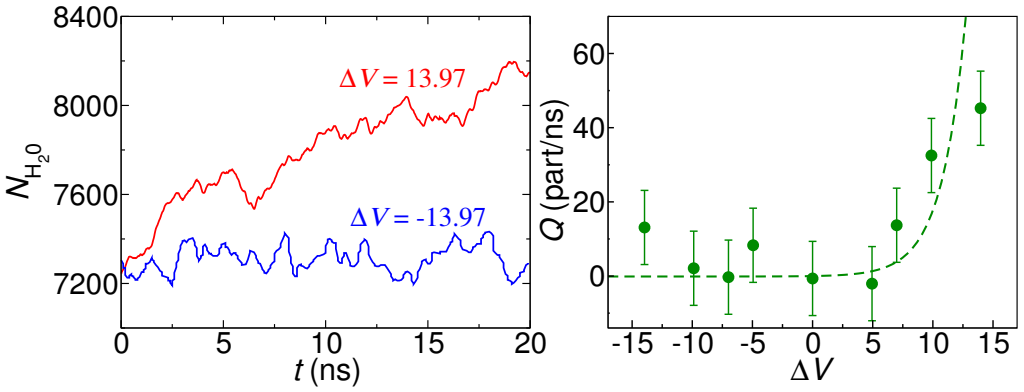

FIGURE 4.6: Left: Evolution of the amount of water molecules after 20 nanoseconds for one positive and one negative value of ΔV, with salt concentration $n_R = n_L = 0.15\,\mathrm{M}$; the surface to bulk charge ratios are $\delta_L = 3$, $\delta_R = 12$. All curves are the average over five realizations of the simulations with a duration of 20 nanoseconds. Right: flux $Q = \Delta N_{\mathrm{H_2O}}/\Delta t$ versus the normalized applied voltage drop ΔV. The dashed line is an adjustment using the expression $Q = Q_s\,(\exp[\Delta V] - 1)$ with $Q_s = 9 \cdot 10^{-4}\,\mathrm{ns}^{-1}$. The voltage is depicted in reduced units of $k_B T/e$..

observe the same behaviour as previously, which confirms the validity of the implicit solvent simulations. Indeed, the resulting diode-like water flow is illustrated in figure 4.6 for $\Delta n = 0$. We evidence here an asymmetric flow response as a function of the applied voltage: for sufficiently high and positive $\Delta\phi = \Delta V \times e/k_B T$ a non-vanishing water flow builds up in the system, while for $\Delta\phi < 0$ the flow can hardly be distinguished from the thermal fluctuations (and from the equilibrium situation $\Delta\phi = 0$). This rectifying behaviour of the water flow under voltage drop is in agreement with the theoretical prediction in equation (4.14).

4.2.4 Summary

Here we demonstrated the possibility of using a nanofluidic diode to rectify the solvent flow. Using a PNP-based theory, a water flow rectification, depending on the applied salt gradient and electrical potential has been predicted. Molecular dynamics simulations confirmed these predictions.

In particular, due to the diode-like dependence of water flux on voltage drop, an oscillating voltage drop is expected to induce a net water flow, which (as quoted above) can be interpreted in terms of rectified electro-osmosis. This

is reminiscent of the nanoscale pumping of water by an AC electric field or oscillating charge, recently evidenced by molecular dynamics simulations [145, 146].

Until now, we studied the nanofluidic diode in the configuration of electrical double layer overlap. Hereafter, we present an extension of this study to the case where the channel height h is large in comparison to the Debye length λ_D. We will start by exposing the motivations of such a study. Then we will present molecular dynamics simulations results and a theoretical model which will be compared with results from finite element calculations.

4.3 A nanofluidic diode without EDLs overlap

4.3.1 Motivations

The overlap of the Electrical Double Layers (EDLs) induces strong electrostatic interactions in the nanochannel, which markedly modify the ion dynamics, as seen previously. Nevertheless, the characteristic width of EDL layers is given by the so called Debye length λ_D, which scales with the bulk salt concentration c_0 as $\lambda_\mathrm{D} \sim 1/\sqrt{c_0}$. For example, with sea water for which the salt concentration is approximately $c_0 \approx 0.6\,\mathrm{M}$, the Debye length is $\lambda_D \approx 0.4$ nm. Therefore, it is a major technological challenge to fabricate channels for which an overlap of the EDLs exists.

However, the importance of surface charge effects in comparison with bulk effects is given by the Dukhin length ℓ_Du defined as the ratio between the surface charge Σ and the salt bulk concentration c_0 (see subsection 1.2.1):

$$\ell_\mathrm{Du} = \frac{|\Sigma|}{c_0 e}.$$

If the Dukhin length is at least comparable to the channel size, one may expect surface effects to play a major role in transport phenomena, regardless of the size of the EDLs. Hence, it should be possible to get a diode-like behaviour (an asymmetric force-flux response) using a channel with no EDL overlap. The aim of the present section is, first, to highlight numerically

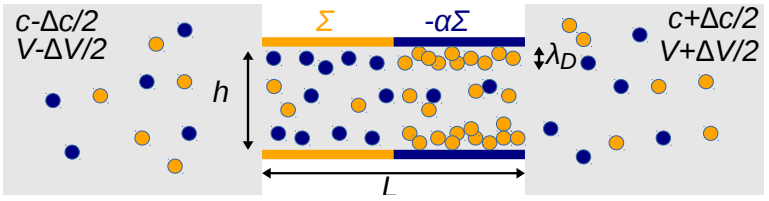

FIGURE 4.7: Sheme of the diode with counter ions (blue and orange discs) and surface charge (blue and orange lines).

this possibility, and then to propose an analytical model for nanofluidic diodes with no EDL overlap.

As a first step, we used molecular dynamics simulations to confirm the existence of rectification effects without overlap of EDLs, but in a surface-dominated regime, where h is the channel width (i.e. $\ell_{\mathrm{Du}} > h > \lambda_D$). Note that Laohakunakorn et al. experimentally observed water flow rectifications in a conical nanopore without EDLs overlap [147]. Then we present an analytical model based on PNP equations. The model is based on the hypothesis that a 1-D model, in which variables are averaged over the other dimensions, captures most of the physics governing flux responses to external forcing, in the footstep of Dydek et al. [137]. Finally, we compare our model with finite element calculations and show a quite good agreement.

4.3.2 Numerical evidence of rectification without Debye overlap

To confirm the existence of a diode-like behaviour without electrical double layer overlap, we performed molecular dynamics simulations. The goal is to measure the ionic current I_e in a asymmetrically charged nanochannel as a function of the external forcing ΔV, and show the asymmetry of the current-force response.

Simulation details – In view of the computational cost required, we have conducted these simulations using an implicit solvent only. The full ion dynamics is explicitly computed, and the solute flux and electric current are measured. The geometry of the system is represented of figure 4.8. The tube radius was equal to $a = 3\,\mathrm{nm}$, the length $L = 12\,\mathrm{nm}$ and the surface charge was $\Sigma = 140\,\mathrm{mC/m^2}$ on the left side and $-\alpha\Sigma$ with $\alpha = 2$ on the

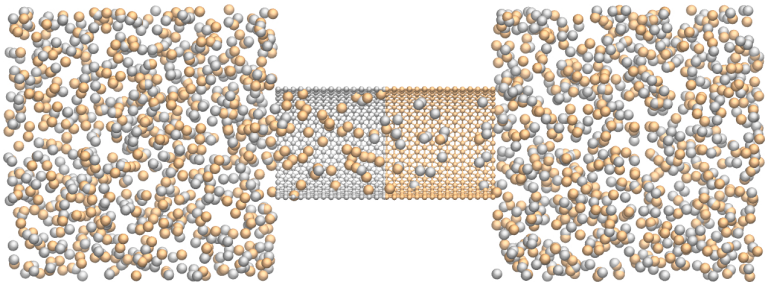

FIGURE 4.8: Sectional view of the diode with counter ions used for molecular dynamics simulations. Image made using VMD [74]. The two colours are associated respectively to the two charges.

right side. The averaged bulk salt concentration was $c_0 = 1\,\mathrm{M}$, then the Debye length was equal to $\lambda_D \sim 3\,\text{Å} \sim a/10$ and the Dukhin length was equal to $\ell_{\mathrm{Du}} \sim 150\,\mathrm{nm}$ on the left and $300\,\mathrm{nm}$ on the right.

Method – The details of the simulation are mostly the same as in part 4.2.2, hence we will only specifies the differences here. Charged fixed atoms combined with solid flat walls are used to build up the channel. Solid flat walls interact with the liquid by generating a force on the atom in a direction perpendicular to the wall. A channel radius equal to ten times the Debye length $\lambda_D = 3\,\text{Å}$ is chosen to ensure a clear non overlap of EDLs. Each side of the reservoir had a length equal to $50\lambda_D$ in the x, y directions, and $100\lambda_D$ in the z direction. This ensures that the concentration and voltage profiles reached a plateau value. We use a diode in contact with the left and right reservoirs, with the same concentration and periodic boundary conditions in all space directions.

Note that the chosen geometry here is cylindrical (i.e. fully 3D), while the simulations in the Debye overlap configuration (previous section) have been performed in a slit geometry (2D). This is a recent choice we made because a potential W solution of $\triangle W = 0$ decreases faster in a 3D geometry than in a 2D geometry (respectively $W \sim 1/r$ and $W \sim \ln(r)$), with r the characteristic distance from the source of the potential. Hence, for a given reservoir size, finite size effects are expected to be minimized in a 3D geometry.

Results – The electric potential drop ΔV was varied in absence of salt concentration difference between the right and left reservoirs ($\Delta n = 0$). Figure 4.9 shows the measured ionic current I_e as a function of the applied

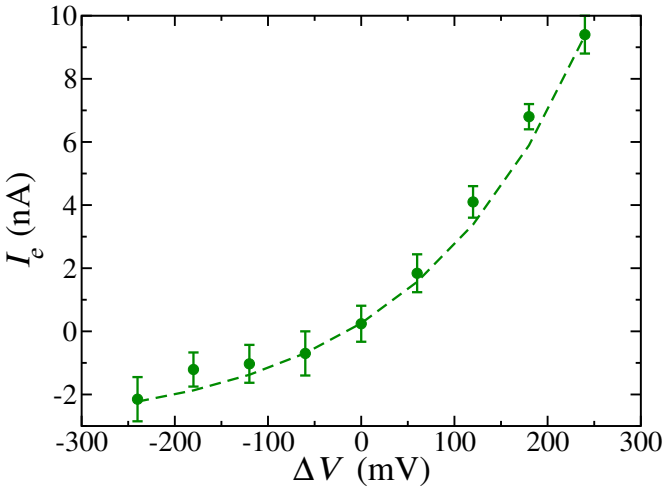

FIGURE 4.9: Ionic current I_e versus voltage drop ΔV obtained from molecular dynamics simulations. The dashed line is an adjustment using the expression $I_e \sim I_s(\exp(e\Delta V/k_BT) - 1)$ with $I_s = 5\,\mathrm{nA}$.

voltage drop. The molecular dynamics simulations reveal a clear diode-like behaviour in the absence of electric double layer overlap. Hence, in the next part, we propose a model based on PNP equations to describe the transport in this regime.

4.3.3 Theoretical model

System – Let us consider a channel separating two sub volumes, containing an electrolyte as depicted in figure 4.10. Driving forces are applied along x, and the length of the channel L is assumed to be way larger than its height h: $L \gg h$. A contrast in the surface charge exists between the two half-sides of the channel: Σ on $-L/2 < x < 0$ and $-\alpha\Sigma$ on $0 < x < L/2$ with α a positive numerical constant. The corresponding Dukhin numbers, defined as the Dukhin length ℓ_{Du} divided by h, are Du and $-\alpha Du$. The bulk salt concentration c_0 is chosen to ensure that the Debye length, $\lambda_{\mathrm{D}} \approx 0.3(\mathrm{nm})/\sqrt{c_0(\mathrm{mol/L})}$, is smaller than h (typically $\lambda_D = h/10$), while the Dukhin length $\ell_{\mathrm{Du}} = |\Sigma|/c_0 e$ is taken to be larger than h, ensuring a surface governed transport. An invariance is assumed along the y axis. The values of Δn and $\Delta\phi$ are imposed, the unknowns are the values of the salt concentration and the electrical potential at both entrances of the channel (n_L^0, n_R^0, ϕ_L^0, ϕ_R^0), and at each side of the central discontinuity of the diode

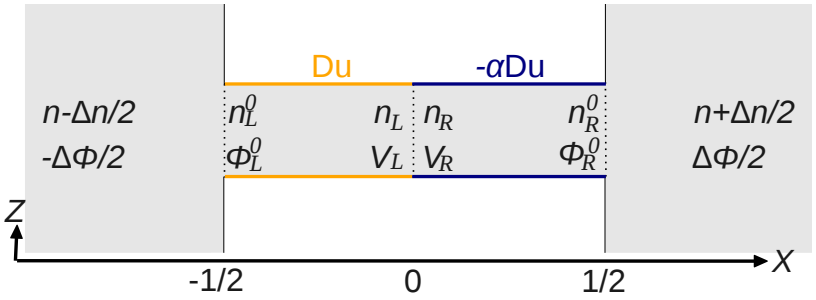

FIGURE 4.10: System and notations used in the analytical model. $n = c/c_0$, $\phi = V \times e/k_BT$ and $X = x/L$.

$(n_L, n_R, \phi_L, \phi_R)$, see figure 4.10.

Governing equations – Following Dydek et al. [137], we have chosen to average the Nernst-Planck equations for the ion densities over the cross-section of the channel. This approximation is expected to be valid for $h \ll L$. Hence a 1D geometry is assumed for the resolution of the transport equation. One defines accordingly area averaged quantities, such as the mean ion concentrations and the mean electrical potential

$$\langle n_\pm \rangle = \frac{2}{H} \int_0^{H/2} n_\pm(x,z)\, \mathrm{d}z, \tag{4.16}$$

$$\langle \phi \rangle = \frac{2}{H} \int_0^{H/2} \phi(x,z)\, \mathrm{d}z. \tag{4.17}$$

In the following we will write $n_\pm \equiv \langle n_\pm \rangle$ and $\phi \equiv \langle \phi \rangle$ to simplify the notations. We then write a PNP equation for the averaged quantities

$$j_\pm = -\nabla n_\pm \mp n_\pm \nabla \phi, \tag{4.18}$$

where $j_\pm$ are respectively the positive and negative normalized ions fluxes $j_\pm = J_\pm L/Dc_0$. Note that the averaged fluxes are independent of y, which means that $\nabla \equiv \dfrac{\mathrm{d}}{\mathrm{d}x}$. Hence, one can define the total ions fluxes $j = j_+ + j_-$ and the ionic current $i = j_+ - j_-$, and one gets from equation (4.18) the following transport equation

$$j = -\nabla n - (n_+ - n_-)\nabla \phi,$$
$$i = -n \nabla \phi.$$

Note that we assumed here the validity of the decoupling $\langle n_\pm \nabla\phi\rangle \simeq \langle n_\pm\rangle \langle\nabla\phi\rangle$. These equations are completed with the charge neutrality, which takes the form:

$$\begin{aligned} n_+ - n_- &= -2Du \quad \text{for } -1/2 < X < 0, \\ n_+ - n_- &= 2\alpha Du \quad \text{for } 0 < X < 1/2, \end{aligned}$$

where we used normalized dimension $X = x/L$.

Boundary conditions – Let us first compute the average charge in the context of the PB (non-linear) model. For a semi-infinite geometry with surface charge $-\Sigma < 0$, the solution of the PB equation for the potential can be written as [46]:

$$\phi(z) = \phi_0 - 2\log\left[\frac{1+\gamma e^{-z/\lambda_D}}{1-\gamma e^{-z/\lambda_D}}\right] \tag{4.19}$$

with ϕ_0 the potential far from the wall, $\gamma = +\gamma_0$ the positive root of the equation $\gamma^2 + 2\frac{\ell_{GC}}{\lambda_D} - 1 = 0$, with $\ell_{GC} = 1/(2\pi|\Sigma|\ell_B)$ the Gouy-Chapmann length: $\gamma_0 \equiv -\frac{\ell_{GC}}{\lambda_D} + \sqrt{1 + (\frac{\ell_{GC}}{\lambda_D})^2}$. For a positive surface charge $+\Sigma$, the solution for V is identical, though with $\gamma = -\gamma_0$ (< 0). Altogether, one may write $\gamma_\mp = \pm\gamma_0$ with γ_0 given above (> 0). The ions profiles are accordingly $n_\pm = n_0 \exp[\mp(\phi - \phi_0)]$ and the averaged density is calculated as

$$\langle n_\pm\rangle = n_0 + 2\frac{n_0}{h}\int_0^\infty \left[\left(\frac{1+\gamma e^{-z/\lambda_D}}{1-\gamma e^{-z/\lambda_D}}\right)^2 - 1\right] \mathrm{d}z, \tag{4.20}$$

which leads after straightforward calculations to

$$\langle n_\pm\rangle = n_0 \pm (1 \pm \gamma_0)\frac{|\Sigma|}{h} \tag{4.21}$$

for a negatively charged surface and

$$\langle n_\pm\rangle = n_0 \mp (1 \mp \gamma_0)\frac{|\Sigma|}{h} \tag{4.22}$$

for a positively charged surface. Note that $\gamma_0 \to 0$ for a weakly charged surface $\Sigma \to 0$ and $\gamma_0 \to 1$ for a strongly charged surface. The relation

between $n_L = n_{L,+} + n_{L,-}$ and $n_R = n_{R,+} + n_{R,-}$ can be written as

$$n_L - n_R = -2Du(\gamma_L + \alpha\gamma_R) \tag{4.23}$$

with $\gamma_L = -\gamma_0(\Sigma)$ and $\gamma_R = \gamma_0(\alpha\Sigma)$. The conditions for the concentration at each entrance can be written as

$$n_L^0 = 2 - 2Du\,\gamma_L - \Delta n \tag{4.24}$$

$$n_R^0 = 2 + 2Du\,\alpha\gamma_R + \Delta n \tag{4.25}$$

Following the same steps as previously (see appendix A), we found four supplementary equations:

$$n^L - n_0^L = 2Du\frac{i}{j}\log\left(\frac{n_L + 2Du \times i/j}{n_L^0 + 2Du \times i/j}\right) - \frac{j}{2}, \tag{4.26}$$

$$n_R - n_0^R = 2\alpha Du\frac{i}{j}\log\left(\frac{n_R^0 - 2\alpha Du \times i/j}{n_R - 2\alpha Du \times i/j}\right) + \frac{j}{2}, \tag{4.27}$$

$$\phi^L - \phi_0^L = \frac{i}{j}\log\left(\frac{n_L + 2Du \times i/j}{n_L^0 + 2Du \times i/j}\right), \tag{4.28}$$

$$\phi^R - \phi_0^R = \frac{i}{j}\log\left(\frac{n_R - 2\alpha Du \times i/j}{n_R^0 - 2\alpha Du \times i/j}\right). \tag{4.29}$$

Those last four equations and equation (4.23) form a set of 5 equations for 6 unknowns; i, j, n_L, n_R, ϕ^L and ϕ^R. A last equation is obtained by extrapolating the definition of the Donan potential, classically used in a full EDLs overlap configuration. This is a common assumption in colloidal science where the expression of a Donnan potential is used even in case of non overlap of electrical double layer. This extrapolation can be written as

$$\phi = \frac{1}{2}\log\left(\frac{n_-}{n_+}\right) + \phi_{\text{axis}}, \tag{4.30}$$

with ϕ_{axis} the local potential along the axis of the diode. ϕ_{axis} is expected to decrease linearly from $\Delta\phi/2$ to $-\Delta\phi/2$, as a first approximation. Doing that, we suppose that we can use the Donnan potential in a situation without EDLs overlap. This will be confirmed hereafter using finite element calculations. Altogether, this leads to the following expression for the potential gap at the centre of the diode:

$$\phi_L - \phi_R = \frac{1}{2}\log\left(\frac{n_L + 2Du}{n_L - 2Du}\right) - \frac{1}{2}\log\left(\frac{n_R - 2\alpha Du}{n_R + 2\alpha Du}\right). \tag{4.31}$$

Summary – Equations (4.23), (4.29), (4.29), (4.28) ,(4.27) and (4.31) constitute a set of 6 equations with 6 unknowns and can be solved numerically. The first strong hypothesis we made was to assume the validity of a 1-D model while the system is clearly multidimensional, with potential and concentration profiles varying in two or more dimensions. The second strong hypothesis was to assume the validity of a Donnan like equation $\phi \sim \log(n_-/n_+)/2$ for averaged quantities in the absence of electrical double layer overlap. To check the validity of the present model, we performed finite element calculations, whose results are presented hereafter.

4.3.4 Comparison between model and finite element calculations

We used the software Comsol multiphysics to perform finite element calculations. A complete set of equations (Stokes, diffusion-convection and Maxwell) in a 2D axi-symmetric geometry is solved with the proper boundary conditions. Details are presented hereafter.

System – We used a system similar to the representation in figure 4.11. A membrane pierced with a nanochannel separates two reservoirs of respective salt concentrations $c - \Delta c/2$ and $c + \Delta c/2$. The nanochannel is taken to be cylindrical with a radius $a = 50\,\text{nm}$ and a length $L = 1\ \mu\text{m}$. Half of the channel is charged with a surface charge Σ, and the other half with a surface charge $-\alpha\Sigma$, with $\alpha = 2$ and $\Sigma = 4\,\text{mC/m}^2$. c_0 is taken to be 1 mmol/L, which gives a Debye length $\lambda_D \approx 10\,\text{nm} \approx a/5$ and a Dukhin length $\ell_{\text{Du}} \approx 40/80\,\text{nm} \approx a$, ensuring strong enough surface effects. We make sure the characteristic size of both reservoirs R_{res} is always bigger than l_{Du}, λ_D and a in order to avoid finite size effects.

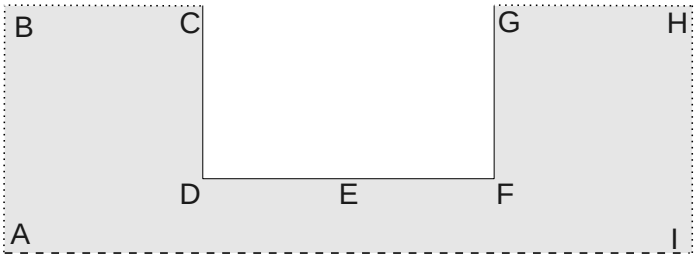

FIGURE 4.11: System used for finite element calculations, see text for the description.

Hydrodynamics – We solve the Stokes equation

$$\eta\vec{\nabla}^2 u = \vec{\nabla}p - \vec{F}_{\text{elec}}, \tag{4.32}$$

where $\vec{u}$ is the water velocity field, p the pressure field, $\vec{F}_{\text{elec}}$ an electric volume force equal to

$$\vec{F}_{\text{elec}} = -F(c_+ - c_-) \times \vec{\nabla}V, \tag{4.33}$$

with F the Faraday constant, $c_\pm$ the concentration in $\pm$ species and V the electrical potential. The flow is taken to be incompressible $\vec{\nabla}.\vec{u} = 0$. Atmospheric pressure p_{atm} is imposed along A-B-C and G-H-I (see figure 4.11). The no slip boundary condition is imposed along walls C-D-E-F-G. An axial symmetry is imposed along A-I.

Electrostatics – We solve the Maxwell-Gauss equation

$$\vec{\nabla}.\vec{D} = \rho, \tag{4.34}$$

together with a constitutive relation relating the electric displacement $\vec{D}$ with the electric field $\vec{E}$:

$$\vec{D} = \epsilon_0\epsilon_r\vec{E}. \tag{4.35}$$

ϵ_r is the dimensionless relative permittivity, and ϵ_0 the vacuum permittivity and ρ the space charge density: $\rho = F(c_+ - c_-)$. The relationship between electric potential V and the electric field $\vec{E}$ is

$$\vec{E} = -\vec{\nabla}V. \tag{4.36}$$

A surface charge Σ is applied along D-E, as well as a surface charge $-\alpha\Sigma$ along E-F (see figure 4.11). The no charge boundary condition is set on C-D and F-G. The electrical potential $-\Delta V/2$ is applied along A-B-C, and $\Delta V/2$ along G-H-I. Axial symmetry was imposed along A-G.

Transport of diluted species – We solve the Nernst-Planck equations

$$\vec{\nabla}.\left(-D\vec{\nabla}c_\pm - \mu c_\pm\vec{\nabla}V\right) = 0 \tag{4.37}$$

and

$$\vec{N}_{\pm} = -D\vec{\nabla}c_{\pm} - \mu c_{\pm}\vec{\nabla}V. \tag{4.38}$$

The no flux boundary condition was imposed along C-D-E-F-G (see figure 4.11). The concentration $c - \Delta c/2$ was imposed for both species along A-B-C, while $c + \Delta c/2$ was imposed along G-H-I. Axial symmetry was imposed along A-I.

Results – First, let us test an important hypothesis of the theoretical model, the validity of a Donnan-like equation in the absence of EDL overlap which can be written as

$$\phi = \ln\left(\frac{n_-}{n_+}\right) + \phi_{\text{axis}}, \tag{4.39}$$

with $\phi = V \times e/k_BT$ and $n_{\pm} = c_{\pm}/c_0$ the values of the (normalized) potential and concentrations averaged over the channel section. To test the validity of equation 4.39, we extract the four quantities ϕ, n_-, n_+ and ϕ_{axis} from finite element calculations. Then, we compare "ϕ" and "$\log(n_-/n_+)/2 + \phi_{\text{axis}}$" for different values of the external voltage drop $\Delta\phi = \Delta V \times e/k_BT$ (-4, 0, and 4). As seen in figure 4.12, the two quantities are found to be in a quite good agreement. This confirms that, despite the absence of electric double layer overlap, a Donnan-like equation gives meaningful results. Hence averaged potential and concentration are linked by a quite simple expression (see equation (4.39)) even in absence of an electrical double layer overlap.

Then, using the very same parameters in both FE calculations and PNP model, we make a comparison of their respective results for i_e, j_i and Q in several configurations, defined by the imposed values of Δn and $\Delta\phi$ ($\Delta n = 0$, $\Delta\phi \neq 0$), ($\Delta n \neq 0$, $\Delta\phi = 0$). The surface charge was taken to be $\Sigma = 4\,\text{mC/m}^2$ and $\alpha = 2$, the bulk concentration was $c_0 = 1\,\text{mmol/L}$ and the channel had a radius $a = 50\,\text{nm}$ and a length $L = 1\,\mu\text{m}$. We plotted in figure 4.13 and 4.14 the (normalized) ionic flux $j_i = J_i \times L/Dc_0$ and ionic current $i_e = I_e \times L/Dc_0e$ as a function of $\Delta\phi$ and Δn. The agreement between the PNP model and FE calculations is very good. From the model, one can also deduce the osmotic pressure $\Delta\Pi$ using the formula

$$\Delta\Pi = c_0 k_B T \left(2\Delta n - j\right), \tag{4.40}$$

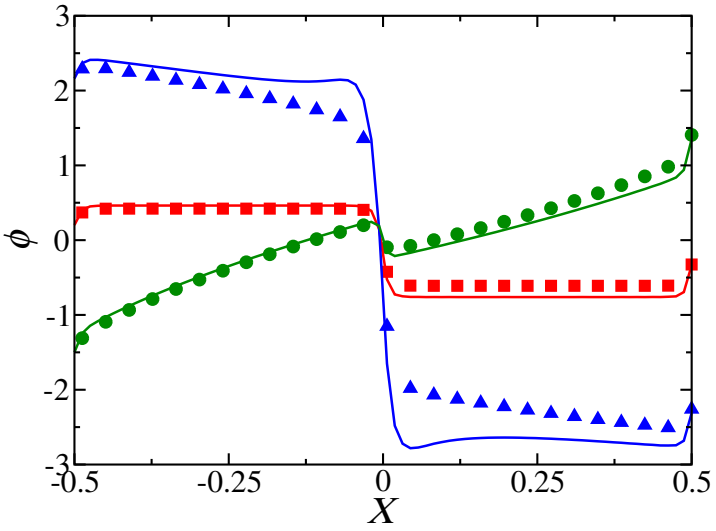

FIGURE 4.12: Comparison between the averaged potential over the cross section $\phi = V \times e/k_BT$ (symbols) and formula $\ln(n_-/n_+) + \phi_{\text{axis}}$ with $n_\pm = c_\pm/c_0$ along the axis $X = x/L$ of the diode. $\Delta n = \Delta P = 0$ and $\Delta\phi$ = -4 (blue), 0 (red) and 4 (green).

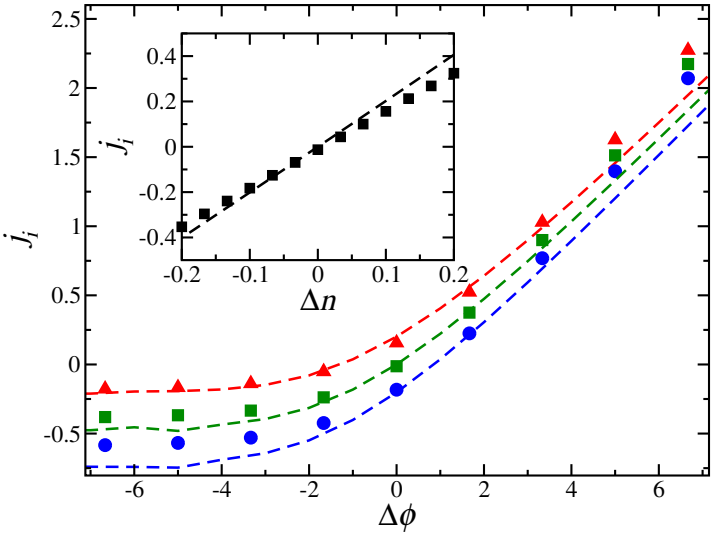

FIGURE 4.13: Main: normalized total flux $j_i = j_+ + j_- = J_i \times L/Dc_0$ as a function of the voltage drop $\Delta\phi = \Delta V \times e/k_BT$. Model: dashed lines, finite element calculations: symbols. Blue circles: $\Delta n = \Delta c/c_0 = 0.1$, green squares: $\Delta n = 0$ and red triangles: Δn = -0.1. Inset: j_i as a function of the normalized concentration difference Δn for $\Delta\phi = 0$.

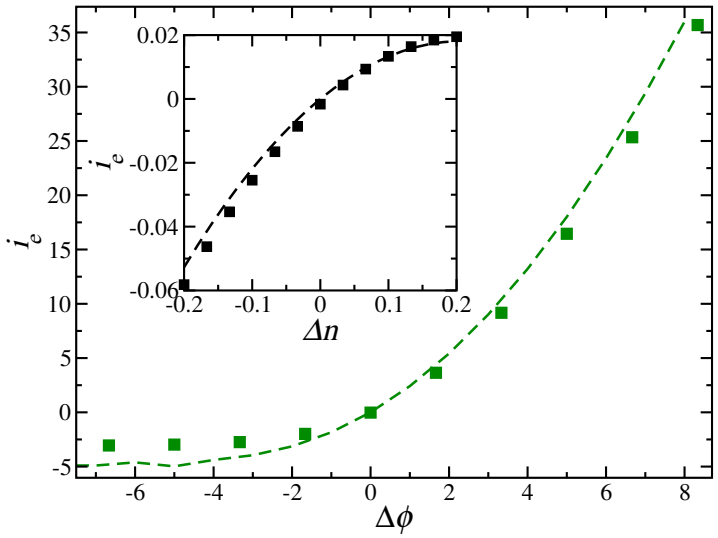

FIGURE 4.14: Main: normalized ionic current $i_e = j_+ - j_- = I_e \times L/Dce$ as a function of the normalized voltage drop $\Delta\phi = \Delta V \times e/k_BT$ for $\Delta n = 0$. Model: dashed line, finite element calculations: symbols. Inset: normalized ionic current $i = j_+ - j_-$ as a function of the normalized concentration difference $\Delta n = \Delta c/c_0$ for $\Delta\phi = 0$.

where the factor 2 accounts for the two species. The water flux Q is expected to be proportional to $\Delta P - \Delta\Pi$:

$$Q = -K(\Delta P - \Delta\Pi) \tag{4.41}$$

with K the hydrodynamic permeability of the channel, and ΔP the hydrodynamic pressure difference, taken to be 0 in this study. We plotted in figure 4.15 a comparison between the measured water flow Q from finite element calculations and the predicted water flow estimated from equation (4.41). The water flow deduced from the theoretical model has been adjusted to fit the finite element results through the permeability K. We used an effective permeability $K^{\text{eff}} = 0.4 \times K^{\text{th}}$ where

$$K^{\text{th}} = \left[\frac{3\eta}{a^3} + \frac{8\eta L}{\pi a^4}\right]^{-1} \tag{4.42}$$

with L=1 µm and a=50 nm, $\eta = 1$ mPa.s, $C = 3$ (cylinder without smooth entrances and with the no slip boundary condition, see chapter 2), which gives $K^{\text{th}} \approx 2.3 \cdot 10^{-21}$ m^3/Pa.s. The fact that the effective permeability of the nanodiode is lower than the predicted one can be explained by the strong internal pressure gradients present at the transition between the left and right parts of the diode. Those internal pressure gradients, which ensure a

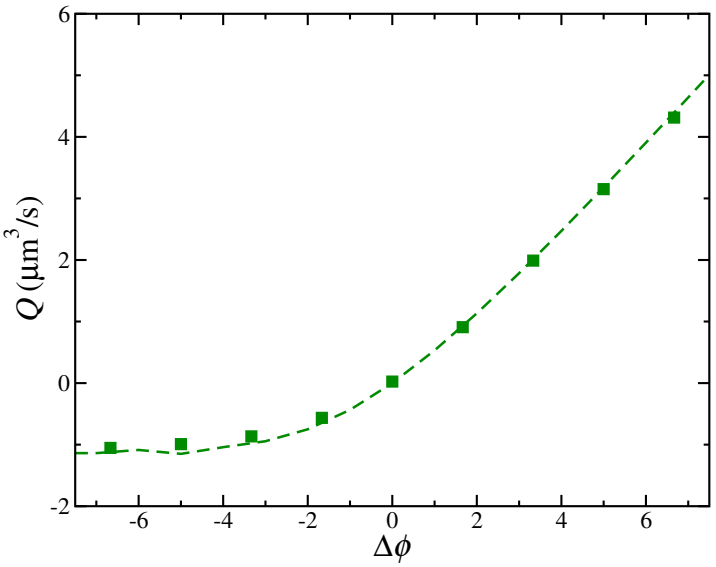

FIGURE 4.15: Water flow Q as a function of the normalized voltage drop $\Delta\phi = \Delta V \times e/k_BT$ for $\Delta n = 0$. Symbols: finite element calculations. Dashed line: theoretical model with an hydrodynamic permeability K^{eff}.

homogeneous water flow along the axis of the diode x, lead to supplementary velocity gradients, hence to a supplementary viscous dissipation. However, the agreement between finite element calculation and the present theoretical model is excellent, using the permeability as an adjustable parameter.

Summary – The PNP model was found to give a quite good agreement with finite element results for the prediction of flux values, such as the ionic current I_e, the total ionic flux J_i or even the water flow Q. This confirms the validity of the various assumptions we made in the building of the model. It justifies the use of a PNP equation with averaged values of n and ϕ over the channel cross-section. It justifies also the use of a Donnan like equation $V \sim \log(n_-/n_+)/2 + V_{\text{axis}}$ despite the absence of an electric double layer overlap.

4.3.5 Discussion

Summary – We showed that it is possible to induce a rectification of the ionic current or the water flow in nanofluidic diodes in the absence of electric double layer overlap. First, molecular dynamics simulations of ionic species in an implicit solvent unveiled the existence of diode-like effects in a

channel whose radius was equal to ten times the Debye length. This effect is governed by surface effects. Then, a theoretical model based on PNP equations was found to compare well with numerical calculations. Despite the multi-dimensionality of the problem, an unidimensional model was found to give very accurate predictions for the flow values through the nanodiode.

Consequences – According to the present work, the condition for diode-like effects to occur, is a surface conduction dominating over the bulk one, which can be achieved with a large surface charge density (or a small salt concentration). This constraint is less restrictive than the electrical double layer overlap, and can be obtained for both realistic salt concentrations and realistic nanochannel dimensions. For example, in the case of sea water ($c_0 \sim 0.6\,\mathrm{M}$), the Dukhin number is equal to one (and the current rectification is expected) in channel of diameter 1 nm and a surface charge $|\Sigma| \sim 50\,\mathrm{mC/m^2}$. In the case of a salt concentration of $c_0 \sim 1\,\mathrm{nM}$ and a surface charge of $50\,\mathrm{mC/m^2}$, a Dukhin number equal to one is obtained for a channel diameter equal to 1 µm. Then, it should be possible to exploit the nanofluidic diode properties with sub-microfluidic devices, or high salt concentration.

Applications – Controlling flow using nanofluidic diodes in the limit of non-overlapping double layers could be of great interest when dealing with sea water with high salt concentration. Indeed, in this case, the Debye length is around 3 Å, and working in a, electrical double layer overlap regime represents a real technological challenge. Our results suggest that nanofluidic diode properties could be used despite the absence of an overlap between double layers. Then, the ability of nanofluidic diodes to rectify and control the flux could be used as a first filtration step in a desalination process.

4.4 General conclusion

In this chapter, it has been shown both theoretically and numerically that a nanofluidic diode can be used to rectify water flow. This effect is based on the nonlinear coupling between the water flow and the ion dynamics.

Moreover, it has been shown that a rectification exists even without any electrical double layer overlap, in the so called Dukhin regime.

These results still need to be confirmed experimentally (at the laboratory scale first). The major difficulty lies in the water flow detection, which remains a technological challenge since the magnitude of the flow through a single nanochannel is by nature extremely small ($Q \sim 10^{-18}\,\mathrm{m}^3/\mathrm{s}$), as evoked in the chapter 1.

If experimentally confirmed, the effect discussed in this chapter may lead to some interesting industrial applications, particularly in water purification and desalination. Indeed, here we propose to manipulate the solvent flow by imposing the electrical potential rather than the pressure, which is the case for the classical Reverse Osmosis (RO). This allows to use electrodes rather than pumps for flow manipulation, and may present some technological advantages. Moreover, the possibility of controlling flow using a nanodiode with no electrical double layer overlap would be an interesting first step toward the improvement of desalination technique. Indeed, the treatment of high salt concentration (~ 0.6 M) solutions would not require the use of subnanometric nanochannels, whose fabrication is still a huge challenge.

Chapter 5

$1/f$ noise in ionic transport across solid state nanopores

Contents

This chapter is based on the following publication:

- Simon Gravelle, Roland R. Netz, Lydéric Bocquet, Adsorption Kinetics in Open Nanopores as a Source of Low-Frequency Noise, *Nano letters*, 2019 [148].

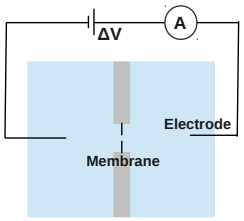

A

Abstract and main results – Ionic current measurement through a single nanopore or an array of nanopores is a widely used method for membrane characterization (see figure A). It was first developed by physiologists for characterizing the ion transport through biological membranes, before it was used with pierced solid state membranes as well. Despite the apparent differences between all the considered systems/membranes, extracted data seem to share one common point: at low frequencies the Power Spectral Density (PSD) of the ionic current decreases with the frequency f as $1/f^{\alpha}$, with $\alpha \sim 1$ (see figure B). This $1/f^{\alpha}$ signature is called pink noise and has been widely observed, in both natural and man-made processes. Its origin and its apparent universality are still an important mystery of modern physics.

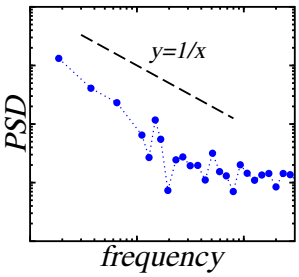

B

In this study, we focus on the presence of pink noise in ionic current measurement through nanopores, whose origin remained unexplained. We presumed that reversible adsorptions of ions on the pore surface is at the origin of the measured pink noise. To test this hypothesis, we performed molecular dynamics simulations in a system made of a solid membrane in contact with diffusing particles that can reversibly adsorb on the pore's walls (see figure C). We found that this simple system leads to the generation of pink noise in the number of free carrier inside the pore. This hypothesis is corroborated by an analytical model based on first return trajectories calculation between reversible adsorption of ionic species on a solid surface. Altogether, our results propose a serious candidate to explain the origin of the widely observed $1/f$ fluctuations in ionic current measurements.

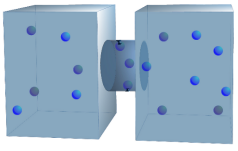

C

5.1 Introduction

The present chapter is inspired by experimental studies reporting the presence of pink noise in the power spectral density of the ionic current measured through nanoporous membranes. Understanding the origin of this ubiquitous phenomena is the main motivation of this study. In order to introduce this subject, we will start with some generalities about coloured noises, with a brief overview of their current understanding. Then, a description of the typical experiment of ionic current measurement through nanoporous membranes is given, as well as a description of how $1/f$ noise is observed and what the basic features are. Then a brief overview of the experiments that have reported $1/f$ noise from ionic current is presented, with some words about the current state of the theory. To end up the introduction, the main idea behind the present study is detailed.

5.1.1 Coloured noises

In this study we will distinguish between three types of noise: white noise, pink noise and Brown (red) noise. The presence of a coloured noise in a signal can be detected by calculating its Power Spectral Density (PSD). The PSD describes how the power of a signal is distributed over the different frequencies f. It is defined as the square modulus of the Fourier transform of the considered signal, divided by the integration time (the duration of the signal). Coloured noises correspond to power-law noises, i.e. to a signal for which the PSD is proportional to $1/f^{\alpha}$. Notice that power law, and therefore PSD are usually plotted in log-log coordinates because $\log(\mathrm{PSD}(f)) = -\log(\mathrm{cst}/f^{\alpha}) = -\alpha\log(f) + \log(\mathrm{cst})$, so the PSD appears as a straight line with a slope α, which eases the identification of the power law as well as the measurement of α.

The case α=0 corresponds to white noise, a signal with a constant PSD over frequencies. It is the signature of an uncorrelated process with time. The case $\alpha = 2$ corresponds to random walk noise or Brown noise (after Robert Brown), and is generated for example by Brownian motion. The PSD of such a signal is inversely proportional to the square of the frequency: $\mathrm{PSD} \propto f^{-2}$. It is the signature of a random walk, i.e. of a process with no

correlation between increments [149]. The intermediate case between white noise and Brown noise is called pink noise, and refers to any noise with a PSD of the form:

$$\mathrm{PSD}(f) \propto \frac{1}{f^{\alpha}}, \text{with } 0 < \alpha < 2. \tag{5.1}$$

While the origins of both white and Brown noises are considered to be well understood, pink noise remains an important mystery of modern physic. Sometimes referred to as originating from a long-memory process with long-term correlations, pink noise is widely found in nature, in both natural and man-made processes. From its first observation by Johnson in 1925 [150] in data from an experiment designed to test Schottky's theory of shot noise in vacuum tubes, it has been reported in a wide range of domains such as condensed matter, electronics, biology, astrophysics, geophysics, economy, psychology, language and even music [149, 151, 152].

The diversity of systems which contain $1/f$ fluctuations, from traffic flow to electrical resistors, indicates that the physical origin of the noise is certainly not universal [153]. Still, the ubiquity of pink noise suggests that a generic *mathematical* explanation may exist, but there is no simple equation generating signals with $1/f$ noise. Furthermore, in most cases the observed $1/f$ noises have been explained by ad hoc models [151]. Accordingly, in the present study, we did not try to adapt an existing model of pink noise to the specific case of ionic current through nanopores, but rather tried to identify the source of 1/f fluctuations in this particular situation.

Note that a PSD cannot be a true power law. Indeed, a signal with a PSD in $1/f^{\alpha}$ presents a total power equal to

$$\int_0^{\infty} f^{-\alpha} df = \infty, \ \forall \alpha, \tag{5.2}$$

which is obviously physically irrelevant. So when thinking about a coloured noise, one has to keep in mind that it can only appear on a limited range of frequencies. Therefore, rolloffs should exist, with $\alpha \leq 0$ at low frequencies, and $\alpha > 0$ at high frequencies, ensuring a finite value for the total power of the signal. In practice, there will also be cut-offs so the measured coloured noises will always be limited to a certain range of frequencies.

5.1.2 Basic experiment and state-of-the-art

The basic idea behind each experiment at the origin of the present study is the following. A membrane pierced with a nanopore separates two reservoirs containing an electrolyte. A voltage drop ΔV is applied far from the membrane using electrodes, and the ionic current I_e that passes through the nanopore is recorded as a function of the time (see figure 5.1). Note that, for the sake of simplicity, one considers only membranes pierced with a single pore, but *a priori* our study can be expanded to membranes pierced with an array of pores or even to a porous medium. The theoretical ionic

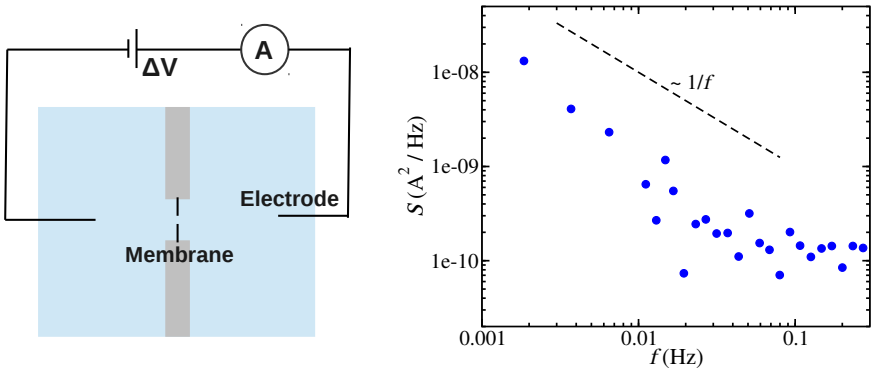

FIGURE 5.1: Left: schematic of an experimental system. Right: typical power spectral density (S) of the ionic current through a single solid state nanopore. Courtnesy of E. Tamborini.

current can be written as $I_e(t) = G(t)\Delta V$, where $G(t)$ is the conductance of the pore. For some reasons, that will be discussed below, the measured ionic current fluctuates around its average value. The Power Spectral Density (PSD), which contains information about how a signal fluctuates, can be calculated for the ionic current. For illustration, a typical PSD obtained from ionic current measurement across a solid state nanopore is shown in figure 5.1 [1]. At low frequencies, the PSD decreases with the frequency as $\sim 1/f$.

A power spectral density that scales as $1/f$ at low frequency is a very common result when measuring ionic current through nanopore. Indeed, during the last decades, $1/f$ signatures in ionic current have been reported for a large variety of fabricated nanopores [21, 154–160]. This pink noise appears to be very robust, and has been observed with various nanopore

[1] data shared by E. Tamborini

geometries, such as conical, hourglass or cylindrical. Moreover, various materials have been used for the membrane fabrication, such as silicon nitrid, glass, polymer or nanopores with atomic layer deposition of Al_2O_3 or covered by SiO_2. Finally, while most measurements have been performed with a solution of water containing K-Cl salt, Tasserit et al. also used ionic liquid and found, again, a robust $1/f$ signal [155]. As a side remark, note that ionic current measurements have also been performed in order to characterize organic membranes. For example, the study of alpha Hemolysin [154], open bacterial porin channel [161] or open maltoporin channel [162] have led to the presence of pink noise in the power spectral density, similarly to observations made with fabricated membranes.

Various reasons have been invoked by authors to explain the presence of pink noise, such as cooperative motion of ions or fluctuations of ions concentration related to surface charge of the pore. However, no one has converged toward a convincing model. Notice that the case of biological membranes is maybe more complex that artificial one, and the presence of pink noise is sometimes attributed to channel conductance fluctuations due to opened-closed transitions, or channel breathing. For these reasons and for the sake of simplicity, we do not focus on biological membrane in this study. But even if one considers fabricated membranes only, the wide range of systems with various geometries or surface chemistries concerned by this so-called pink noise suggests the ubiquity and the robustness of the phenomenon.

Most of the time, authors modelled the low frequency noise with the Hooge's phenomenological relation for low-frequency pink noise [163]:

$$S(f) = \gamma \frac{I_e^{2+\beta}}{N_c f^{\alpha}} \tag{5.3}$$

where S_I is the power spectral density of the ionic current I_e, f the frequency, γ the Hooge parameter which quantifies the amount of low-frequency noise and N_c the number of charge carriers. Notice that γ is dimensionless if $\alpha = 1$ and $\beta = 0$ only. Based on the dependence of γ with the pH, authors usually suggest that the noise originates from surface charge fluctuations. But the Hooge's relation is only phenomenological, and brings no clear explanation on the origin of the reported pink noise. Some theoretical studies report

a possible link between the diffusion of ions in nanopores and the $1/f^{\alpha}$ spectrum, but these studies did not converge towards an elegant and general solution [164–166].

5.1.3 General idea

As stated above, pink noise is a widely observed phenomenon in physics. Since no general equation satisfactorily describes its origin, specific models have been built in each situation. Thus, the objective of the present chapter is to understand and describe the origin of pink noise in the particular case of ionic current measurement through a nanopore. Inspired by some experimental measurements [155], in which a strong dependency of the power spectral density with the pH of the solution have been reported, we explored a possible link between ion adsorption on the membrane's surface and pink noise. The main idea behind the present study is presented hereafter.

Consider a solid membrane pierced with a nanopore, in contact with an ionic solution. Due to protonation/deprotonation reactions of ions occuring on the nanopore's surface, the nanopore exhibits a fluctuating surface charge $\Sigma(t) = \Sigma_0 + \delta\Sigma(t)$, with $\Sigma_0 = \langle\Sigma\rangle_t$ the temporal average of $\Sigma(t)$. For example, a protonation reaction

$$\mathrm{SH} + \mathrm{H_2O} \leftrightarrow \mathrm{S^-} + \mathrm{H_3O^+}, \tag{5.4}$$

where S stands for surface, leads to a change of the surface charge $\Sigma(t)$. Accordingly, this fluctuating surface charge leads to fluctuations in the pore conductance $G(t)$. We made the hypothesis that fluctuations that are due to reversible adsorptions are low-frequency, and contain long-term correlations. This hypothesis will be discussed in the next paragraph, and justified all over this chapter. Hence the ionic current can be written as the (independent) sum of a low frequency varying term $G(t)$, and a high-frequency noise term $\delta I(t)$ which is a classical white noise such as a thermal noise [167] $I(t) = G(t)\Delta V + \delta I(t)$.

If one admits that reversible adsorption of ions on the surface leads to pink noise, which will be shown below, one may wonder why such a simple process

generates this pink noise. In other words, since pink noise is associated with a long-term memory process, what physical variable or process contains this memory? An element of answer is that, to generate pink noise, the considered event must be distributed in time as a power law $1/t^{\gamma}$. It happens to be the case of the probability distributions of times associated with diffusion, that are usually proportional to $1/t^{\gamma}$, where γ is related to the physical dimension of the problem. This is a key point of the present work, which is going to be illustrated all along this study. Accordingly, the trajectories of ions between two adsorptions, called first return processes and controlled by diffusion, will be at the centre of our attention.

5.1.4 Outline of the study

The goal of the present study is to understand and describe the pink noise commonly observed when measuring ionic current through nanopores. To do so, we first focused on the case of an infinite cylinder with an adsorbing surface. Using molecular dynamics simulations, we found that fluctuations of the number of particles inside the pore presents pink noise in a limited range of frequencies. This result confirms our primary hypothesis that diffusion combined to reversible adsorption can generate pink noise, and is the first important result of the present study. Then a theoretical model describing the trajectories of the particles in the same geometry is presented, and appears to be in really good agreement with simulations.

Our results show that this phenomenon is limited to large frequencies only. This is due to the geometrical confinement imposed to the particles inside an infinite cylinder, which does not allow very long trajectories. To overcome this limitation, the study was extended to a more realistic case: a finite-sized cylindrical nanopore with an adsorbing surface connected to large reservoirs containing diffusing particles. Molecular dynamics simulations shows the existence of pink noise in a larger range of frequencies in this case. The lower frequency at which pink noise appears is limited by the time spent by a particle inside the nanopore. Hence in the case of long nanochannels or realistic surface energy adsorption, the pink noise is expected to be observable down to the Hertz, which is in good agreement with experiments. This indicates that diffusion combined to adsorption is a serious candidate

explaining the presence of pink noise at low frequencies measured in ionic currents. Finally, a theory describing particles diffusing in a large reservoir and adsorbing on the surface of a structure (taking to be a sphere by simplicity) is presented and confirms our main message.

5.2 Noise in an infinite nanotube

The first considered system was an infinite cylinder of radius a with an adsorbing surface, as shown in figure 5.2. Inside the cylinder, a number N of particles alternate diffusion and adsorption. We focused on the temporal fluctuations of the number of free particles $\delta N_f(t) = N_f(t) - \langle N_f(t) \rangle_t$, with $N_f(t)$ the number of free particles at a time and $\langle . \rangle_t$ a temporal average. Note that the number of free particles is closely related to the number of bonded (adsorbed) particles: $N_f(t) = N - N_b(t)$.

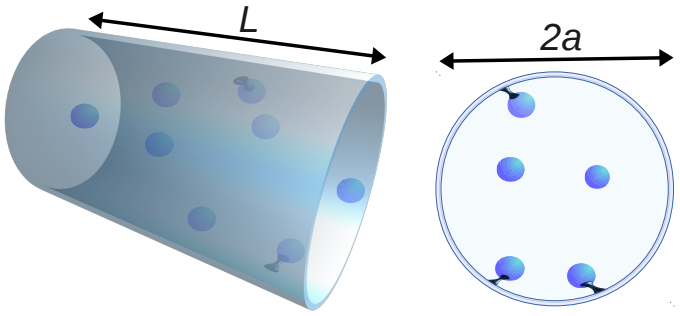

FIGURE 5.2: Scheme of the system of interest, a cylinder of radius a and length L contain diffusing particles. Particles can be reversibly trapped on the surface of the cylinder.

To begin our study, we used molecular dynamics simulations in order to highlight the existence of pink noise in the power spectral density of the number of free particle inside the cylinder. Moreover, these simulations allowed to easily explore the impact of various parameters, such as the tube radius or the surface trap density on the PSD. Then, an analytical calculation of power spectral density of diffusing species inside an infinite tube was made to confirm the link between diffusion, adsorption and pink noise.

5.2.1 Molecular dynamics simulations

Method – Molecular dynamics simulations where performed with LAMMPS [82]. The system was made of a solid cylinder with radius a ($\sim$ 20 to 100 Å) in contact with a liquid, as shown in figure 5.2. The length of the cylinder was chosen $L \sim 2a$, with no impact on the results due to the periodic boundary condition along the axis of the tube. The solid surface was made of a combination of fixed atoms (acting as traps) and a solid flat wall that interacts with the liquid by generating a force on the atom in a direction perpendicular to the wall. The liquid was made of a number N of particles diffusing in an implicit solvent. The time-step was taken to be 2 fs. A Langevin thermostat (temperature 300 K) was applied on the moving particles and represents the interactions with a background implicit solvent. From mean square displacement measurements, the value of the diffusion coefficient of ions was found to be: $D = 1.8 \times 10^{-8}\,\mathrm{m}^2/\mathrm{s}$. The diffusion coefficient depends, among other, on the "damping" parameter of the Langevin thermostat, taken to be equal to $\tau_{\mathrm{damp}} = 330$ fs. Notice that particles have ballistic trajectories for $t < \tau_{\mathrm{damp}}$, and diffusing trajectories for $t > \tau_{\mathrm{damp}}$. This high value of D, i.e. one order of magnitude larger than typical diffusion coefficient for microions, was chosen on purpose, with the aim of exploring a larger range of configurations in a given simulation time. We made sure that the physics remains unchanged when using a realistic diffusion coefficient. The equations of motion were integrated using the velocity Verlet algorithm [168]. Particles interact with each other as well as with wall's atoms via a Lennard-Jones potential with depth $\epsilon = 0.3$ Kcal/mole and equilibrium distance $\sigma = 3$ Å. The cut-off for the Lennard-Jones is taken to be $r_c = \sigma \times 2^{1/6}$ and corresponds to the minimum of the Lennard-Jones potential. This potential, which keeps only the repulsive part of the Lennard-Jones potential, is called WCA [169]. The process of reversible adsorption of particles was introduced by the presence of fixed traps located on pore surface. A particle forms a bond with a trap when the distance of their respective centres is lower than a certain distance, taken to be 1.5σ. A trapped particle is blocked by a harmonic potential and may escape thanks to thermal fluctuations; a bond breaks when the distance between the particle and the trap's centres is higher than 1.5σ. The depth of the harmonic potential (similar to the adsorption energy) can be tuned,

and its value directly impacts the characteristic time spent by a particle inside the trap. Note that the adsorption energy is chosen to be several orders of magnitude lower than the realistic one. This way, desorption events of particles appears in a reasonable time (< 100 ps), which eases the acquisition of a high statistics during the simulation time ($\sim$ µs).

Data analysis – The total number of free particles $N_f(t)$ inside the tube was evaluated every 0.1 ps. A partial signal is presented in figure 5.3. The Fourier transform $\tilde{N}_f$ of the fluctuations of $N_f(t)$ around its average

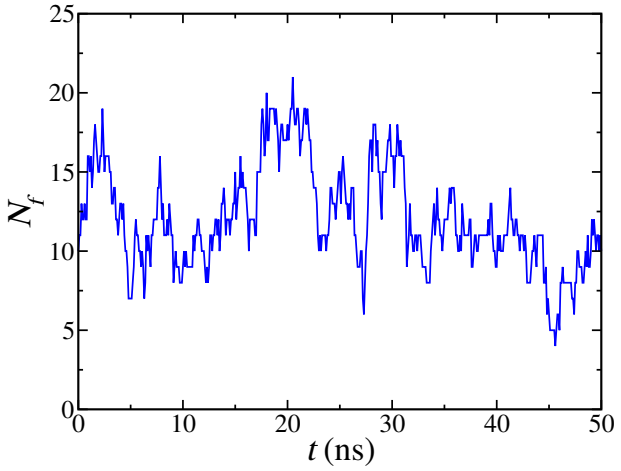

FIGURE 5.3: Evolution of the number of free ions N_f inside an infinite cylinder as the function of the time.

value $\delta N_f(t) = N_f(t) - \langle N_f \rangle$ was calculated thanks to the FFT algorithm [170, 171]. The square modulus of $\tilde{N}_f$ gives the Power Spectral Density (PSD) of $\delta N_f(t)$: $S_N(f) = |\tilde{N}(f)|^2/\mathrm{T}$, where T refers to the duration of the simulation.

5.2.2 Discussion and results' analysis

Typical PSD – Let us consider a cylinder of radius a=20 Å and a trap density of $\rho_t \sim 3$ part/nm^2. The chosen density of traps is close to the maximum density with no overlap between traps, the trap radius being 4.5 Å. This way, a particle cannot form a bond with more than one trap at a time. From the recorded number of free particles $N_f(t)$, the power spectral density, noted S, was calculated and plotted in figure 5.4. As one can see, the PSD contains three distinct parts, with three different slopes. It appears to be flat for low frequencies, to decrease as $1/f^2$ for high frequencies, and to

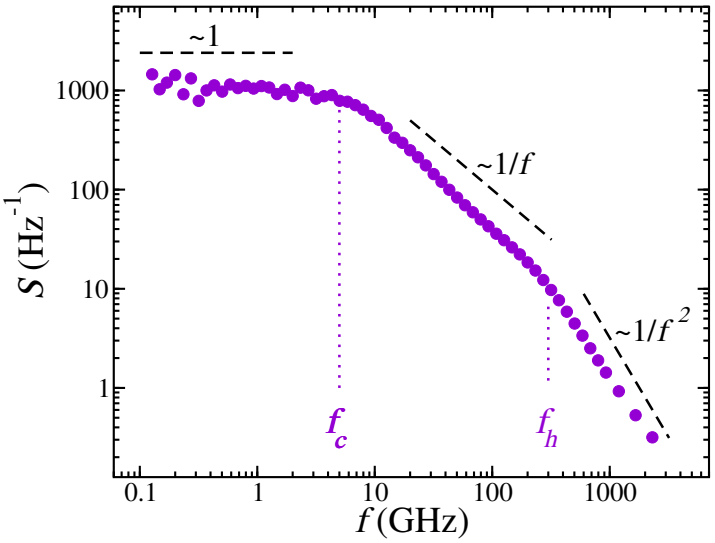

FIGURE 5.4: Power spectral density (S) of the number of free particles inside an infinite cylinder calculated with molecular dynamics simulations. Dashed and dotted lines are guides for the eyes.

be $\propto 1/f^{\alpha}$ with $\alpha \sim 1$ for intermediate frequencies. One can already notice the appearance of pink noise in an intermediate range of frequency. The existence of pink noise in simulated systems constitutes a first important result of this study. Each regime (each PSD slope) will be discussed below.

The characteristic frequencies separating the regimes are also of main interest in this study. Efforts will be made to link them to geometric, energetic or diffusion parameters of the simulation, with the purpose of extrapolating our results to more realistic systems. In figure 5.4, one may distinguish two characteristic frequencies. The first one separates the flat and the $1/f$ parts of the PSD, and is approximately equal to 5 GHz. We call it cut-off frequency f_c, because it is the frequency below which no pink noise (i.e. no interesting phenomena/no correlation) is observed. The second characteristic frequency separates the $1/f$ and $1/f^2$ parts of the PSD and is approximately equal to 300 GHz. Let us call it f_h for high frequency cut-off. The parameters that impact the respective values of f_c and f_h will be discussed below.

Duration distributions – As a first step, before exploring the impact of each simulation's parameter on the PSD, it is interesting to see what happens to a diffusing particle along the time. As seen in figure 5.5, each particle alternates between adsorbed and free states, which in term of the variable $N_f(t)$ translates in a series of 0 (the particle is trapped) and 1 (the

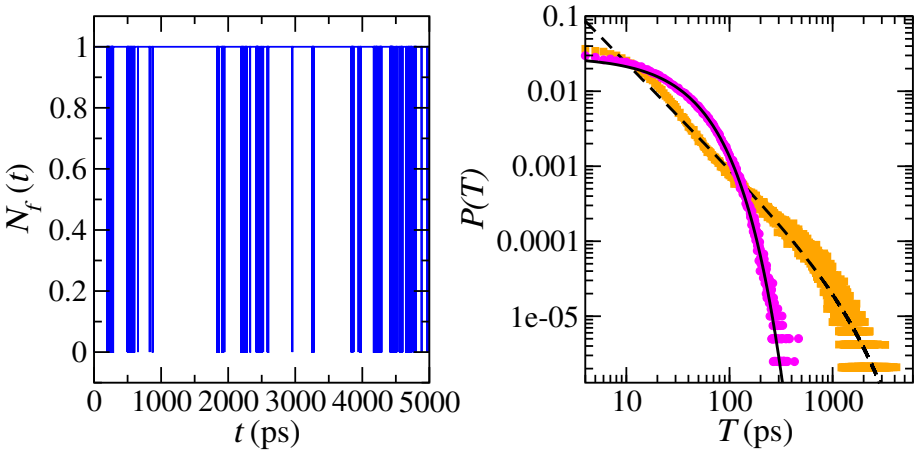

FIGURE 5.5: Left: evolution of the variable $N_f(t)$ for one single particle. Right: probability distributions of duration time for desorption events (pink circles) and adsorption events (orange squares) for particles inside an infinite cylinder. Black continuous line is $\sim \exp(-\lambda T)$ and black dashed line is $\sim \exp(-f_c T)/T^{3/2}$.

particle is free). What matters is how each state is distributed along time. The two considered events (adsorption and desorption) are controlled by very different processes. The time spent by a particle in a trap is governed by thermal fluctuations that have to make the particle pass over an energy barrier for the particle to get free. On the other hand, the time a particle spends free is governed by diffusion. To highlight the difference between these two processes in term of duration, one can extract from simulations their respective distributions of time. If normalized, it gives the probability $P(T)$ that the considered event lasts a duration T. Probability distributions of each process are plotted in figure 5.5. The distribution of the time spent by a particle in the bonded state, which will be called desorption distribution (since it corresponds to the distribution of time necessary for a desorption to occur), is exponential-like $P(T) \sim \exp -\lambda T$. The characteristic frequency of desorption (escape rate) λ is related to the energy of the trap which is an input of the simulation. By contrast, the adsorption distribution, i.e. the distribution of time spent by a particle in a free state between two adsorptions, is a power law [172] with a cut-off: $P(T) \sim T^{-3/2} \exp(-T/\tau_c)$. The cut-off, with characteristic time $\tau_c = 0.5$ ns, indicates that long time events do not exist. Note that this long-time cut-off is in good agreement with the low frequency cut-off observed in the PSD of figure 5.4, $\tau_c \sim 1/f_c$.

Link between duration distributions and PSD – As we have just seen, the minimum frequency f_c at which pink noise is observed corresponds

to the longest diffusion events $\tau_c \sim 1/f_c$. If no event lasts more than τ_c, this is due to both geometrical confinement which prevents long trajectories, and to the low trapping energy, which prevents long adsorption event from occurring. In other words, the system is entirely decorrelated if one waits more than τ_c, when any memory concerning previous states of the system is lost. This is in good agreement with the flat PSD observed at frequencies lower than f_c and coherent with the temporal distributions that do not show any event that lasts more than τ_c. For intermediate frequencies (5 GHz< f <300 GHz), the PSD is in $1/f^\alpha$ with $\alpha \sim 1$. One can see in figure 5.5 that there is a range of time for which only diffusion exists. This indicates that the pink noise is caused by the diffusion (re-adsorption event), which appears to be distributed as a power law. This is in good agreement with the prediction made in the introduction, supposing that only events distributed in time as a power law could lead to pink noise in the PSD. Finally, for high frequencies, the power spectrum is $\sim 1/f^2$, which is a well-known signature of an exponentially distributed event. In other words, for high frequencies, the power spectrum appears to be dominated by desorption events.

Cut-off frequencies – An important issue is to determine what fixes the two frequency limits, f_c and f_h. Following the previous discussion about the loss of memory at large times, one can deduce that f_c is fixed by the geometrical confinement. The longest possible trajectory for a diffusing particle in a confinement is governed by its diffusion coefficient D and the characteristic length of the system, here the radius a, so $f_c \approx D/a^2$. For a fixed diffusion coefficient, f_c is expected to decrease for increasing tube radius a. This was confirmed by a set of simulations made for various tube radii a, from 20 to 60 Å, whose results are represented in figure 5.6. The frequency f_c corresponds quite well to the prediction $f_c \approx D/a^2$. Note that f_c also varies with trap concentration (roughly $f_c \propto \rho_t$), which is related to the fact that at lower trap density, the probability of adsorption is lower, allowing for longer trajectories between two adsorptions. This can be interpreted in terms of an effective radius of the cylinder, which increases when decreasing the surface trap density. The second boundary, f_h, is identified as the limit above which desorption events dominate over adsorption. Accordingly, f_h is expected to decrease (which is equivalent to an increase of the characteristic adsorption times) with increasing adsorption

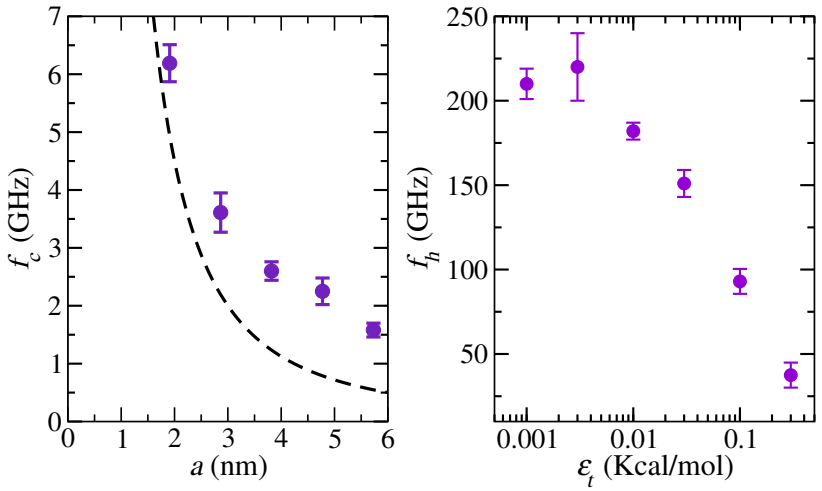

FIGURE 5.6: Left: low frequency cut-off f_c as a function of the tube radius a (symbols), and $f_c = D/a^2$ with D the diffusion coefficient of the particles (dashed line). Right: high frequency cut-off f_h as a function of the adsorption energy ϵ_t.

energy ϵ_t. This is confirmed by figure 5.6, in which f_h is plotted as a function of ϵ_t.

Slope α – The last issue we can tackle using molecular dynamics simulations concerns the slope of the pink noise α, that is measured in the frequency range between f_c and f_h ($S \propto 1/f^\alpha$). The first observation is that α is quasi-invariant with the tube radius a and particles concentration. However, α strongly varies with the surface trap density ρ_t, as shown in figure 5.7. In the studied range of surface densities, α was found to vary from ~ 0.5 to ~ 1.5. This strong variation highlights a link between the adsorption probability (which must depend on the trap density) and the slope α of the pink noise. α was also found to vary with the trapping energy ϵ_t, as shown in figure 5.7 where α is plotted as a function of the trapping energy ϵ_t for various trap densities ρ_t. The value of α saturates when $\epsilon_t \to 0$. The increase of α for increasing value of ϵ_t is probably due to a competition between the two distributions of duration time shown in figure 5.5. Indeed, increasing ϵ_t leads to an increase of the typical adsorption time, while the diffusion time stays unchanged. As seen previously, desorption events lead to $S \sim 1/f^2$, and for an increasing value of ϵ, one may expect $\alpha \to 2$. In conclusion, the observed pink noise is not a robust $1/f$ signal, but rather a $1/f^\alpha$ signal with α strongly dependent on the density of traps and on the energy of trapping.

Summary – To summarize, simulations lead to one major result: a combination of diffusion and adsorption can generate pink noise, i.e. power spectral density that decreases in $1/f^{\alpha}$ with $0 < \alpha < 2$ at intermediate frequencies. To go further and confirm the previous observations, a theoretical model of adsorption-desorption and diffusion inside an infinite cylinder is now presented. Note that the present model has been developed by Roland Netz and Lydéric Bocquet in parallel to simulations. See appendix B for details.

5.2.3 Theoretical model

Presentation of the model – The aim of the present model is to calculate the power spectral density of a system of N particles that reversibly adsorb on the surface of an infinite cylinder (see the appendix B for details). The system consists of a cylindrical tube containing N freely diffusing species, which is *exactly* the situation simulated previously. No electrostatic effect is included in this model, particles being considered as neutral. Let us define a state variable $n_A^i(t)$ equal to 1 when a particle is adsorbed on a surface, 0 otherwise. We are interested in the auto-correlation function of the total number of adsorbed particles $N_A(t)$: $\langle N_A(0)N_A(t)\rangle$. Using that ions are uncorrelated among each other, the auto-correlation function can be written

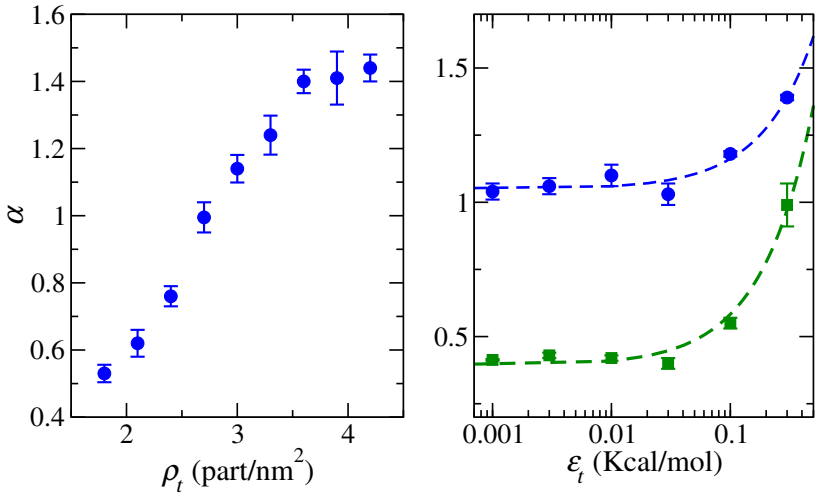

FIGURE 5.7: Left: slope α of the PSD for intermediate frequencies ($f_c < f < f_h$) for varying surface trap concentration ρ_t. Right: slope α for varying energy of trapping ϵ_t for two values of the trap density, dashed lines are guide for the eyes $\alpha \propto \epsilon_t$.

as

$$\langle N_A(0)N_A(t)\rangle = N^2p_A^2 + Np_AC_{AA}(t) - Np_A^2 \tag{5.5}$$

where p_A is the probability for a particle to be adsorbed and $C_{AA}(t)$ the single-ion correlation function, i.e. the probability for an ion to be adsorbed at t given that it is adsorbed at $t = 0$. This probability can be written in terms of the adsorption–desorption process combined with diffusive path in the bulk of the system:

$$C_{AA}(t) = \sum_{n=0}^{\infty}\left[\int_0^\infty \mathrm{d}t_e Q(t_e)\prod_{m=1}^{n}\left[\int_0^\infty \mathrm{d}t_m P(t_m)\int_0^\infty \mathrm{d}t'_m J(t'_m)\right]\right.$$
$$\left.\times\delta\left(t_e + \sum_{k=1}^{n}(t_k + t'_k) - t\right)\right] \tag{5.6}$$

where the outer sum counts the number of desorption and re-adsorption events. $P(t)$ is the desorption distribution, which we assume to be of exponential form: $P(t) = \lambda \mathrm{e}^{-t\lambda}$ with λ the characteristic frequency of the desorption. Its Laplace transform can be written as $\tilde{P}(f) = \lambda/(\lambda + 2\pi f)$. $Q(t)$ is called the survival distribution, it corresponds to the probability for an ion to be adsorbed over the time span from $t = 0$ to t and is given by $Q(t) = \int_t^\infty \mathrm{d}t' P(t')$. Its Laplace transform $\tilde{Q}(f)$ can be written as $1/(\lambda + 2\pi f)$. Finally, the first-return distribution $J(t)$ is the probability for an ion desorbed at time zero to return to the cylinder surface at t. The Laplace transform of $C_{AA}(t)$, defined as $\tilde{C}_{AA}(f) = \int_0^\infty \mathrm{e}^{-2\pi f t} C_{AA}(t)\mathrm{d}t$, can be written:

$$\tilde{C}_{AA}(f) = \frac{\tilde{Q}(f)}{1 - \tilde{P}(f)\tilde{J}(f)}. \tag{5.7}$$

Note that $\tilde{C}_{AA}(f = 0)$ is the probability that a particle is adsorbed. Similarly, one can construct $C_{AD}(t)$, the conditional probability that an ion that was desorbed at time $t = 0$ is desorbed at time t. Then $\tilde{C}_{AD}(f = 0)$ is the probability for a particle to be desorbed. Finally, we define the first-return distribution $J(t)$ as the probability for an ion desorbed at time zero to return to the cylinder surface at t.

The first-return distribution, in the case of an infinite tube of radius a can be written as

$$J(f)^{-1} = 1 + \frac{\sqrt{2\pi f D}}{k}\frac{I_1(a\sqrt{2\pi f/D})}{I_0(a\sqrt{2\pi f/D})} \tag{5.8}$$

where $I_0(x)$ is a modified Bessel functions and $\partial_x I_0(x) = I_1(x)$ [173]. D is the diffusion coefficient and k is a phenomenological rate constant equal to the ionic outgoing flux across the tube boundary divided by the ionic density along this boundary.

Comparison with molecular dynamics simulations – According to the analytical calculations, the power spectral density of the adsorption signal can be estimated as the the real of equation (5.7) with $J(f)$ from equation (5.8): $S(f) = C_{AA}(if) + C_{AA}(-if)$. The result, for different trap densities is represented with plain lines in figure 5.8. On the same figure, power spectral densities resulting from MD simulations for the same system parameters are represented with symbols. The agreement between theory and MD simulations is excellent. One finds that the k coefficient of the

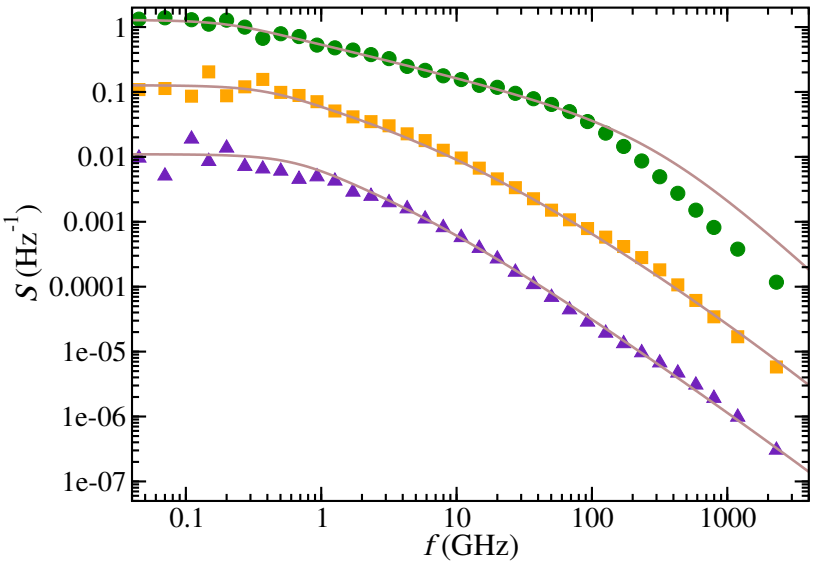

FIGURE 5.8: Symbols: power spectral density S extracted from molecular dynamics simulations for a cylinder of radius $a = 10$ nm, an adsorption energy of $\epsilon_t = 0.1\,\mathrm{Kcal/mol}$, a diffusion coefficient $D = 1.8 \cdot 10^8\,\mathrm{m^2/s}$ and a trap density $\rho_t = 1.8\,\mathrm{part/nm^3}$ (green circles), $3\,\mathrm{part/nm^3}$ (orange squares) and $4.2\,\mathrm{part/nm^3}$ (violet triangles). Full lines are real part of equation (5.7) with respectively $k = 80$, 400 and 800 m/s, $a = 28$, 20 and 15 nm, $\lambda = 300\,\mathrm{GHz}$ and $D = 1.8 \cdot 10^8\,\mathrm{m^2/s}$.

model impacts the slope of the pink part of the PSD, as highlighted in figure 5.8. An increase of k in the model corresponds to an increase of the surface trap density ρ_t in the simulations. This indicates that the phenomenological rate k is related to the probability of adsorption in surface, which depends on the trap density. Moreover the ratio D/a^2 fixes the low frequency cut-off in both simulation and model, with an effective radius a taken to be slightly larger than the real radius, and depending on the trap concentration.

5.2.4 The need to go further

Summary – The study of the number of diffusing particles inside an infinite cylinder with adsorbing surfaces has revealed the existence of pink noise when considering the number of freely diffusing particles. The presence of pink noise has been confirmed both numerically and theoretically, and constitutes the first important result of the present study. It has been identified that the key ingredient for the appearance of pink noise lies in the way the "first-return" trajectories of particles between two adsorption are distributed in time, i.e. $\sim T^{-3/2}$. This power law distribution is the signature of diffusion, which is therefore at the base of the presence of pink noise.

Remark – It is good to keep is mind that the motivation of the present study comes from some experiments that have reported pink noise when studying fluctuations of the ionic current through a charged nanopore. Even if the system considered here is neutral for numerical simplifications, fluctuations in the number of free particles $\delta N_t(t)$ can be associated with the fluctuations in the number of free carriers in the case of a charged system. Similarly, fluctuations in the number of trapped particles can be associated with surface charge fluctuations $\delta\Sigma(t)$, again in the case of a charged system. Neutral and charged systems will be proved to have similar behaviors hereafter.

Major limitation – One major problem remains: the pink noise only appears in a restricted range of frequencies, whose lower limit can be roughly approximated by $f_c \approx D/a^2$. Obviously, this limitation does not exist in experimental systems since some experiments report pink noise spanning to frequencies as low as 1 Hz. Indeed, a quick estimation shows that an expected cut-off in such system is $D/a^2 \sim 10\,\mathrm{MHz}$, with D a typical diffusion coefficient for ions taken to be $D = 1 \cdot 10^{-9}\,\mathrm{m}^2/\mathrm{s}$ and a a typical nanopore radius taken to be $a = 10\,\mathrm{nm}$. Hence the expected cut-off frequency (from our results) is much higher that the sub-Hz measured experimentally. To solve this problem, we clearly need to push further the present study, and consider a system much closer to experimental ones: a finite cylinder (nanopore) connected to large reservoirs. Such a system is not as confining as an infinite cylinder due to the connection to large

reservoirs. So it is expected that the cut-off frequency will be decreased to frequencies lower than D/a^2.

5.3 Noise in a nanopore

In the previous section, it has been shown that pink noise in the power spectral density exists when considering the number of adsorbed particles on the surface of a cylindrical infinite tube. The geometrical constraints of the tube induced a low frequency cutoff which is inconsistent with experimental measurements. We now extend the present study to the case of a cylindrical pore connected to reservoirs. The idea is that, in this configuration, trajectories between two adsorption-desorption events are not limited by the pore size anymore, but are limited by the reservoir size instead, which is supposed to be large in comparison with pore's dimensions. This configuration was explored using molecular dynamics simulations, as presented below. We found that, as expected, the cut-off frequency, i.e. the frequency below which the noise is white, is pushed towards lower frequencies. Moreover, this cut-off is governed by the time spent by particles inside the pore. This is the second major result of this study. Due to the poor level of symmetry, and contrary to the case of an infinite cylinder, no theoretical model have been built yet in this particular configuration.

5.3.1 Description of the studied system

The system consists of a cylindrical nanopore of radius a, pierced in a membrane of width L and connected to large reservoirs of size $R_{\text{res}} \gg a$. It is filled with particles that can adsorb on the surface of the nanopore (see figure 5.9). Just like in the case of the infinite cylinder, we are interested in the number of particles freely diffusing inside the pore $N_f(t)$. It is defined as the total number of particles inside the pore $N_{\text{t}}(t)$ minus the total number of bonded particles N_{b}: $N_{\text{f}}(t) = N_{\text{t}}(t) - N_{\text{b}}(t)$. This is a pertinent quantity to evaluate if one keeps in mind that the initial goal was to understand the presence of pink noise in the ionic current. Extrapolating our results to the complete case of a charged system, one expects the ionic current to behave as N_{f}, the number of free carriers inside the pore, in the first order

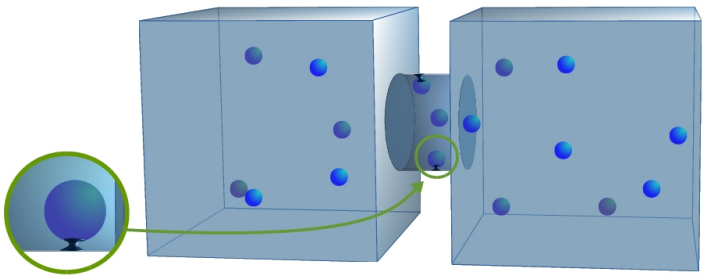

FIGURE 5.9: Drawing of the system of interest. A cylindrical nanopore of radius a and length L connects two reservoirs of characteristic size R_{res}. Particles fill both reservoirs and the inside tube, and can bond with the tube surface.

of approximation. In this case, and by opposition to the previously studied infinite nanotube, two kinds of events are expected to impact $N_{\text{f}}(t)$; the reversible adsorption of particles at the surface of the pore and the particles exchange with reservoirs. Change in power spectral density is therefore expected, as we will see below.

The technical details of the simulation are the same as in the case of the infinite cylinder. The only difference, besides the geometry, is that two quantities are recorded: the number of bonded particles $N_{\text{b}}(t)$ and the total number of particles inside the tube $N_{\text{t}}(t)$.

5.3.2 Results

Typical PSD – The case of a nanopore of radius $a = 20$ Å and length $L = 30$ Å connected to large reservoirs of size $R_{\text{res}} = 100$ Å is considered here. A surface trap density $\rho_T = 3$ part/nm^2 with energy $\epsilon_t = 0.1$ Kcal/mol is located on the surface of the nanopore. The PSD of the number of free particles inside the pore $N_{\text{f}}(t)$ is plotted in figure 5.10. As a comparison, the PSD obtained in the previously studied case of an infinite tube of same radius, same density of trap and same trapping energy is plotted. In both cases, one can define the cut-off frequency f_c as the limit between the low frequency white noise ($S \sim 1$) and the pink noise $\sim 1/f$. One can see that the cut-off frequency is lower in the case of the nanopore. Indeed, while f_c is around 6 Ghz in the case of the infinite tube, it is around 0.2 Ghz in the case of the nanopore. So the pink noise exists on a larger range of frequencies in the case of the nanopore compared to the infinite tube case. This result is important since to explain experimental results, one has to

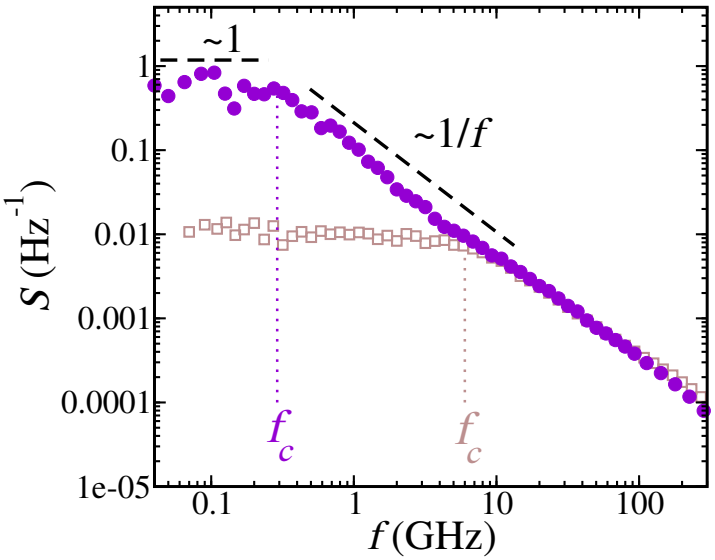

FIGURE 5.10: Symbols: PSD of the number of free particles inside a nanopore connected to reservoirs (violet circle) and inside an infinite nanotube (brown squares). The cut-off frequency f_c is defined in both cases as the intersection between the flat part $S \sim 1$ at low frequency and the pink part $S \sim 1/f^{\alpha}$ with $\alpha \sim 1$. Black dashed and dotted lines are guides for the eyes.

justify the possibility of pink noise at very low frequencies (down to the hertz). In the following, we determine what impacts the value of f_c in the case of a nanopore connected to large reservoirs.

Low frequency cut-off – Let us explore the dependence of f_c as a function of the simulation parameters in order to determine what fixes the lower limit at which pink noise can be observed. It appears that f_c is strongly dependent in both pore's lengths L and trap's energies ϵ_t, as shown in figure 5.11, where $\tau_c = 1/f_c$ is plotted for various pore length L and trapping energy ϵ_t. The cut-off time appears to be proportional to the length of the tube L. Moreover, it varies exponentially with the energy of trapping ϵ_t. Altogether, these results indicate that f_c depends mainly on the time spent by particles inside the pore, which is indeed expected to increase with the pore size and with the energy of trapping. The duration spent by particles inside the pore comes from the alternate of adsorption and diffusion.

Slope α – Finally, one may wonder if the slope α of the pink noise is robust or depends on the parameters of the simulation. α is plotted in figure 5.12 as a function of both the trapping energy ϵ_t and the pore length L. α is found to decrease with increasing ϵ_t and increase with increasing L. Understanding the meaning of these variations is beyond the scope of the

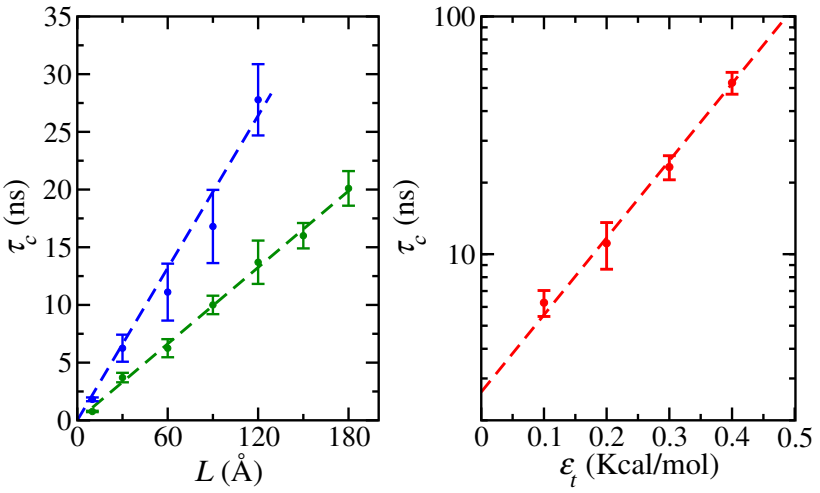

FIGURE 5.11: Evaluated cut-off time $\tau_c = 1/f_c$ corresponding to low frequency cut-off. Left: τ_c as a function of the pore length L for two values of trapping energy $\epsilon_t = 0.1$ and 0.2 Kcal/mol, respectively in green and blue. Dashed lines are guides for the eyes $\tau_c \propto L$. Right: τ_c as a function of the trapping energy ϵ_t for a pore length L=60 Å. Dashed lines are guides for the eyes $\tau_c \propto \exp(\epsilon_t)$.

present study, one will simply notice that the slope α of the pink part of the PSD is not a robust $1/f$, but rather depends on the simulation parameters.

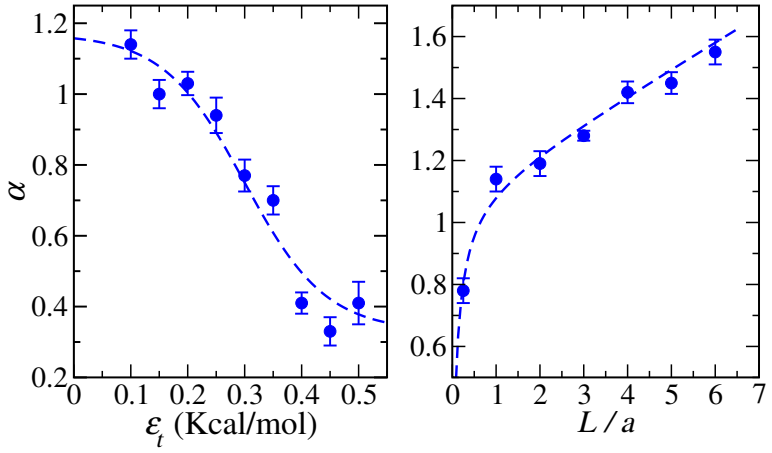

FIGURE 5.12: Left: slope α of the PSD for intermediate frequencies ($f_c < f < f_h$) for varying energy of trapping ϵ_t. Right: slope α for varying ratio pore length L over pore radius a. Dashed lines are guides for the eyes.

Summary – Some very interesting conclusions can be drawn from the present molecular dynamics results. First, as already seen in the infinite cylinder case, diffusion combined to reversible adsorption of particles on a solid surface leads to pink noise in the power spectral density. Second, in the geometry of a nanopore in contact with large reservoirs, pink-noise can be obtained at very low frequencies, which was an important limitation of the infinite cylinder geometry. It has been found that the limiting

frequency until which the noise behaves as $\sim 1/f^{\alpha}$ with $\alpha \sim 0.5 - 1.5$ is controlled by the characteristic time spent by the particles inside the pore. This characteristic time depends mostly on both pore dimensions and surface adsorption energy. This is a crucial observation since our primary objective was to find the existence of pink noise at very low frequencies (down to 1 Hz) in the PSD of ionic current through nanopores. Considering a realistic adsorption energy, for example 0.4 eV [44], an extrapolation from our molecular dynamics results (figure 5.11 in particular) using a realistic diffusion coefficient ($10^{-9}\,\mathrm{m}^2/\mathrm{s}$) allows us to reasonably assume that reversible adsorption combined to diffusion of carriers may lead to pink noise at frequencies down to $1 - 10\,\mathrm{Hz}$. This is a major result of the present study. Particles alternating adsorption and diffusion inside the pore potentially spend very long time inside the pore. This translates in pink noise at very low frequencies when considering the PSD of the number of particles inside the pore. This result confirms our primary intuition that fluctuations of the surface charge due to reversible adsorptions of carriers is a serious candidate for explaining the origin of the mysterious pink noise observed in ionic current measurements. The trajectories followed by the particles between consecutive adsorptions have durations distributed as power laws, which is a key ingredient to the generation of pink noise.

However, most of our results have been obtained with a neutral system, assuming that the existence of charge (carrier by both particles and pore surface) does not dramatically change the behaviour of particles nor the measured power spectral density. To prove this point, which is important considering the analogy with real systems, we now show a comparison between both the charged and the neutral case.

5.3.3 Comparison with the charged case

We performed a simulation very similar to the one made with a neutral system. A nanopore of same length and radius ($L = a = 2\,\mathrm{nm}$) is connected to large reservoirs ($R_{\mathrm{res}} \gg a$). The pore has a surface charge $\Sigma = -60\,\mathrm{mC}/\mathrm{m}^2$, and diffusing particles are charged (respectively charge $+e$ for counterion and $-e$ for co-ion). Long-range Coulombic interactions were computed using the particle-particle particle-mesh (PPPM) method [83, 84]. The

number of ions was chosen in order to ensure the electroneutrality of the system. The bulk salt concentration was chosen to be 0.2 mol/L, leading to a Debye length λ_D slightly smaller than the radius a. Counterions can reversibly adsorb on surface with an energy $\epsilon_t = 0.1\,\text{Kcal/mol}$. The number of free carriers inside the pore $N_f^+ + N_f^-$ was evaluated, and its power spectral density is plotted in figure 5.13. Charged and neutral systems show similar PSD. In both cases there are three parts, separated by similar cut-off frequencies, and presenting similar slopes (~ 1 at low frequencies, $\sim 1/f^\alpha$ with $\alpha \sim 0.5$ at intermediate frequencies) and $\sim 1/f^2$ at high frequencies. Hence the previous discussion and results most probably applies to charged systems. One may expect slight differences, due to additional electrostatic interaction that may modify the trajectories. This description is beyond the scope of the present study.

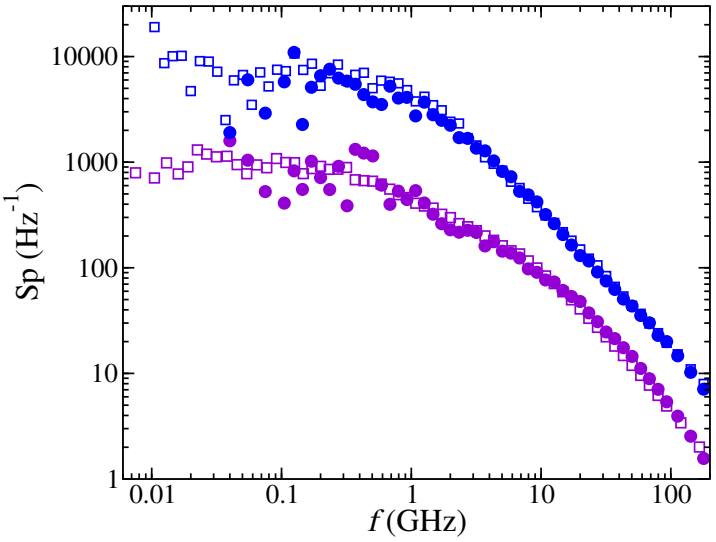

FIGURE 5.13: PSD of the number of free particles inside respectively a charged (full circles) and neutral (empty squares) nanopores for $\epsilon_t = 0.1$ Kcal/mol (blue) and $\epsilon_t = 0.4$ Kcal/mol (violet).

5.4 The need for an analytical model for noise in nanopore

In the spirit of what has been done for the diffusing-adsorbing dynamics of particle inside an infinite cylinder, the present study with a nanopore geometry lacks an analytical confirmation.

This analytical confirmation must describe the probability for a particle to be free inside a nanopore. In analogy with equation (5.6), one has to sum over all different paths that start and end at a time t inside the pore. It implies calculating a survival probability (for the particle inside the pore, which may both adsorb on the pore surfaces and leave the pore for the reservoir), a desorption probability distribution (same as previously, $P(t) = \lambda \exp(-\lambda t)$) and a first return rate (for particles coming back inside the pore after visiting a reservoir).

The building of this model is, today, still in progress.

5.5 Conclusion

In this study, we first showed, using molecular dynamics simulations, the presence of pink noise (in a limited range of frequencies) when considering particles alternating between diffusion and reversible adsorption on the surface of an infinite cylinder. The importance of the result lies in the fact that we linked such a simple system to the $1/f^{\alpha}$ power spectral density, which was the main motivation of the present study. Results show that the key point for the generation of pink noise is the time distribution of the first return (to the surface) trajectories, which follow a power law. This was confirmed by an analytical model, which compares well with simulations results.

The previous study showed that the geometric confinement of the particles results in a restriction of the frequency span of the pink-noise regime. Therefore we conducted a similar study, where particles are diffusing inside a cylindrical nanopore connected to large reservoirs. In this case, even if the observed pink noise is still limited to a certain range of frequencies, this range can be extended to extremely low frequencies by tuning for example the energy of trapping, which impacts the time spent by particles inside the pore. An extrapolation from our results indicates that the pink noise associated with first return trajectories between adsorption/desorption events could be found at very low frequencies (1-10 Hz). Therefore, it represents a serious candidate for explaining the presence of pink noise in ionic current measurement through nanopores.

Note that, in this study, we considered systems at equilibrium only. However, it would be interesting to consider the effect of a flow on the measured power spectral density. Hence, a complete model would include the effect of the convection on the effective diffusion coefficient of (adsorbing-desorbing) ions [174]. According to experimental measurements of current flow through solid nanopores, one may expect an increase of the level of noise with the flow [159]. Ultimately, a full understanding between the system properties and the signature of the noise may allow to extract some information about the system from the power spectral density.

Chapter 6

General conclusion

This thesis discusses various situations linked to transport at the nanoscale. While the first chapter is an introduction to nanofluidics, containing a review of characteristic lengths, forces or phenomena existing at the nanoscale, the other four chapters describe each a study that can be read independently from the other.

The second chapter focuses on the hydrodynamic entrance effects in a nanopore. Using both finite element calculations and molecular dynamics results, we explored the impact of both the hydrodynamic boundary condition and the geometry on the hydrodynamic permeability of a nanopore. Our main result is that, compared to a cylindrical nanopore, **a hourglass nanopore presents an enhanced hydrodynamic permeability**, and that **there is one specific opening angle that optimizes the water flow**. Strikingly, **this angle appears to be close to the angle measured in the aquaporin**, a natural water channel.

The third chapter is a study of capillary filing inside subnanometric channels. Using molecular dynamics simulations, we measured both the velocity filling and the Laplace pressure inside nanochannels whose diameter was close to the size of fluid molecules. Our main result is that **both velocity and pressure show strong non-linearity with the channel radius**, contrary to classical capillarity predictions. These deviations between measurement and prediction have been found to be mostly due to the discrete nature of the fluid structuring that generates a disjoining pressure.

The fourth chapter is a study of nanofluidic diodes. Using molecular dynamics simulations, finite element calculations and an analytical model, we showed that **the coupling between water flow and ion dynamics leads to a water flow rectification**. Moreover, we extended the conventional study of nanofluidic diodes to the case of non-overlapping electric double layers, and showed the possibility of current and flow rectification in this configuration as well.

The fifth and last chapter is a study of the presence of pink noise in ionic current measurements through nanopores. Using both molecular dynamics simulations and an analytical model, we studied the fluctuations in the number of particles reversibly adsorbing on the surface of both an infinite cylinder and a cylindrical nanopore connected to large reservoirs. Both numerically and theoretically, **we show the existence of pink noise on a limited range of frequencies in the considered systems**. We found that pink noise originates from the first return trajectories, and in particular their durations, which are controlled by the diffusion process occurring between two adsorptions of the particle on the pore's surface.

Perspectives – Some perspectives for future studies can be drawn from the present work. For example, the study of the shape of nanopores inspired by aquaporins indicates that the use of a hourglass shaped pore may lead to a significant improvement of water permeability, in comparison with pierced graphene which is commonly seen as the ultimate tool for water filtration. Hence this is of main interest for the fabrication of highly efficient membranes for water desalination. This study could be pushed further in order to determine the optimal shape for a nanopore, which is probably slightly different from the hourglass. Concerning the desalination and water filtration, our results indicate that nanofluidic diodes can be used to rectify the water flow using an external applied electric field. This is a very interesting way to control the flow from a technological point of view. Indeed, in comparison with the classic reverse osmosis method, pressure pomps are replaced by electrodes, which is certainly more convenient, in particular for small desalination plants.

In another work, we made the observation that the capillary filling of subnanometric channels is strongly impacted by the discrete nature of the fluid, with the possibility to switch the pore behaviour from hydrophilic

to hydrophobic for some specific radius values. This may have a strong impact on the imbibition of nanoporous media, and it would be worthwhile to perform experiments in order to observe this phenomena. Moreover, our results indicate that a small change in the pore radius can have a dramatic impact on its affinity for a fluid, depending on both the fluid particle diameter and the pore dimensions. Hence it could be an important criterion for the selectivity of nanoporous membranes, and may already be involved in the selectivity of natural nanochannels.

Finally, our results concerning fluctuations of particles inside nanopores indicate that some information about the pore geometry or adsorption energy of particles on surface could be extracted from the observation of a cut-off at low frequency in the power spectral density. Our current results could be pushed further with a calculation for the geometry of the nanopore connected to reservoirs, and then by the introduction of convection. If confirmed theoretically, a link between the fluctuations (and accordingly the power spectral density) of a ionic current measured through a nanopore and the transport properties could be established, which would constitute a new method for extracting information about flow at the nanoscale.

Appendix A

Nanofluidic osmotic diode, analytical calculation

This appendix is based on the following supplementray material: [175].

We consider here an asymmetrically charged nanochannel of length L and height h, as depicted in figure A.1. The left side of the channel has a positive

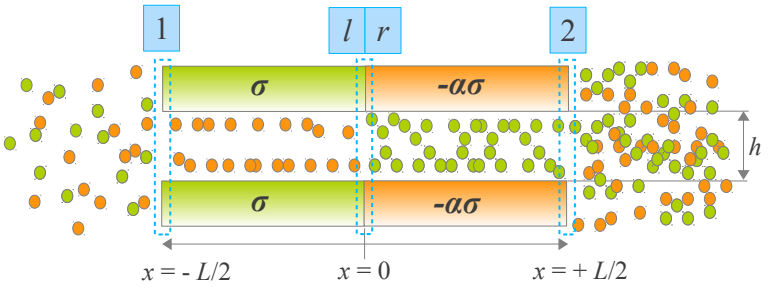

FIGURE A.1: Sketch of the system showing the asymmetry of surface charge in the nanochannel, and the different salt concentrations in the left and right reservoirs.

surface charge density σ while the right side has a negative surface charge $-\alpha\sigma$, with $\alpha > 1$ a numerical coefficient. Each end of the channel is in contact with a reservoir of concentration $n_L = n_0 - \Delta n/2$ and $n_R = n_0 + \Delta n/2$ in the left and right ends, respectively. A voltage drop $\Delta V = V_R - V_L$ is also applied between the two reservoirs. Three space charge zones (SCZs), denoted by 1, lr, and 2 in figure A.1 appear due to the discontinuities of the surface charge: between the reservoirs and the left and right inner ends of

the nanochannel, and in the junction between the positively and negatively charged sides of the channel.

For the sake of simplicity, we will use reduced units $\tilde{x} = x/L$, $\tilde{n} = n/n_0$, $\tilde{V} = eV/k_BT$, $j_\pm = J_\pm L/Dn_0$ in terms of the length of the system L and the average concentration of the reservoirs n_0. Since we will exclusively use reduced units in the rest of the text, we remove the tildes of the reduced units keeping in mind that in the following, all the variables are dimensionless.

In reduced units, the Nernst-Planck transport equations in the low Peclet number regime read

$$j_\pm = -\nabla n_\pm \mp n_\pm \nabla V \tag{A.1}$$

and give us the fluxes of the negative j_- and the positive j_+ species. The solute j_s and electric j_e fluxes are defined as

$$\begin{aligned} j_s &\equiv j_+ + j_- = -\nabla n_{\text{sol}} - (n_+ - n_-)\nabla V \\ j_e &\equiv j_+ - j_- = -\nabla(n_+ - n_-) - n_{\text{sol}}\nabla V \end{aligned} \tag{A.2}$$

in terms of the total ion concentration $n_{\text{sol}} = n_+ + n_-$.

We will also apply a local electroneutrality ansatz. This means that everywhere in the system (out of the SCZs), the positive and negative charges should compensate to give a total zero charge. This gives the following relationship between surface and bulk charges in reduced units,

$$\begin{aligned} n_- - n_+ &= 2\delta, \quad -1/2 < x < 0 \\ n_+ - n_- &= 2\alpha\delta, \quad 0 < x < 1/2 \end{aligned} \tag{A.3}$$

where δ is the surface-to-bulk charge ratio $\delta = |\Sigma|/hn_0$, corresponging to a Duhkin number.

Making use of the electroneutrality condition (A.3), the expression for the electric flux j_e in equations (A.2) can be further simplified to

$$\begin{aligned} j_s &\equiv j_+ + j_- = -\nabla n_{\text{sol}} - (n_+ - n_-)\nabla V \\ j_e &\equiv j_+ - j_- = -n_{\text{sol}}\nabla V \end{aligned} \tag{A.4}$$

We will focus on the minority species on each side of the junction, i.e. n_+ on the left side and n_- on the right side. This means that we will express n_{sol} as

$$n_{\text{sol}} = 2(n_+ + \delta), \quad -1/2 < x < 0 \tag{A.5}$$

$$n_{\text{sol}} = 2(n_- + \alpha\delta), \quad 0 < x < 1/2 \tag{A.6}$$

making use of equations (A.3). Furthermore, we will focus on the fluxes $j_+ = (j_s + j_e)/2$ on the left side and $j_- = (j_s - j_e)/2$ on the right side, according to the minority species on each side.

A.0.1 General case

Left side $-1/2 < x < 0$**:** Regarding the concentration of the minority species we have

$$j_+ = \frac{1}{2}(j_s + j_e) = -\nabla n_+ - n_+ \nabla V$$

Multiplying both sides of the equation by n_{sol}, recalling that $-n_{\text{sol}}\nabla V = j_e$, substituting n_{sol} by equation (A.5) and reorganizing terms, we arrive to the equation

$$j_s(n_+ + \delta(1 + j_e/j_s)) + 2(n_+ + \delta(1 + j_e/j_s) - \delta j_e/j_s)\nabla n_+ = 0, \tag{A.7}$$

that can be easily integrated as

$$2n_+ - 2\delta\frac{j_e}{j_s}\log(n_+ + \delta(1 + \frac{j_e}{j_s})) + j_s x = C_{n_+} \tag{A.8}$$

where C_{n_+} is a constant of integration.

In order to integrate the voltage we make use of the expression for the electric flux,

$$j_e = -n_{\text{sol}}\nabla V = -2(n_+ + \delta)\nabla V = -2(n_+ + \delta)\nabla_{n_+} V \nabla n_+$$

which, making use of equation (A.7) turns,

$$j_e = j_s\left(n_+ + \delta\left(1 + \frac{j_e}{j_s}\right)\right)\nabla_{n_+} V \tag{A.9}$$

that can be easily integrated to

$$V = \frac{j_e}{j_s} \log\left(n_+ + \delta\left(1 + \frac{j_e}{j_s}\right)\right) + C_{V_+} \tag{A.10}$$

with C_{V_+} a constant of integration.

Right side $0 < x < 1/2$**:** Following the same procedure as for the left side for the minority species, n_- in this case, we arrive to the equation

$$\begin{aligned} j_s(n_- + \alpha\delta(1 - j_e/j_s)) + 2(n_- + \alpha\delta(1 - j_e/j_s) + \\ \alpha\delta j_e/j_s)\nabla n_- = 0 \end{aligned} \tag{A.11}$$

that is integrated to

$$2n_- + 2\alpha\delta\tfrac{j_e}{j_s}\log(n_- + \alpha\delta(1 - \tfrac{j_e}{j_s})) + j_s x = C_{n_-} \tag{A.12}$$

where C_{n_-} is a constant of integration.

Regarding the voltage,

$$j_e = -n_{\text{sol}}\nabla V = -2(n_- + \alpha\delta)\nabla V = -2(n_- + \alpha\delta)\nabla_{n_-} V \nabla n_-$$

which, making use of equation (A.11) turns,

$$j_e = j_s\left(n_- + \alpha\delta\left(1 - \frac{j_e}{j_s}\right)\right)\nabla_{n_-} V$$

that integrates to

$$V = \frac{j_e}{j_s} \log\left(n_- + \alpha\delta\left(1 - \frac{j_e}{j_s}\right)\right) + C_{V_-} \tag{A.13}$$

with C_{V_-} a constant of integration.

Boundary conditions at the SCZs:

SCZ 1: The electroneutrality condition as well as the continuity of the electrochemical potential must hold

$$\begin{aligned} n_-^1 - n_+^1 &= 2\delta \qquad (A.14)\\ \log(1-\Delta n/2) + \Delta V &= \log(n_-^1) - V_1 \\ \log(1-\Delta n/2) - \Delta V &= \log(n_+^1) + V_1 \end{aligned}$$

Adding and subtracting the two last equations we obtain respectively,

$$(1-\Delta n/2)^2 = n_+^1 n_-^1 \qquad (A.15)$$

$$V_1 = -\Delta V + \frac{1}{2}\log\left(\frac{n_-^1}{n_+^1}\right) \qquad (A.16)$$

SCZ lr: We call l the left side of the junction and r the right side of the junction.We then have,

$$\begin{aligned} n_-^l - n_+^l &= 2\delta \\ n_+^r - n_-^r &= 2\alpha\delta \\ \log(n_-^l) - V_l &= \log(n_-^r) - V_r \\ \log(n_+^l) + V_l &= \log(n_+^r) + V_r \end{aligned}$$

Adding and subtracting the two last equations we obtain respectively,

$$\frac{n_-^l}{n_-^r} = \frac{n_+^r}{n_+^l} \qquad (A.17)$$

$$V_l - V_r = \log\left(\frac{n_+^r}{n_+^l}\right) = \log\left(\frac{n_-^l}{n_-^r}\right) \qquad (A.18)$$

SZC 2: Following the same reasoning as for the SCZ 1,

$$\begin{aligned} n_+^2 - n_-^2 &= 2\alpha\delta \qquad (A.19)\\ \log(1+\Delta n/2) &= \log(n_+^2) + V_2 \\ \log(1+\Delta n/2) &= \log(n_-^2) - V_2 \end{aligned}$$

Adding and subtracting the two last equations we obtain respectively,

$$(1 + \Delta n/2)^2 = n_+^2 n_-^2 \tag{A.20}$$

$$V_2 = \frac{1}{2} \log \left(\frac{n_-^2}{n_+^2} \right) \tag{A.21}$$

A.0.2 Large δ case

If the surface charge dominates over the charge coming from the salt solution, i.e., $\delta \gg 1$, appropriate approximations can be made that allow us to obtain analytical solutions of the equations. We begin by the electroneutrality conditions (A.3) which if $\delta \gg 1$ can be simplified as follows,

$$\begin{aligned} n_- &\simeq 2\delta, \quad -1/2 < x < 0 \\ n_+ &\simeq 2\alpha\delta, \quad 0 < x < 1/2 \end{aligned} \tag{A.22}$$

where, on each side of the junction, only the minority species has a role. This approximation is widespread in the semiconductors literature. Furthermore, if $\delta \gg 1$ we can also approximate equations (A.5), (A.6) by

$$n_{\text{sol}} \simeq 2\delta, \quad -1/2 < x < 0 \tag{A.23}$$

$$n_{\text{sol}} \simeq 2\alpha\delta, \quad 0 < x < 1/2 \tag{A.24}$$

Left side $-1/2 < x < 0$**:** Under the condition $\delta \gg 1$, equation (A.7) becomes

$$j_s + j_e \simeq -2\nabla n_+, \tag{A.25}$$

that is easily integrated to

$$n_+ + \tfrac{1}{2}(j_s + j_e)x \simeq C_{n_+\delta} \tag{A.26}$$

with $C_{n_+\delta}$ a constant of integration. While the voltage equation

$$j_e = -n_{\text{sol}} \nabla V \simeq -2\delta \nabla V \tag{A.27}$$

can be integrated as

$$V \simeq \frac{-j_e}{2\delta}x + C_{V_l} \tag{A.28}$$

with C_{V_l} a constant of integration.

Right side $0 < x < 1/2$**:** Under the condition $\delta \gg 1$, equation (A.11) becomes

$$j_s - j_e = -2\nabla n_- \tag{A.29}$$

that can be integrated as

$$n_- + \tfrac{1}{2}(j_s - j_e)x = C_{n_-\delta} \tag{A.30}$$

with $C_{n_-\delta}$ a constant of integration. While the voltage, as before, can be integrated as

$$j_e = -n_{\text{sol}}\nabla V \simeq -2\alpha\delta\nabla V \tag{A.31}$$

$$V \simeq \frac{-j_e}{2\alpha\delta}x + C_{V_r} \tag{A.32}$$

with C_{V_r} a constant of integration.

Boundary conditions at the SCZs: In the $\delta \gg 1$ case, the boundary conditions are much simpler for the three SCZs.

SCZ 1**:**

$$n_-^1 \simeq 2\delta \tag{A.33}$$

$$n_+^1 \simeq \frac{1}{2\delta}\left(1 - \frac{\Delta n}{2}\right)^2 \tag{A.34}$$

$$V_1 \simeq -\Delta V + \log\left(\frac{2\delta}{1 - \Delta n/2}\right) \tag{A.35}$$

SCZ lr**:**

$$n_-^l \simeq 2\delta \tag{A.36}$$

$$n_+^r \simeq 2\alpha\delta \tag{A.37}$$

$$V^l - V^r \simeq \log\left(\frac{2\alpha\delta}{n_+^l}\right) \simeq \log\left(\frac{2\delta}{n_-^r}\right) \tag{A.38}$$

SCZ 2**:**

$$n_+^2 \simeq 2\alpha\delta \tag{A.39}$$

$$n_-^2 \simeq \frac{1}{2\alpha\delta}(1+\frac{\Delta n}{2})^2 \tag{A.40}$$

$$V_2 \simeq \log\left(\frac{1+\Delta n/2}{2\alpha\delta}\right) \tag{A.41}$$

Analytical solution

This approximation reduces the number of unknowns and with the simple equations and boundary conditions that we have obtained, we can proceed straightforward to the full integration of the equations to obtain the remaining unknowns, n_+^l, n_-^r, V^l and V^r.

$$n_+^l = \frac{(1-\Delta n/2)^2}{2\delta} - \frac{j_s + j_e}{4} \tag{A.42}$$

$$n_-^r = \frac{j_s - j_e}{4} + \frac{(1+\Delta n/2)^2}{2\alpha\delta} \tag{A.43}$$

$$V^l = -\Delta V - \frac{j_e}{4\delta} + \log\left(\frac{2\delta}{1-\Delta n/2}\right) \tag{A.44}$$

$$V^r = \frac{j_e}{4\alpha\delta} - \log\left(\frac{2\alpha\delta}{1+\Delta n/2}\right) \tag{A.45}$$

Subtracting the last two equations (A.44) and (A.45) and making use of boundary condition equations (A.38) with the expressions for n_+^l (A.42)

and n_{-}^{r} (A.43) we have the following set of equalities,

$$\begin{aligned} V^l - V^r = \\ -\Delta V - \frac{j_e}{4\delta}\left(1+\frac{1}{\alpha}\right) + \log\left(\frac{\alpha\,(2\delta)^2}{(1-\Delta n/2)\,(1+\Delta n/2)}\right) = \\ \log\left(2\alpha\delta\right) - \log\left(-\frac{j_s+j_e}{4} + \frac{(1-\Delta n/2)^2}{2\delta}\right) = \\ \log\left(2\delta\right) - \log\left(\frac{j_s-j_e}{4} + \frac{(1+\Delta n/2)^2}{2\alpha\delta}\right) \end{aligned} \tag{A.46}$$

The last two equations allows us to arrive to a relation between the electric and solute fluxes

$$j_e = \frac{1}{\alpha-1}\left((\alpha+1)j_s + \frac{4\Delta n}{\delta}\right) \tag{A.47}$$

Or in a more general way, letting the concentrations of the reservoirs take any value n_L,n_R,

$$j_e = \frac{1}{\alpha-1}\left((\alpha+1)j_s - \frac{4}{\delta}(n_L-n_R)\right). \tag{A.48}$$

Moreover, in the limit $\delta \gg 1$, the term $\frac{j_e}{4\delta}\left(1+\frac{1}{\alpha}\right)$ in equation (A.46) can be neglected to obtain an explicit approximate expression for the solute flux in terms of the concentration imbalance of the reservoirs and the electric potential:

$$j_s = \frac{-2\Delta n}{\delta} - \frac{\alpha-1}{\alpha\delta}\left(1-\left(\frac{\Delta n}{2}\right)^2\right)\left(e^{+\Delta V} - \frac{2+\Delta n}{2-\Delta n}\right) \tag{A.49}$$

$$j_s = \frac{-2\Delta n}{\delta} - \frac{\alpha-1}{\alpha\delta}\left(1-\left(\frac{\Delta n}{2}\right)^2\right)\left(e^{+\Delta V} - \frac{2+\Delta n - n_R n_L}{4 n_L n_R}\right) \tag{A.50}$$

$$j_s = \frac{-2\Delta n}{\delta} - \frac{\alpha-1}{\alpha\delta}\left(1-\left(\frac{\Delta n}{2}\right)^2\right)\left(e^{+\Delta V} - \frac{n_R}{n_L}\right) \tag{A.51}$$

or

$$j_s = 2\frac{n_L-n_R}{\delta} - \frac{\alpha-1}{\alpha\delta} n_R\left(n_L e^{+\Delta V} - n_R\right) \tag{A.52}$$

It is worth noting that in the regime $\Delta V \gg 1$, i.e. $eV/k_BT \gg 1$ in real units, the logarithms in equation (A.46) become negligible compared to the ΔV contribution and we recover a linear regime $j_e = -4\delta\Delta V/\left(1+1/\alpha\right)$ where surface conduction dominates. This means that the exponential regime

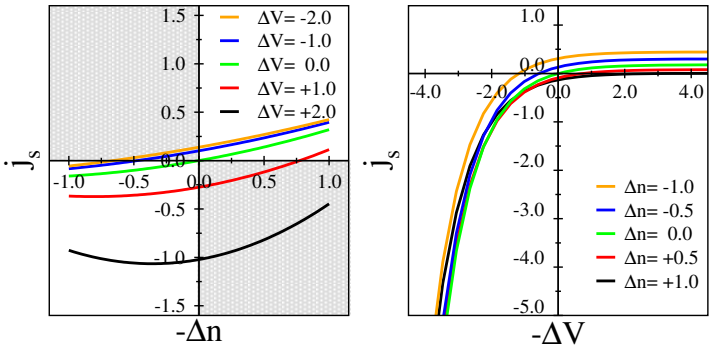

FIGURE A.2: Theoretical solute flux versus the concentration difference and the external voltage imposed between the two reservoirs, obtained from Eq. (A.52).

(A.51) is only valid for low values of ΔV.

Comparison with the numerical solution of the full PNP equations

To check the validity of our simple analytical theory, we can make use of a finite elements (FE) method to solve the Nernst-Planck transport equations (A.1) along with the electroneutrality condition. Instead of using the much more restrictive local electroneutrality ansatz that we used in the theory, here we can numerically solve the full Poisson equation instead.

$$\nabla^2 V = \begin{cases} -(1/\lambda_D)^2 (n_+ - n_-)/2, & x < -1/2 \\ -(1/\lambda_D)^2 (n_+ - n_- + \delta)/2, & -1/2 < x < 0 \\ -(1/\lambda_D)^2 (n_+ - n_- - \alpha\delta)/2, & 0 < x < 1/2 \\ -(1/\lambda_D)^2 (n_+ - n_-)/2, & 1/2 < x \end{cases}$$

This allows us to compare our theoretical predictions for large δ with the numerical solution of the full equations and also with the molecular dynamics simulations results. Since we are working in a regime of Debye length overlap we assume that the ion concentration will be approximately constant in the cross section of the channel and hence we will use 1D equations as we did in the analytical approach. As it can be observed in figure A.3, the numerical solution of the complete equations validates the theory since for large δ the two are in excellent agreement.

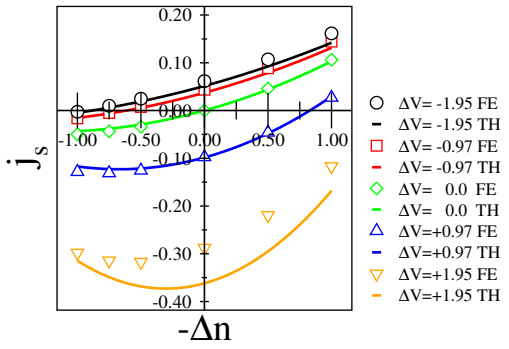

FIGURE A.3: Solute flux j_s versus salt concentration difference Δn: comparison of the FE solution of the full equations and the analytical approximation for large δ.

Analytical solution for a symmetric channel

It is interesting to note that the complex osmotic phenomena that appear are advantageous due to the charge discontinuity in the channel. The performance of this device to produce asymmetric controllable flow can be compared to the one obtained by simple charged nanochannels. To visualize this, we can compare it against the behavior of a simple symmetric pore of Dukhin number δ. Following the same procedure as before, we obtain the expressions of the solute and electric flux for this simpler setup:

$$j_s = 2\delta \left[+\Delta V + \log\left(\frac{n_L}{n_R}\right) + \frac{n_L^2 - n_R^2}{2\delta^2} \right] \tag{A.53}$$

$$j_e = 2\delta \left[-\Delta V - \log\left(\frac{n_L}{n_R}\right) \right] \tag{A.54}$$

In figure A.4 we compare the analytical solutions for the flux through a simple pore. In fact in the symmetric case we can get flux against the expected solute gradient. However, in this setup, a continuous current would be necessary to rectify the solute flux, which is not usually achievable in experiments, since it usually causes problems of polarization in the electrodes.

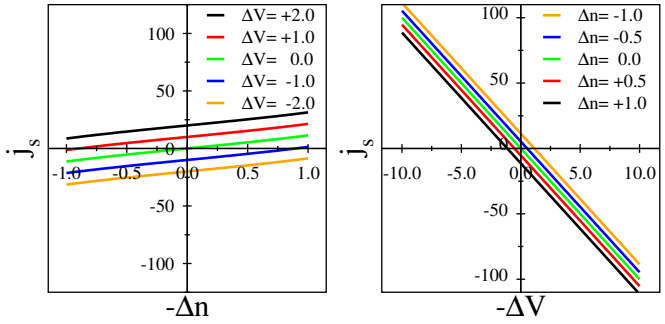

FIGURE A.4: Solute flux in terms of the osmotic gradient (left) and applied voltage (right) for a symmetric positively charged channel, obtained from Eq. (A.53).

Appendix B

Detailed theory: fluctuations in infinite nanotube

Theory: general case – Let us consider N charge carriers (ions or protons) in a cylindrical pore of length L and radius a. Each ion undergoes consecutive surface adsorption and desorption events, we introduce a binary adsorption state variable $n_A^i(t)$ for each ion $i = 1...N$ that is $n_A^i(t)$=1 when the ion is adsorbed and $n_A^i(t)$=0 when the ion is desorbed. The number of adsorbed ions at any time t follows as

$$N_A(t) = \sum_{i=1}^{N} n_A^i(t). \tag{B.1}$$

The auto-correlation function of N_A(t) writes

$$R_{N_A}(0,t) = \langle N_A(0)N_A(t)\rangle = \sum_{i,j=1}^{N} \left\langle n_A^i(0)n_A^j(t)\right\rangle . \tag{B.2}$$

If the ions are uncorrelated among each other, one can write:

$$R_{N_A}(0,t) = \sum_{i\neq j}^{N} \left\langle n_A^i(0)\right\rangle \left\langle n_A^j(t)\right\rangle + \sum_{i=1}^{N} \left\langle n_A^i(0)n_A^i(t)\right\rangle . \tag{B.3}$$

Defining the probability for an ion to be adsorbed as

$$p_A = \left\langle n_A^i(0)\right\rangle = \left\langle n_A^j(t)\right\rangle \tag{B.4}$$

we can rewrite the auto-correlation function as

$$R_{N_A}(0,t) = N^2 p_A^2 + N p_A C_{AA}(t) - N p_A^2 \tag{B.5}$$

where the single-ion correlation function

$$C_{AA}(t) = \langle n_A(0) n_A(t) \rangle \,/\, \langle n_A(0) \rangle \tag{B.6}$$

denotes the conditional probability that an ion is adsorbed at time t given that it was adsorbed at time t=0. Similarly, the autocorrelation function of the number of desorbed ions $N_D(t) = N - N_A(t)$ can be written as

$$R_{N_D}(0,t) = \langle N_D(0) N_D(t) \rangle \tag{B.7}$$

$$= \langle [N - N_A(t)][N - N_A(t)] \rangle \tag{B.8}$$

$$= N^2(1-p_A)^2 + N p_A C_{AA}(t) - N p_A^2$$

So the only non-trivial quantity to calculate is the single-ion correlation function C_{AA}(t). The probability for an ion to be adsorbed at time t given that it is adsorbed at time t=0 can be written as

$$C_{AA}(t) = \sum_{n=0}^{\infty} \left[\int_0^{\infty} dt_e Q(t_e) \prod_{m=1}^{n} \left[\int_0^{\infty} dt_m P(t_m) \int_0^{\infty} dt'_m J(t'_m) \right] \right. \tag{B.9}$$
$$\left. \times \delta \left(t_e + \sum_{k=1}^{n} (t_k + t'_k) - t \right) \right]$$

where the outer sum counts the number of desorption and re-adsorption events. The distribution $P(t)$ is the probability for an adsorbed ion to desorb from the surface at time t. We assume an exponential desorption distribution

$$P(t) = \lambda \mathrm{e}^{-\lambda t} \tag{B.10}$$

with λ in inverse time unit. Then it's Laplace transform $P(\omega) = \int_0^{\infty} \exp(-\omega t) P(t)$ writes

$$\tilde{P}(\omega) = \frac{\lambda}{\lambda + \omega}. \tag{B.11}$$

The probability for an ion to be absorbed at t, called the survival distribution $Q(t)$ is the probability for an ion to be adsorbed over the time span from

t =0 to t and is given by

$$Q(t) = \int_t^\infty dt' P(t'). \tag{B.12}$$

In our case, it writes:

$$Q(t) = \mathrm{e}^{-\lambda t} \tag{B.13}$$

and it's Laplace transform is

$$\tilde{Q}(\omega) = \frac{1}{\lambda + \omega}. \tag{B.14}$$

Finally, the first-return distribution $J(t)$ is the probability for an ion that has been desorbed at time zero to return to the cylinder surface for the first time at t. Note the different physical units of the distributions, $P(t)$ and $J(t)$ have units of inverse time, $Q(t)$ by virtue of equation (B.12) is unit-less, and the probability $C_{AA}(\mathrm{t})$ is unit-less because of the delta function. By means of Laplace transformation the correlation function factorizes into a geometric sum as

$$\tilde{C}_{AA}(\omega) = \sum_{n=0}^{\infty} \left(\tilde{Q}(\omega) \left[\tilde{P}(\omega) \tilde{J}(\omega) \right]^n \right) = \frac{\tilde{Q}(\omega)}{1 - \tilde{P}(\omega)\tilde{J}(\omega)} \tag{B.15}$$

Determination of $J(\omega)$ for an infinite tube – An expression for $J(\omega)$ is needed. Since $J(\omega)$ is the Laplace transform of the probability for a desorbed ion to return to the cylinder surface, it strongly depends on the geometry. Inside an infinite cylindrical tube, the diffusion equation in cylindrical coordinates as to be solved. The radially symmetric Green's function for an ion to be at time t at a radius r when starting at a radius r_0 obeys the radial diffusion equation in cylindrical coordinates

$$\partial_t \mathcal{G}(r, t|r_0) = D \triangle_r \mathcal{G}(r, t|r_0) = D \frac{1}{r} \partial_r r \partial_r \mathcal{G}(r, t|r_0) \tag{B.16}$$

where D denotes the diffusion constant. The Laplace transformed equation reads

$$\omega \tilde{\mathcal{G}}(r, \omega|r_0) - \frac{\delta(r - r_0)}{2\pi r} = D \frac{1}{r} \partial_r r \partial_r \tilde{\mathcal{G}}(r, \omega|r_0) \tag{B.17}$$

where we used the initial condition

$$\tilde{\mathcal{G}}(r, t = 0|r_0) = \frac{\delta(r - r_0)}{2\pi r}. \tag{B.18}$$

Using the rescaled radial coordinate

$$\tilde{r} = r\sqrt{\omega/D} \tag{B.19}$$

the equation can be brought into the canonical form of a Bessel differential equation

$$\frac{\tilde{r}}{2\pi D}\delta(\tilde{r} - \tilde{r}_0) = \tilde{r}^2\tilde{\mathcal{G}}(r, \omega|r_0) - \tilde{r}\partial_r\tilde{\mathcal{G}}(r, \omega|r_0) - \tilde{r}^2\partial_r^2\tilde{\mathcal{G}}(r, \omega|r_0). \tag{B.20}$$

The general solution is

$$\tilde{\mathcal{G}}(\tilde{r}, \omega|\tilde{r}_0) = aI_0(\tilde{r}) \tag{B.21}$$

for $\tilde{r} < \tilde{r}_0$ and

$$\tilde{\mathcal{G}}(\tilde{r}, \omega|\tilde{r}_0) = bI_0(\tilde{r}) + cK_0(\tilde{r}) \tag{B.22}$$

for $\tilde{r} > \tilde{r}_0$ where $I_0(x)$ and $K_0(x)$ are modified Bessel functions. The coefficients a, b, c are determined by the following three boundary conditions:

(BC1) continuity at $\tilde{r} = \tilde{r}_0$:

$$aI_0(\tilde{r}_0) = bI_0(\tilde{r}_0) + cK_0(\tilde{r}_0), \tag{B.23}$$

(BC2) initial condition of equation (B.20), obtained by the integration of equation (B.17) between r_0^- and r_0^+:

$$\frac{1}{2\pi D\tilde{r}_0} = aI_1(\tilde{r}_0) - bI_1(\tilde{r}_0) + cK_1(\tilde{r}_0) \tag{B.24}$$

where $\partial_x I_0(x) = I_1(x)$ and $\partial_x K_0(x) = -K_1(x)$,

(BC3) a surface reaction boundary condition at $r = R$ which in unrescaled units reads

$$j(R, \omega|r_0) = -D\partial_R\tilde{\mathcal{G}}(R, \omega|\tilde{r}_0) = k\tilde{\mathcal{G}}(R, \omega|\tilde{r}_0) \tag{B.25}$$

and reflects that the ion boundary flux $j(R, \omega|r_0)$ is proportional to the ion boundary density times a phenomenological rate constant k. In rescaled

radial units and using $k = \tilde{k}\sqrt{\omega D}$ this condition reads

$$\partial_R \tilde{\mathcal{G}}(R, \omega|\tilde{r}_0) = -\tilde{k}\tilde{\mathcal{G}}(R, \omega|\tilde{r}_0) \tag{B.26}$$

which explicitly yields

$$bI_1(\tilde{R}) - cK_1(\tilde{R}) = -k\left[bI_0(\tilde{r}_0) + cK_0(\tilde{r}_0)\right] \tag{B.27}$$

Introducing rescaled coefficients $\tilde{a} = 2\pi D\tilde{r}_0 a$ (and similarly for b and c) we arrive at the final boundary conditions

$$\tilde{a}I_0(\tilde{r}_0) = \tilde{b}I_0(\tilde{r}_0) + \tilde{c}K_0(\tilde{r}_0) \tag{B.28}$$

$$1 = \tilde{a}I_1(\tilde{r}_0) - \tilde{b}I_1(\tilde{r}_0) + \tilde{c}K_1(\tilde{r}_0) \tag{B.29}$$

$$\tilde{b}I_1(\tilde{R}) - \tilde{c}K_1(\tilde{R}) = -\tilde{k}\left[\tilde{b}I_0(\tilde{R}) + \tilde{c}K_0(\tilde{R})\right] \tag{B.30}$$

The solutions for $\tilde{b}$ and $\tilde{c}$ read

$$\tilde{c} = \frac{I_0(\tilde{r}_0)}{K_0(\tilde{r}_0)I_1(\tilde{r}_0) + K_1(\tilde{r}_0)I_0(\tilde{r}_0)} \tag{B.31}$$

and

$$\tilde{b} = \tilde{c}\left(\frac{K_1(\tilde{R}) - \tilde{k}K_0(\tilde{R})}{I_1(\tilde{R}) + \tilde{k}I_0(\tilde{R})}\right) \tag{B.32}$$

For the total flux at the cylinder surface we obtain combining Eqs. (B.22) and (B.23)

$$\begin{aligned} 2\pi R j(R, \omega|r_0) &= 2\pi Rk\left[bI_0(\tilde{R}) + cK_0(\tilde{R})\right] \\ &= \frac{\tilde{k}\tilde{R}}{\tilde{r}_0}\left[\tilde{b}I_0(\tilde{R}) + \tilde{c}K_0(\tilde{R})\right] \end{aligned} \tag{B.33}$$

The first-return distribution follows as

$$\begin{aligned} J(\omega) &= 2\pi R j(R, \omega|R) \\ &= \tilde{k}\left[\tilde{b}(\tilde{r}_0 = \tilde{R})I_0(\tilde{R}) + \tilde{c}(\tilde{r}_0 = \tilde{R})K_0(\tilde{R})\right] \\ &= \frac{\tilde{k}I_0(\tilde{R})}{I_1(\tilde{R}) + \tilde{k}I_0(\tilde{R})} \end{aligned} \tag{B.34}$$

Connection to the law of mass action – In order to calculate the

probability for an ion to be absorbed, we need to construct the conditional probability that an ion that was absorbed at time $t = 0$ is desorbed at time t

$$C_{\mathrm{AD}}(t) = \langle n_A(0)(1 - n_A(t))\rangle \,/\, \langle n_A(0)\rangle \,. \tag{B.35}$$

Similarly to our previous construction, we obtain

$$C_{AD}(t) = \sum_{n=0}^{\infty} \left[\int_0^\infty dt_e P(t_e) \int_0^\infty dt'_e J_D(t'_e) \prod_{m=1}^{n} \left[\int_0^\infty dt_m P(t_m) \int_0^\infty dt'_m J(t'_m) \right] \right.$$
$$\left. \times \delta \left(t_e + t'_e + \sum_{k=1}^{n} (t_k + t'_k) - t \right) \right] \tag{B.36}$$

We have indroduced the probability distribution $J_D(t)$ for an ion to be desorbed over the entire time span from $t = 0$ to t, which follows from the first-return probability $J(t)$ via

$$J_D(t) = \int_t^\infty dt' J(t'). \tag{B.37}$$

After Laplace transformation the correlation function follows as

$$\begin{aligned} \tilde{C}_{AD}(\omega) &= \sum_{n=0}^{\infty} \left(\tilde{P}(\omega)\tilde{J}_D(\omega) \left[\tilde{P}(\omega)\tilde{J}(\omega) \right]^n \right) \\ &= \frac{\tilde{P}(\omega)\tilde{J}_D(\omega)}{1 - \tilde{P}(\omega)\tilde{J}(\omega)} \end{aligned} \tag{B.38}$$

The probabilities for an ion being absorbed versus being desorbed can be obtained from the Laplace transformed correlation functions $\tilde{C}_{AA}(\omega)$ and $\tilde{C}_{AD}(\omega)$ in the limit $\omega \to 0$. From

$$\tilde{J}_D(\omega) = \frac{\tilde{J}(\omega = 0) - \tilde{J}(\omega)}{\omega} \tag{B.39}$$

and using that, for small frequencies:

$$\tilde{J}^{-1}(\omega) \approx 1 + \frac{\omega a}{2k} \tag{B.40}$$

we obtain

$$\tilde{J}_D(\omega \to 0) = \frac{a}{2k}. \tag{B.41}$$

With Eq. B.38 we obtain

$$\frac{\tilde{C}_{AA}(\omega=0)}{\tilde{C}_{AD}(\omega=0)} = \frac{\tilde{Q}(\omega=0)}{\tilde{P}(\omega=0)\tilde{J}_D(\omega=0)} = \frac{\tau}{a/2k} = \frac{2k}{\lambda a}. \tag{B.42}$$

For the ratio of ion surface concentration and bulk concentration we obtain the law of mass action

$$\frac{\tilde{C}_{AA}(\omega=0)/(2\pi a)}{\tilde{C}_{AD}(\omega=0)/(\pi a^2)} = k/\lambda. \tag{B.43}$$

The equilibrium reaction constant is thus shown to be proportional to the product of the surface reaction rate k and the mean adsorption time τ and agrees with the planar case (to be published).

Bibliography

1. Gravelle, S. *Nanofluidics: A pedagogical introduction.* 2016.
2. Bocquet, L. & Charlaix, E. "Nanofluidics, from bulk to interfaces." *Chemical Society reviews* **39,** 1073–1095 (2010).
3. Eijkel, J. C. T. & van den Berg, A. "Nanofluidics: What is it and what can we expect from it?" *Microfluidics and Nanofluidics* **1,** 249–267 (2005).
4. Spiegler, K. & Kedem, O. "Thermodynamics of hyperfiltration (reverse osmosis): criteria for efficient membranes". *Desalination* **1,** 311–326 (1966).
5. Morrison, F. A. & Osterle, J. F. "Electrokinetic Energy Conversion in Ultrafine Capillaries". *The Journal of Chemical Physics* **43** (1965).
6. Gross, R. J. & Osterle, J. F. "Membrane Transport Characteristics of Ultrafine Capillaries". *The Journal of Chemical Physics* **49** (1968).
7. Fair, J. C. & Osterle, J. F. "Reverse Electrodialysis in Charged Capillary Membranes". *The Journal of Chemical Physics* **54** (1971).
8. Hoffer, E & Kedem, O. "Hyperfiltration in charged membranes: the fixed charge model". *Desalination* **2,** 25–39 (1967).
9. Bocquet, L. & Tabeling, P. "Physics and technological aspects of nanofluidics." *Lab on a chip* **14,** 3143–58 (2014).
10. Majumder, M., Chopra, N., Andrews, R & Hinds, B. J. "Enhanced flow in carbon nanotubes". *Nature* **438,** 44 (2005).
11. Holt, J. K. *et al.* "Fast mass transport through sub-2-nanometer carbon nanotubes." *Science (New York, N.Y.)* **312,** 1034–1037 (2006).

12. Whitby, M., Cagnon, L., Thanou, M. & Quirke, N. "Enhanced fluid flow through nanoscale carbon pipes". *Nano Letters* **8,** 2632–2637 (2008).

13. Daiguji, H., Oka, Y. & Shirono, K. "Nanofluidic diode and bipolar transistor". *Nano Letters* **5,** 2274–2280 (2005).

14. Deng, D. *et al.* "Overlimiting current and shock electrodialysis in porous media". *Langmuir* **29,** 16167–16177 (2013).

15. Bocquet, L. & Barrat, J. L. "Flow boundary conditions from nano- to micro-scales". *Soft Matter* **3,** 685–693 (2006).

16. De Groot, B. L. & Grubmüller, H. "Water permeation across biological membranes: mechanism and dynamics of aquaporin-1 and GlpF." *Science (New York, N.Y.)* **294,** 2353–2357 (2001).

17. Agre, P. "Aquaporin water channels". *Bioscience Reports* **24,** 127–163 (2005).

18. Mijatovic, D, Eijkel, J. C. T. & van den Berg, a. "Technologies for nanofluidic systems: top-down vs. bottom-up–a review." *Lab on a chip* **5,** 492–500 (2005).

19. Dekker, C. "Solid-state nanopores." *Nature nanotechnology* **2,** 209–215 (2007).

20. Hemamouche, A. *et al.* "FIB patterning of dielectric, metallized and graphene membranes: A comparative study". *Microelectronic Engineering* **121,** 87–91 (2014).

21. Chen, P. *et al.* "Atomic layer deposition to fine-tune the surface properties and diameters of fabricated nanopores". *Nano Letters* **4,** 1333–1337 (2004).

22. Karnik, R., Duan, C., Castelino, K., Daiguji, H. & Majumdar, A. "Rectification of ionic current in a nanofluidic diode". *Nano Letters* **7,** 547–551 (2007).

23. Siria, A. *et al.* "Giant osmotic energy conversion measured in a single transmembrane boron nitride nanotube." *Nature* **494,** 455–8 (2013).

24. Cuenca, A. & Bodiguel, H. "Fluorescence photobleaching to evaluate flow velocity and hydrodynamic dispersion in nanoslits". *Lab on a Chip* **12,** 1672 (2012).

25. Lee, C. *et al.* "Osmotic flow through fully permeable nanochannels". *Physical Review Letters* **112,** 244501 (2014).

26. Gadaleta, A., Biance, A.-L., Siria, A. & Bocquet, L. "Ultra-sensitive flow measurement in individual nanopores through pressure–driven particle translocation". *Nanoscale* **7,** 7965–7970 (2015).

27. Tocci, G., Joly, L. & Michaelides, A. "Friction of water on graphene and hexagonal BN from ab initio methods : very different slippage despite very similar interface structures". *Nano letters* **submitted** (2014).

28. Cohen-Tanugi, D. & Grossman, J. C. "Water desalination across nanoporous graphene". *Nano Letters* **12,** 3602–3608 (2012).

29. Nicholls, W. D., Borg, M. K., Lockerby, D. a. & Reese, J. M. "Water transport through (7,7) carbon nanotubes of different lengths using molecular dynamics". *Microfluidics and Nanofluidics* **12,** 257–264 (2012).

30. Borgnia, M., Nielsen, S., Engel, A. & Agre, P. "Cellular and Molecular Biology of the Aquaporin Water Channels". *Annual Review of Biochemistry* **68,** 425–458 (1999).

31. Mathé, J., Aksimentiev, A., Nelson, D. R., Schulten, K. & Meller, A. "Orientation discrimination of single-stranded DNA inside the alpha-hemolysin membrane channel." *Proceedings of the National Academy of Sciences of the United States of America* **102,** 12377–82 (2005).

32. Verkman, A. S. "Role of aquaporin water channels in eye function". *Experimental Eye Research* **76,** 137–143 (2003).

33. Glynn, I. M. "Annual review prize lecture. 'All hands to the sodium pump'." *The Journal of physiology* **462,** 1–30 (1993).

34. Gouaux, E. & Mackinnon, R. "Principles of selective ion transport in channels and pumps." *Science (New York, N.Y.)* **310,** 1461–1465 (2005).

35. Ben Amar, N., Saidani, H., Deratani, a. & Palmeri, J. "Effect of temperature on the transport of water and neutral solutes across nanofiltration membranes". *Langmuir* **23,** 2937–2952 (2007).

36. Humplik, T *et al.* "Nanostructured materials for water desalination." *Nanotechnology* **22,** 292001 (2011).

37. Fritzmann, C., Löwenberg, J., Wintgens, T. & Melin, T. "State-of-the-art of reverse osmosis desalination". *Desalination* **216,** 1–76 (2007).

38. Cath, T. Y., Childress, A. E. & Elimelech, M. "Forward osmosis: Principles, applications, and recent developments". *Journal of Membrane Science* **281,** 70–87 (2006).

39. Scheumann, R. & Kraume, M. "Influence of different HRT for the operation of a Submerged Membrane Sequencing Batch Reactor (SM-SBR) for the treatment of greywater". *Desalination* **248,** 123–130 (2009).

40. Achilli, A., Cath, T. Y. & Childress, A. E. "Power generation with pressure retarded osmosis: An experimental and theoretical investigation". *Journal of Membrane Science* **343,** 42–52 (2009).

41. Guan, W., Fan, R. & Reed, M. a. "Field-effect reconfigurable nanofluidic ionic diodes". *Nature Communications* **2,** 506 (2011).

42. Batsanov, S. "Van der Waals radii of elements". *Inorganic materials* **37,** 871–885 (2001).

43. Schoch, R. B., Han, J. & Renaud, P. "Transport phenomena in nanofluidics". *Reviews of Modern Physics* **80,** 839–883 (2008).

44. Boroudjerdi, H. *et al.* "Statics and dynamics of strongly charged soft matter". *Physics Reports* **416,** 129–199 (2005).

45. Joly, L., Ybert, C. & Bocquet, L. "Probing the nanohydrodynamics at liquid-solid interfaces using thermal motion". *Physical Review Letters* **96,** 46101 (2006).

46. Andelman, D. "Chapter 12 Electrostatic properties of membranes: The poisson-boltzmann theory". *Handbook of Biological Physics* **1,** 603–642 (1995).

47. Israelachvili, J. N. *Intermolecular and Surface Forces: Revised Third Edition* (ed Eselvier) (Academic press, 2011).

48. Clapham, D. E. "Symmetry, Selectivity, and the 2003 Nobel Prize". *Cell* **115,** 641–646 (2003).

49. De Gennes, P.-G., Brochard-Wyart, F. & Quéré, D. *Capillarity and wetting phenomena: drops, bubbles, pearls, waves* (Springer Science & Business Media, 2013).

50. "The Collected Works of J. Willard Gibbs. Two volumes". *Journal of Chemical Education* **6,** 591 (1929).

51. Kedem, O. & Katchalsky, A. "Permeability of Composite Membranes". *Transactions of the Faraday Society* **59,** 1918–1939 (1962).

52. Plecis, A., Schoch, R. B. & Renaud, P. "Ionic transport phenomena in nanofluidics: Experimental and theoretical study of the exclusion-enrichment effect on a chip". *Nano Letters* **5,** 1147–1155 (2005).

53. Daiguji, H., Yang, P. & Majumdar, A. "Ion Transport in Nanofluidic Circuits". *Nano letters* **4,** 47405 (2004).

54. Van Der Heyden, F. H. J., Stein, D. & Dekker, C. "Streaming currents in a single nanofluidic channel". *Physical Review Letters* **95,** 116104 (2005).

55. Anderson, J. "Colloid Transport By Interfacial Forces". *Annual Review of Fluid Mechanics* **21,** 61–99 (1989).

56. Prieve, D. C., Anderson, J. L., Ebel, J. P. & Lowell, M. E. "Motion of a particle generated by chemical gradients. Part 2. Electrolytes". *Journal of Fluid Mechanics* **148,** 247 (1984).

57. Lee, J., Laoui, T. & Karnik, R. "Nanofluidic transport governed by the liquid/vapour interface." *Nature nanotechnology* **9,** 317–23 (2014).

58. Siria, A. *et al.* "Supplementary information: Giant osmotic energy conversion measured in a single transmembrane boron nitride nanotube." *Nature* **494,** 455–8 (2013).

59. Gravelle, S. & Ybert, C. "Flow-Induced Shift of the Donnan Equilibrium for Ultra-Sensitive Mass Transport Measurement Through a Single Nanochannel". *arXiv preprint arXiv:1910.13126* (2019).

60. Gravelle, S. *et al.* "Optimizing water permeability through the hourglass shape of aquaporins." *Proceedings of the National Academy of Sciences of the United States of America* **110,** 16367–72 (2013).

61. Gravelle, S., Joly, L., Ybert, C. & Bocquet, L. "Large permeabilities of hourglass nanopores : From hydrodynamics to single file transport". *The Journal of Chemical Physics* **141,** 18C526 (2014).

62. Gravelle, S. *et al.* "Perméabilité optimale des aquaporines: Une histoire de forme?" *Medecine/Sciences* **31,** 174–9 (2015).

63. Sampson, R. A. "On Stokes's Current Function". *Philosophical Transactions of the Royal Society A: Mathematical, Physical and Engineering Sciences* **182,** 449–518 (1891).

64. Weissberg, H. L. "End Correction for Slow Viscous Flow through Long Tubes". *Physics of Fluids* **5,** 1033 (1962).

65. Dagan, Z., Weinbaum, S. & Pfeffer, R. "An infinite-series solution for the creeping motion through an orifice of finite length". *Journal of Fluid Mechanics* **115,** 505 (1982).

66. Majumder, M., Chopra, N. & Hinds, B. J. "Mass transport through carbon nanotube membranes in three different regimes: Ionic diffusion and gas and liquid flow". *ACS Nano* **5,** 3867–3877 (2011).

67. Du, F., Qu, L., Xia, Z., Feng, L. & Dai, L. "Membranes of vertically aligned superlong carbon nanotubes". *Langmuir* **27,** 8437–8443 (2011).

68. Sisan, T. B. & Lichter, S. "The end of nanochannels". *Microfluidics and Nanofluidics* **11,** 787–791 (2011).

69. Falk, K., Sedlmeier, F., Joly, L., Netz, R. R. & Bocquet, L. "Molecular origin of fast water transport in carbon nanotube membranes: Superlubricity versus curvature dependent friction". *Nano Letters* **10,** 4067–4073 (2010).

70. Suk, M. E. & Aluru, N. R. "Water transport through ultrathin graphene". *Journal of Physical Chemistry Letters* **1,** 1590–1594 (2010).

71. Happel, J & Brenner, H. *Low Reynolds number hydrodynamics* (Martinus Nijhoff Publishers, 1973).

72. Joly, L. "Capillary filling with giant liquid/solid slip: Dynamics of water uptake by carbon nanotubes". *Journal of Chemical Physics* **135** (2011).

73. Bernstein, F. C. *et al.* "The Protein Data Bank. A computer-based archival file for macromolecular structures." *European journal of biochemistry / FEBS* **80,** 319–324 (1977).

74. Humphrey, W., Dalke, A. & Schulten, K. "VMD – Visual Molecular Dynamics". *J. Molec. Graphics* **14,** 33–38 (1996).

75. Ho, J. D. *et al.* "Crystal structure of human aquaporin 4 at 1.8 A and its mechanism of conductance." *Proceedings of the National Academy of Sciences of the United States of America* **106,** 7437–7442 (2009).

76. Smart, O. S., Neduvelil, J. G., Wang, X., Wallace, B. a. & Sansom, M. S. P. "HOLE: A program for the analysis of the pore dimensions of ion channel structural models". *Journal of Molecular Graphics* **14,** 354–360 (1996).

77. Hashido, M., Kidera, A. & Ikeguchi, M. "Water transport in aquaporins: osmotic permeability matrix analysis of molecular dynamics simulations." *Biophysical journal* **93,** 373–385 (2007).

78. Finkelsteinrsen, A. & Ande, O. S. "The gramicidin a channel: A review of its permeability characteristics with special reference to the single-file aspect of transport". *The Journal of Membrane Biology* **59,** 155–171 (1981).

79. Bocquet, L. & Barrat, J. L. "Hydrodynamic boundary conditions, correlation functions, and Kubo relations for confined fluids". *Physical Review E* **49,** 3079–3092 (1994).

80. Cornell, W. D. *et al.* "A 2nd Generation Force-Field for the Simulation of Proteins, Nucleic-Acids, and Organic-Molecules". *J. Am. Chem. Soc.* **117,** 5179–5197 (1995).

81. Jorgensen, W. L., Chandrasekhar, J., Madura, J. D., Impey, R. W. & Klein, M. L. "Comparison of simple potential functions for simulating liquid water". *The Journal of Chemical Physics* **79,** 926 (1983).

82. Plimpton, S. "Fast Parallel Algorithms For Short-range Molecular-dynamics". *J. Comp. Phys.* **117,** 1–19 (1995).

83. Darden, T., York, D. & Pedersen, L. "Particle mesh Ewald: An N log(N) method for Ewald sums in large systems". *The Journal of Chemical Physics* **98,** 10089 (1993).

84. Lu, Q. & Luo, R. "A Poisson-Boltzmann dynamics method with nonperiodic boundary condition". *Journal of Chemical Physics* **119,** 11035–11047 (2003).

85. Ryckaert, J.-P., Ciccotti, G. & Berendsen, H. J. "Numerical integration of the cartesian equations of motion of a system with constraints: molecular dynamics of n-alkanes". *Journal of Computational Physics* **23,** 327–341 (1977).

86. Groot, R. D. & Warren, P. B. "Dissipative particle dynamics: Bridging the gap between atomistic and mesoscopic simulation". *The Journal of Chemical Physics* **107,** 4423 (1997).

87. Alexiadis, A. & Kassinos, S. "Molecular Simulation of Water in Carbon Nanotubes". *Chemical Reviews* **30,** 5014–5034 (2008).

88. Thomas, J. a. & McGaughey, A. J. H. "Water flow in carbon nanotubes: Transition to subcontinuum transport". *Physical Review Letters* **102,** 184502 (2009).

89. Werder, T *et al.* "On the Water - Carbon Interaction for Use in Molecular Dynamics Simulations of Graphite and Carbon Nanotubes". *Journal of Physical Chemistry B* **107,** 1345–1352 (2003).

90. Huang, D. M., Cottin-Bizonne, C., Ybert, C. & Bocquet, L. "Massive amplification of surface-induced transport at superhydrophobic surfaces". *Physical Review Letters* **101,** 064503 (2008).

91. Sender, C., Horinek, D., Bocquet, L. & Netz, R. R. "Interfacial water at hydrophobic and hydrophilic surfaces: Slip, viscocity, and diffusion". *Langmuir* **25,** 10768–10781 (2009).

92. Wu, Y., Tepper, H. L. & Voth, G. a. "Flexible simple point-charge water model with improved liquid-state properties." *The Journal of chemical physics* **124,** 024503 (2006).

93. Jensen, M. Ø., Park, S., Tajkhorshid, E. & Schulten, K. "Energetics of glycerol conduction through aquaglyceroporin GlpF." *Proceedings of the National Academy of Sciences of the United States of America* **99,** 6731–6736 (2002).

94. Zhu, F., Tajkhorshid, E. & Schulten, K. "Theory and simulation of water permeation in aquaporin-1." *Biophysical journal* **86,** 50–57 (2004).

95. Murata, K *et al.* "Structural determinants of water permeation through aquaporin-1." *Nature* **407,** 599–605 (2000).

96. Sui, H, Han, B. G., Lee, J. K., Walian, P & Jap, B. K. "Structural basis of water-specific transport through the AQP1 water channel." *Nature* **414,** 872–878 (2001).

97. Rasaiah, J. C., Garde, S. & Hummer, G. "Water in nonpolar confinement: from nanotubes to proteins and beyond." *Annual review of physical chemistry* **59,** 713–740 (2008).

98. Cui, Y. & Bastien, D. a. "Water transport in human aquaporin-4: Molecular dynamics (MD) simulations". *Biochemical and Biophysical Research Communications* **412,** 654–659 (2011).

99. De Groot, B. L., Engel, A. & Grubmüller, H. "The structure of the aquaporin-1 water channel: A comparison between cryo-electron microscopy and X-ray crystallography". *Journal of Molecular Biology* **325,** 485–493 (2003).

100. Harries, W. E. C., Akhavan, D., Miercke, L. J. W., Khademi, S. & Stroud, R. M. "The channel architecture of aquaporin 0 at a 2.2-A resolution." *Proceedings of the National Academy of Sciences of the United States of America* **101,** 14045–14050 (2004).

101. Zhang, Y. B. & Chen, L. Y. "In silico study of Aquaporin V: Effects and affinity of the central pore-occluding lipid". *Biophysical Chemistry* **171,** 24–30 (2013).

102. Jensen, M. Ø. & Mouritsen, O. G. "Single-channel water permeabilities of Escherichia coli aquaporins AqpZ and GlpF." *Biophysical journal* **90,** 2270–2284 (2006).

103. Fischer, G. *et al.* "Crystal structure of a yeast aquaporin at 1.15 Å reveals a novel gating mechanism". *PLoS Biology* **7,** e1000130 (2009).

104. Suk, M. E. & Aluru, N. R. "Molecular and continuum hydrodynamics in graphene nanopores". *RSC Advances* **3,** 9365 (2013).

105. O'Hern, S. C. *et al.* "Selective ionic transport through tunable subnanometer pores in single-layer graphene membranes". *Nano Letters* **14,** 1234–1241 (2014).

106. Gravelle, S., Ybert, C., Bocquet, L. & Joly, L. "Anomalous capillary filling and wettability reversal in nanochannels". *Phys. Rev. E* **93,** 033123 (2016).

107. Young, T. "An Essay on the Cohesion of Fluids". *Philosophical Transactions of the Royal Society of London* **95,** 65–87 (1805).

108. Laplace, P.-S. "Traité de mécanique cèleste; suppléments au Livre X, 1805 and 1806 resp". *Oeuvres Complètes* **4** (1906).

109. Van Honschoten, J. W., Brunets, N. & Tas, N. R. "Capillarity at the nanoscale." *Chemical Society reviews* **39,** 1096–1114 (2010).

110. Caro, a., Schwen, D., Hetherly, J. & Martinez, E. "The capillarity equation at the nanoscale: Gas bubbles in metals". *Acta Materialia* **89,** 14–21 (2015).

111. Kim, W. & Bush, J. W. M. "Natural drinking strategies". *Journal of Fluid Mechanics* **705,** 7–25 (2012).

112. Persson, B. N. J. "Biological Adhesion for Locomotion on Rough Surfaces: Basic Principles and A Theorist's View". *MRS Bulletin* **32,** 486–490 (2007).

113. Sparreboom, W, van den Berg, a & Eijkel, J. C. T. "Principles and applications of nanofluidic transport." *Nature nanotechnology* **4,** 713–720 (2009).

114. Supple, S & Quirke, N. "Molecular dynamics of transient oil ows in nanopores I: Imbibition speeds for single wall carbon nanotubes". *Chemical Physics* **121,** 8571–8579 (2004).

115. Stange, M., Dreyer, M. E. & Rath, H. J. "Capillary driven flow in circular cylindrical tubes". *Physics of Fluids* **15,** 2587–2601 (2003).

116. Berendsen, H. J. C., Postma, J. P. M., van Gunsteren, W. F., DiNola, a & Haak, J. R. "Molecular dynamics with coupling to an external bath". *The Journal of Chemical Physics* **81,** 3684–3690 (1984).

117. Cornell, W. D. *et al.* "A second generation force field for the simulation of proteins, nucleic acids, and organic molecules". *Journal of the American Chemical Society* **117,** 5179–5197 (1995).

118. Jensen, K. H., Valente, A. X. C. N. & Stone, H. a. "Flow rate through microfilters: Influence of the pore size distribution, hydrodynamic interactions, wall slip, and inertia". *Physics of Fluids* **26,** 052004 (2014).

119. Errington, J. R. & Debenedetti, P. G. "Relationship between structural order and the anomalies of liquid water." *Nature* **409,** 318–321 (2001).

120. Daw, M. S. & Baskes, M. I. "Semiempirical, quantum mechanical calculation of hydrogen embrittlement in metals". *Physical Review Letters* **50,** 1285–1288 (1983).

121. Grochola, G., Russo, S. P. & Snook, I. K. "On fitting a gold embedded atom method potential using the force matching method." *The Journal of chemical physics* **123,** 204719 (2005).

122. Song, C. & Corry, B. "Intrinsic ion selectivity of narrow hydrophobic pores". *Journal of Physical Chemistry B* **113,** 7642–7649 (2009).

123. Corry, B. "Designing carbon nanotube membranes for efficient water desalination". *J. Phys. Chem. B* **112,** 1427–1434 (2008).

124. Pascal, T. a., Goddard, W. a. & Jung, Y. "Entropy and the driving force for the filling of carbon nanotubes with water." *Proceedings of the National Academy of Sciences of the United States of America* **108,** 11794–11798 (2011).

125. Van Honschoten, J. W., Brunets, N. & Tas, N. R. "Capillarity at the nanoscale." *Chemical Society reviews* **39,** 1096–1114 (2010).

126. Merlet, C *et al.* "Highly confined ions store charge more efficiently in supercapacitors." *Nature communications* **4,** 2701 (2013).

127. Forse, A. C. *et al.* "NMR Study of Ion Dynamics and Charge Storage in Ionic Liquid Supercapacitors". *Journal of the American Chemical Society* **137,** 7231–7242 (2015).

128. Picallo, C. B., Gravelle, S., Joly, L., Charlaix, E. & Bocquet, L. "Nanofluidic osmotic diodes: Theory and molecular dynamics simulations". *Physical Review Letters* **111,** 1–5 (2013).

129. Cheng, L.-J. & Guo, L. J. "Nanofluidic diodes." *Chemical Society reviews* **39,** 923–938 (2010).

130. Siwy, Z., Heins, E., Harrell, C. C., Kohli, P. & Martin, C. R. "Conical-nanotube ion-current rectifiers: The role of surface charge". *Journal of the American Chemical Society* **126,** 10850–10851 (2004).

131. Siwy, Z., Kosińska, I. D., Fuliński, a. & Martin, C. R. "Asymmetric diffusion through synthetic nanopores". *Physical Review Letters* **94,** 048102 (2005).

132. Siwy, Z. S. "Ion-current rectification in nanopores and nanotubes with broken symmetry". *Advanced Functional Materials* **16,** 735–746 (2006).

133. Vlassiouk, I. & Siwy, Z. S. "Nanofluidic diode." *Nano Lett.* **7,** 552–6 (2007).

134. Qu, L.-j., Zhang, X., Fu, J., Li, L. & Yan, D. "Poisson-Nernst-Planck Model of Bipolar Nanofluidic Diode Based on Bulletlike Nanopore". *Arxiv* (2013).

135. Constantin, D. & Siwy, Z. S. "Poisson Nernst-Planck Model of Ion Current Rectification through a Nanofluidic Diode". *Phys. Rev. E* **76,** 1–9 (2007).

136. Kedem, O & Katchalsky, a. "A physical interpretation of the phenomenological coefficients of membrane permeability." *The Journal of general physiology* **45,** 143–179 (1961).

137. Dydek, E. V. *et al.* "Overlimiting current in a microchannel". *Physical Review Letters* **107,** 118301 (2011).

138. Manning, G. S. "Binary Diffusion and Bulk Flow through a Potential-Energy Profile: A Kinetic Basis for the Thermodynamic Equations of Flow through Membranes". *The Journal of Chemical Physics* **49,** 2668–2675 (1968).

139. Constantin, D. & Siwy, Z. S. "Poisson-Nernst-Planck model of ion current rectification through a nanofluidic diode". *Physical Review E - Statistical, Nonlinear, and Soft Matter Physics* **76,** 1–10 (2007).

140. Vlassiouk, I., Smimov, S. & Siwy, Z. "Nanofluidic ionic diodes. Comparison of analytical and numerical solutions". *ACS Nano* **2,** 1589–1602 (2008).

141. Schneider, T. & Stoll, E. "Molecular-dynamics study of a three-dimensional one-component model for distortive phase transitions". *Physical Review B* **17,** 1302–1322 (1978).

142. Crozier, P. S., Rowley, R. L., Holladay, N. B., Henderson, D. & Busath, D. D. "Molecular dynamics simulation of continuous current flow through a model biological membrane channel". *Physical Review Letters* **86,** 2467–2470 (2001).

143. Delemotte, L., Dehez, F., Treptow, W. & Tarek, M. "Modeling membranes under a transmembrane potential". *Journal of Physical Chemistry B* **112,** 5547–5550 (2008).

144. Chen, A. A. & Pappu, R. V. "Parameters of Monovalent Ions in the AMBER-99 Forcefield: Assessment of Inaccuracies and Proposed Improvements". *The Journal of Physical Chemistry B* **111,** 11884–11887 (2007).

145. Rinne, K. F., Gekle, S., Bonthuis, D. J. & Netz, R. R. "Nanoscale pumping of water by AC electric fields". *Nano Letters* **12,** 1780–1783 (2012).

146. Kou, J. *et al.* "A vibration-charge-induced unidirectional transport of water molecules in confined nanochannels". *Soft Matter,* 12111–12115 (2012).

147. Laohakunakorn, N. *et al.* "A Landau-Squire nanojet". *Nano Letters* **13,** 5141–5146 (2013).

148. Gravelle, S., Netz, R. R. & Bocquet, L. "Adsorption Kinetics in Open Nanopores as a Source of Low-Frequency Noise". *Nano letters* **19,** 7265–7272 (2019).

149. Ward, L. M. & Greenwood, P. E. "1/f noise". *Scholarpedia* **2,** 1537 (2007).

150. Johnson, J. B. "The Schottky effect in low frequency circuits". *Physical Review* **26,** 71–85 (1925).

151. Milotti, E. *1/f noise : a pedagogical review*. 1921.

152. Cardner, M. "Mathematical Games". *Scientific American* **224,** 112–117 (1971).

153. Dutta, P & Horn, P. M. *Low-frequency fluctuations in solids: 1/f noise*. 1981.

154. Tabard-Cossa, V., Trivedi, D., Wiggin, M., Jetha, N. N. & Marziali, A. "Noise analysis and reduction in solid-state nanopores". *Nanotechnology* **18,** 305505 (2007).

155. Tasserit, C., Koutsioubas, A., Lairez, D., Zalczer, G. & Clochard, M. C. "Pink noise of ionic conductance through single artificial nanopores revisited". *Physical Review Letters* **105,** 260602 (2010).

156. Smeets, R. M. M., Dekker, N. H. & Dekker, C. "Low-frequency noise in solid-state nanopores." *Nanotechnology* **20,** 095501 (2009).

157. Smeets, R. M. M., Dekker, N. H. & Dekker, C. "Low-frequency noise in solid-state nanopores". *Nanotechnology* **20,** 095501 (2009).

158. Powell, M. R., Vlassiouk, I., Martens, C. & Siwy, Z. S. "Nonequilibrium 1/f noise in rectifying nanopores". *Physical Review Letters* **103,** 9–12 (2009).

159. Powell, M. R. *et al.* "Noise properties of rectifying nanopores". *Journal of Physical Chemistry C* **115,** 8775–8783 (2011).

160. Hoogerheide, D. P., Garaj, S. & Golovchenko, J. A. "Probing surface charge fluctuations with solid-state nanopores". *Physical Review Letters* **102,** 256804 (2009).

161. Wohnsland, F. & Benz, R. "1/f-Noise of open bacterial porin channels". *Journal of Membrane Biology* **158,** 77–85 (1997).

162. Bezrukov, S. M. & Winterhalter, M. "Examining noise sources at the single-molecule level: 1/f noise of an open maltoporin channel". *Physical Review Letters* **85,** 202–205 (2000).

163. Hooge, F. N. "1/F Noise Is No Surface Effect". *Physics Letters A* **29,** 139–140 (1969).

164. Green, M. E. "Diffusion and 1/f noise". *The Journal of Membrane Biology* **28,** 181–186 (1976).

165. Neumcke, B. "1/F Noise in Membranes." *Biophysics of structure and mechanism* **4,** 179–199 (1978).

166. Neumcke, B. "1/f Membrane noise generated by diffusion processes in unstirred solution layers." *Biophysics of structure and mechanism* **1,** 295–309 (1975).

167. Detcheverry, F. & Bocquet, L. "Thermal fluctuations in nanofluidic transport". *Physical Review Letters* **109,** 024501 (2012).

168. Martys, N. & Mountain, R. "Velocity Verlet algorithm for dissipative-particle-dynamics-based models of suspensions". *Physical Review E* **59,** 3733–3736 (1999).

169. Weeks, J. D., Chandler, D. & Andersen, H. C. "Role of repilsive forces in determining the equilibrium structure of simple liquids". *The Journal of Chemical Physics* **54,** 5237–5247 (1971).

170. Walker, J. S. *Fast fourier transforms* (CRC Press, 1996).

171. Cooley, J. W. & Tukey, J. W. "An Algorithm for the Machine Calculation of Complex Fourier Series". *Mathematics of computation* **19,** 297–301 (1966).

172. Levitz, P. "Random flights in confining interfacial systems". *Journal of Physics: Condensed Matter* **17,** S4059–S4074 (2005).

173. Wolfram Research, I. *Mathematica*. 2014.

174. Levesque, M., Bénichou, O., Voituriez, R. & Rotenberg, B. "Taylor dispersion with adsorption and desorption". *Physical Review E* **86,** 036316 (2012).

175. Picallo, C. B., Gravelle, S., Joly, L. & Charlaix, E. "Supplemental Material for " Nanofluidic osmotic diodes : theory and molecular dynamics simulations "". *Phys. Rev. Lett.* 1–6 (2013).

Contents

Resume : This thesis discusses various situations linked to transport at the nanoscale. The first chapter is an introduction to nanofluidics, containing a review of characteristic lengths, forces, or phenomena existing at the nanoscale. The second chapter is a study of the impact of geometry on the hydrodynamic permeability of a nanopore. This study, inspired by the shape of aquaporins, suggests a possible optimisation of permeability for bi-conical channels. The third chapter is a study of capillary filing inside subnanometric carbon channels which highlights the importance of the disjoining pressure induced by the fluid structuring inside the nanochannel. The fourth chapter is a study of nanofluidic diode, a component known to mimic the behaviour of semiconductor diode. The study highlights a strong coupling between water and ion dynamics which leads to a water flow rectification inside the diode. The fifth and last chapter is a study of the origin of commonly observed pink noise ($1/f$) in ionic current measurements through nanopores.

Key-words : nanofluidics, transport, aquaporin, capillary filling, nanofluidic diode, pink noise, molecular dynamics, finite elements.

Résumé : Cette thèse décrit diverses situations liées au transport fluidique aux nano-échelles. Le premier chapitre est une introduction à la nanofluidique qui contient une revue des longueurs caractéristiques, des forces et des phénomènes présents aux nano-échelles. Le deuxième chapitre est une étude de l'impacte de la géométrie sur la perméabilité hydrodynamique d'un nanopore. Inspirée par la forme des aquaporines, cette étude suggère une optimisation possible pour des canaux biconiques. Le troisième chapitre est une étude du remplissage capillaire dans des canaux sub-nanométriques en carbone. Cette étude montre l'importance de la pression de disjonction induite par la structure du fluide sur le remplissage. Le quatrième chapitre est une étude d'une diode nanofluidique, un composant connu pour imiter le comportement d'une diode à semi-conducteur. On montre qu'un fort couplage entre l'eau et la dynamique des ions entraîne une rectification du flux d'eau à l'intérieur de la diode. Le cinquième et dernier chapitre est une étude de l'origine du bruit rose ($1/f$) communément observé lors des mesures de courant ionique dans les nanopores.

Mots-clés: nanofluidique, transport, aquaporine, remplissage capillaire, diode nanofluidique, bruit rose, dynamique moléculaire, éléments finis.